PLASMA DYNAMICS

X. PLASMAS AND CONTROLLED NUCLEAR FUSION*

A. Waves and Radiation

Academic and Research Staff

Prof. G. Bekefi
Prof. S. C. Brown
Prof. W. M. Manheimer
Prof. B. L. Wright
J. J. McCarthy
W. J. Mulligan

Graduate Students

R. J. Becker
A. J. Cohen
L. Litzenberger
L. P. Mix, Jr.
L. D. Pleasance
G. L. Rogoff
C. E. Speck
E. N. Spithas
D. W. Swain
J. H. Vellenga

1. THEORY OF ION ACOUSTIC WAVES

The propagation characteristics of ion acoustic waves have been studied in highly ionized collisionless helium and argon plasmas.[1] The study indicates that the waves are dispersionless and obey the classical dispersion relation for ion acoustic waves propagating in an infinite medium along a magnetic field. The waves, however, are heavily damped. In an attempt to explain this heavy damping, two different approaches have been used in the derivation of the ion acoustic wave theory. One theory, based on the Vlasov equation, ignores collisions and predicts the damping to be independent of frequency and a function only of the ratio of electron to ion temperatures for plasma parameters typically observed in PF-1. The other theory is based on the macroscopic transport equations and predicts a damping that has a strong frequency dependence and is a function of electron and ion temperature and density. In this report these theories and their predicted damping curves are presented.

The strong magnetic field used to constrain the plasma to the axis of the system suggests that only one dimension need be considered for these longitudinal waves. The good agreement between the observed dispersion curves and the classical curves, which are derived under the assumption of an infinite geometry, hints that boundary effects may be unimportant for this simple longitudinal mode of the plasma. Therefore, both theories will be derived, under the assumption of an infinite homogeneous plasma in one dimension and neglecting the magnetic field. Drift of the plasma has been observed experimentally; therefore, the equations will be derived to include the effects of drift on the dispersion relations. The effect of a non-Maxwellian electron distribution is also considered.

---

*This work was supported by the U.S. Atomic Energy Commission (Contract AT(30-1)-3980).

Collisionless Theory

The basis for this theory will be the collisionless Boltzmann equation or Vlasov equation. If we assume the electrostatic approximation in addition to the approximations stated above, the following well-known dispersion relation for longitudinal waves is obtained.

$$D(k,\omega) = 1 - \sum_s \frac{\omega_{p_s}^2}{k^2} \int_{-\infty}^{\infty} \frac{F_{s_o}(u)}{u - \frac{\omega}{k}} = 0. \tag{1}$$

Here F_{s_o} is the one-dimensional distribution function, k is the wavevector, and ω_{p_s} is the plasma frequency of the species. Under the assumption that the species are in a drifted Maxwellian distribution with a streaming velocity U_s, the equation further reduces to the following form

$$D(k,\omega) = 1 - \sum_s \frac{\omega_{p_s}^2}{k^2 a_s^2} Z'\left(\frac{\omega}{k a_s} - \frac{U_s}{a_s}\right), \tag{2}$$

where Z' is the first derivative of the plasma dispersion function,[2] and $a_s = \sqrt{2T_s/m_s}$ is the thermal speed of the species. Making the usual assumption $a_e \gg \frac{\omega}{k} \gg a_i$, we may use the power-series expansion and the asymptotic expansion for the plasma dispersion function. Keeping two terms in the ion expansion and one in the electron expansion for the dispersion function, we obtain for one of the two sets of roots

$$\left(\frac{\omega}{k} - U_i\right)^2 = \frac{T_e + 3T_i\left(1 + \frac{k^2\lambda_{D_e}^2}{2}\right)}{\left(1 + \frac{k^2\lambda_{D_e}^2}{2}\right)m_i}, \tag{3}$$

where $\lambda_{D_e} = \frac{a_e}{\omega_{p_e}}$ is the electron Debye length. If we further assume that $k\lambda_{D_e} \ll 1$, which is a very good approximation for the plasma produced in PF 1, Eq. 3 becomes

$$\frac{\omega}{k} = V_s + U_i,$$

where

$$V_s = \sqrt{\frac{T_e + 3T_i}{m_i}}. \tag{4}$$

If instead, two terms in the electron expansion are retained, and only the leading term in the ion expansion is retained, one of the two sets of roots that is obtained is

$$\left(\frac{\omega}{k} - U_i\right)^2 = \frac{T_e}{m_i} \frac{1}{1 + \frac{k^2 \lambda_{D_e}^2}{2}} \left[1 + \frac{m_e}{4m_i}\left(\frac{\frac{\omega}{k} - U_e}{\frac{\omega}{k} - U_i}\right)^2\right]. \tag{5}$$

If the frequency is assumed to have a small imaginary part, we can expand the dispersion function in a power series of the real part, that is, if $\omega = \omega_r + i\gamma$ and $\frac{\gamma}{\omega_r} \ll 1$, then

$$D(k, \omega) = D(k, \omega_r) + i\gamma D'(k, \omega_r) - \frac{\gamma^2}{2!} D''(k, \omega_r) + \ldots . \tag{6}$$

Assuming $\gamma \approx 0$, we obtain to first order

$$\gamma \approx - \frac{\text{Im } (D(k, \omega_r))}{\text{Re } (D'(k, \omega_r))}, \tag{7}$$

where $D'(k, \omega_r)$ is the first derivative of Eq. 2 with respect to ω and evaluated at $\omega = \omega_r$. Because γ is assumed small, the power-series expansion of the plasma dispersion function for the ions will be used in which it is assumed γ equal to zero. Putting into Eq.7 the values obtained from the first-order expansion, the following equation for γ is obtained

$$\gamma = k \sqrt{\frac{T_e}{m_i}} \sqrt{\frac{\pi}{8}} \left\{\sqrt{\frac{m_e}{m_i}} + \left(\frac{T_e}{T_i}\right)^{3/2} \exp\left(-\frac{T_e}{2T_i}\right)\right\}. \tag{8}$$

In Eq. 8, the ions and electrons are assumed to have equal streaming velocities.

Although these forms of the solution are relatively simple and easy to use, for our experiments the approximations are not strictly valid. To avoid this difficulty, Eq. 2 was solved on the computer, using a modified Newton-Raphson method.[3] The exact solution of the dispersion equation obtained in this manner indicates that Eq. 4 gives the real part of the dispersion relation within an accuracy of 3% for values of T_e/T_i from 1 to 40. Equation 8 is found to be in poor agreement with the exact computer solution.

The quantity,

$$\frac{D_e}{\lambda} = \frac{-\omega}{2\pi\gamma}, \tag{9}$$

rather than γ, is the quantity that is measured experimentally; therefore this quantity,

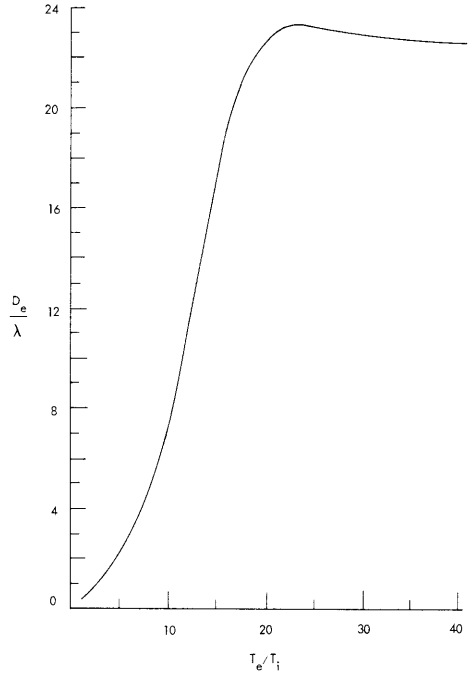

(a)

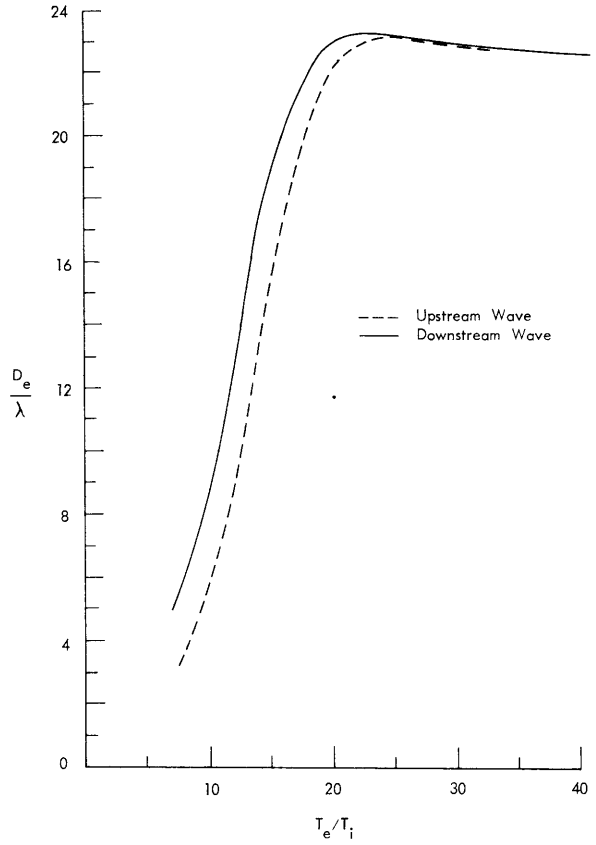

(b)

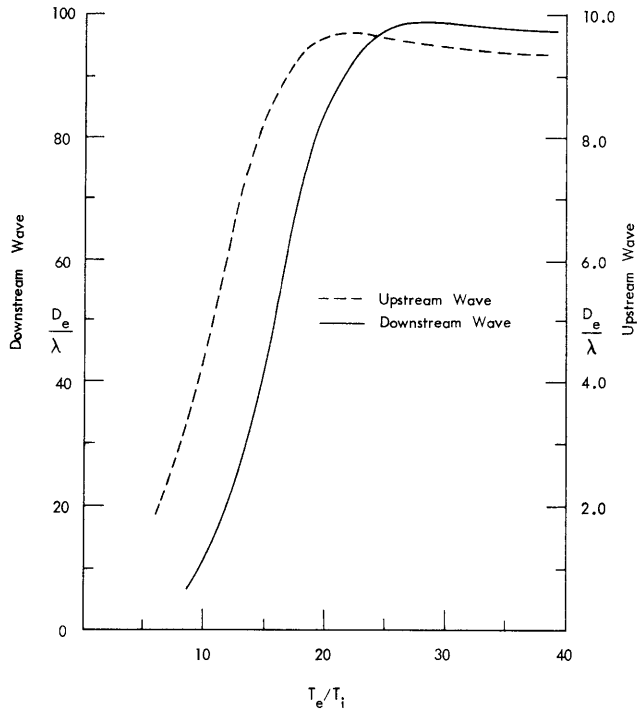

(c)

Fig. X-1.

Theoretical values of Landau damping as a function of the ratio of electron-to-ion temperature in a helium plasma. (a) No electron or ion drifts. (b) Ion drift velocity 0.3 V_s; electron drift velocity 0.0. (c) Ion drift velocity 0.3 V_s; electron drift velocity V_s.

rather than γ, will be discussed in the rest of this report. If the electron and ion drift velocities are equal, the value of the damping term D_e/λ is found to vary from the value obtained with no drift, $(D_e/\lambda)_o$, in the following way

$$\frac{D_e}{\lambda} = \left(\frac{D_e}{\lambda}\right)_o \left(1 + \frac{U_i}{V_s}\right). \tag{10}$$

Because of the good agreement (less than 3% variation) between the exact solution and this equation, the theoretical curve of $(D_e/\lambda)_o$ as a function of T_e/T_i is shown in Fig. X-1a. These values of $(D_e/\lambda)_o$ are found to be independent of ion temperature, at least for values between 0.1 and 0.4 eV, and a function only of the temperature ratio T_e/T_i. For comparison, Fig. X-1b and X-1c gives the values of D_e/λ as a function of T_e/T_i for upstream and downstream propagation with the electron and ion drift velocities unequal.

The pronounced breaks observed in some of the log I vs V curves that were used to obtain the electron temperature suggests that the plasma might consist of a two-temperature Maxwellian electron distribution.[4] The fact that the probe curves generally suggested a slightly higher temperature than that calculated from the wavelength of the ion acoustic wave gives additional support to the idea that the body of the electron distribution may not be Maxwellian. It has also been found that if the ion saturation current is extrapolated by using a more horizontal line, i.e., extrapolating that part of the ion saturation curve which appears linear rather than using a tangent to the curve at a point which gives the most linear log I vs V plot, pronounced breaks are observed even near the axis of the column. The temperature obtained by this more horizontal extrapolation indicates a high energy tail typically 9 or 10 eV.

Because of the long mean-free paths for the electrons in this system, it is not unreasonable to assume that the electrons are not in a Maxwellian distribution. The grid farthest from the plasma-generating structure is observed to act as an electrostatic reflector, causing the mirror magnetic field to have no observable effect on either the plasma or the wave propagation. The reflecting efficiency of electrostatic reflectors is greatest when the velocity of the reflected particles normal to the reflector is the smallest. Therefore, because of the observed discrepancies between measurements of the electron temperature and the definite possibility that the grids could cause an overpopulation of the low parallel energy electrons relative to a Maxwellian distribution, the effects of a two-temperature Maxwellian will be considered.

The effect of a colder component of the electron distribution on the dispersion relation is simply to add an additional term to the sum over the species in Eq. 1. This additional term causes Eq. 2 to take the following form:

$$D(k,\omega) = k^2\lambda_{D_e}^2 - \frac{T_e}{T_i} Z'\left(\frac{\frac{\omega}{k} - U_i}{a_i}\right) - \frac{T_e}{T'_e}\delta Z'\left(\frac{\frac{\omega}{k} - U'_e}{a_e}\right) - \epsilon Z'\left(\frac{\frac{\omega}{k} - U_e}{a_e}\right), \tag{11}$$

where δ and ϵ are the fractional concentrations of the cold and hot electron distributions, and the primed variables denote the parameters of the colder electron species.

For simplicity, assume $U_i = U_e = U'_e = 0$, and $a_i \ll \frac{\omega}{k} \ll a'_e < a_e$. Using the appropriate series expansions for $Z'(\xi)$, the following dispersion relation is obtained if only the leading terms of the expansions are kept:

$$\frac{\omega^2}{k^2} = \frac{T_e T'_e}{m_i(\delta T_e + \epsilon T'_e)} \tag{12}$$

or

$$\frac{\omega^2}{k^2} = \frac{T_{eff}}{m_i},$$

where

$$T_{eff} = \frac{T_e T'_e}{T'_e + \delta(T_e - T'_e)} \qquad \epsilon + \delta = 1. \tag{13}$$

The imaginary part of the dispersion relation is computed by using (7) and the leading terms in the expansions of $Z'(\xi)$. The following equation is obtained.

$$\frac{\gamma}{\omega} \approx -\sqrt{\frac{\pi}{8}} \left\{ \left(\frac{T_{eff}}{T_i}\right)^{3/2} \exp\left(-\frac{T_{eff}}{2T_i}\right) + \sqrt{\frac{m_e}{m_i}} \left(\delta \left(\frac{T_{eff}}{T'_e}\right)^{3/2} + \epsilon \left(\frac{T_{eff}}{T_e}\right)^{3/2} \right) \right\}. \tag{14}$$

The full equation, Eq. 11, was solved exactly for several values of T_{eff} and T_e, with zero drift assumed. The real part of the dispersion relation agrees with Eq. 15 within 3%:

$$\frac{\omega^2}{k^2} = \frac{T_{eff} + 3T_i}{m_i}. \tag{15}$$

The imaginary part of the dispersion relation is plotted as a function of T'_e in Fig. X-2, for values of T_{eff} typically obtained from wavelength measurements, and values of T_e typical of those measured by using the more horizontal ion saturation current extrapolation. From Eq. 13 δ and ϵ were obtained.

Collisional Theory

The high densities that are obtainable with this plasma source suggested that viscous damping might be playing an important role in the damping of the waves. Since, in

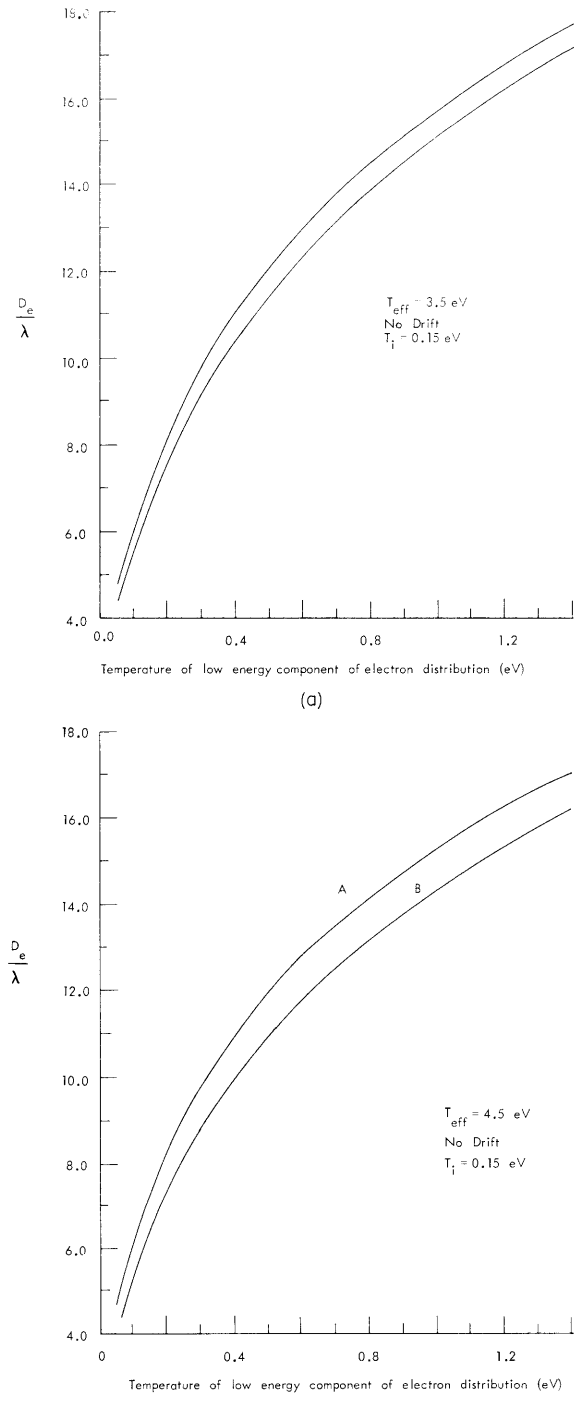

Fig. X-2. Theoretical values of the Landau damping for a helium plasma having a two-temperature Maxwellian electron distribution. The temperature of the high-energy component of the electron distribution is 9 eV for curve (a) and 11 eV for curve (b).

general, the mean-free path of the ions is less than the wavelength of the waves that are observed, a fluid description is valid, at least for the ions. Since the magnetic field used to contain the plasma is sufficiently large to satisfy the following inequalities:

$$\Omega_e \gg \Omega_i > \nu_i, \nu_e,$$

where Ω_i and Ω_e are the ion and electron-cyclotron frequencies, and ν_i and ν_e are the self-collision frequencies of the ions and electrons, many simplifying assumptions may be made. Braginskii[5] has considered these assumptions in some detail; therefore, the transport equations derived by him will be used. The variables in the transport equation will be assumed to consist of a steady-state plus a small perturbation having a harmonic variation of the form, $\exp(i(\omega t+kz))$. This is essentially equivalent to Fourier-Laplace transforming the transport equations and solving them for times sufficiently long that the initial-value terms introduced by the Laplace transforms can be neglected and only the natural modes of the system considered. Absolute neutrality will also be assumed.

With these assumptions, the mass conservation equation for the ions may be linearized to give

$$(\omega+U_i k)\tilde{n} = -kn\tilde{U}_i, \tag{16}$$

where n is the density and the tilde denotes a small perturbation to the steady state. Defining $\omega_{||} = kU_e$, the electron-mass conservation equation becomes

$$(\omega+\omega_{||})\tilde{n} + nk\tilde{U}_e = 0. \tag{17}$$

The momentum conservation equations may be linearized to yield the following relations if we neglect electron inertia; that is, we assume the frequency of the variation of the electron velocity to be much greater than the frequency of the collective modes of interest.

$$0 = -k(\tilde{n}T_e+n\tilde{T}_e) \tag{18}$$

$$nm_i(\omega+kU_i)\,\tilde{U}_i = -k(n\tilde{T}_i+\tilde{n}T_i). \tag{19}$$

Adding Eqs. 18 and 19, we obtain

$$nm_i(\omega+kU_i)\,\tilde{U}_i = -k(\tilde{n}(T_e+T_i)+n(\tilde{T}_i+\tilde{T}_e)). \tag{20}$$

Proceeding to the energy balance equations for the ions and electrons, we have

$$\frac{\tilde{T}_i}{T_i}\left\{\frac{3}{2}(\omega+kU_i) - i\chi_i\frac{k^2a_i^2}{\nu_i}\right\} - (\omega+kU_i)\frac{\tilde{n}}{n} = 0 \tag{21}$$

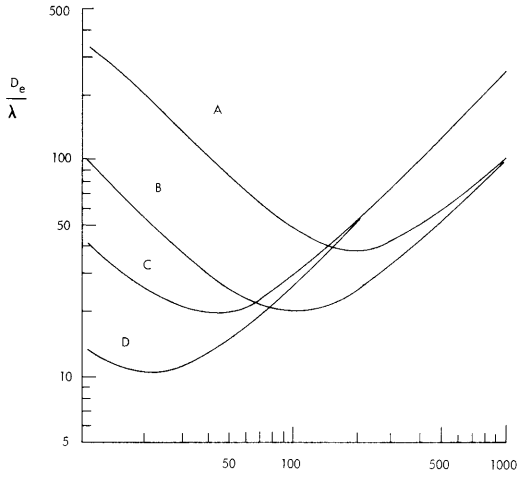

Curve	T_i (eV)	T_e (eV)	$\nu_i \times 10^{-4}$	$\nu_e \times 10^{-4}$
A	0.1	4.0	3.979	2.178
B	0.1	2.0	3.979	5.719
C	0.2	4.0	1.570	2.175
D	0.2	2.0	1.570	5.719

(a)

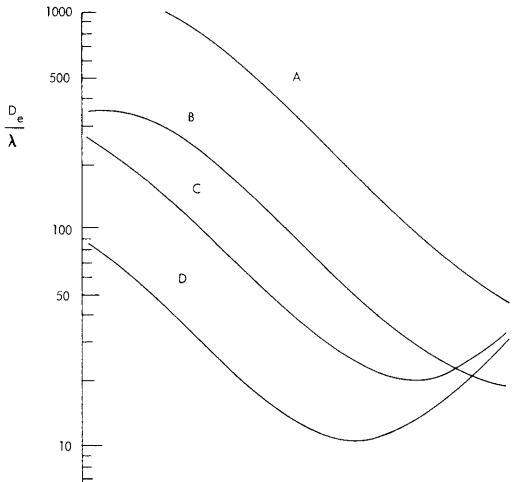

Curve	T_i (eV)	T_e (eV)	$\nu_i \times 10^{-5}$	$\nu_e \times 10^{-5}$
A	0.1	4.0	1.389	2.005
B	0.1	2.0	1.389	5.229
C	0.2	4.0	3.467	2.005
D	0.2	2.0	3.467	5.229

(b)

Fig. X-3. Theoretical values of the viscous damping in a helium plasma as a function of frequency. The density for curves (a) and (b) is $4 \times 10^9/cm^3$ and $4 \times 10^{10}/cm^3$.

$$\frac{\tilde{T}_e}{T_e}\left\{\frac{3}{2}(\omega+\omega_{||}) - i\chi_e\frac{k^2a_e^2}{\nu_e}\right\} - (\omega+\omega_{||})\frac{\tilde{n}}{n} = 0. \tag{22}$$

The mass conservation equations have been used to obtain these forms; χ_i and χ_e are numerical factors equal to 1.95 and 1.58 for singularly ionized ions and electrons, respectively. Combining Eqs. 20, 21, and 22, we arrive at the following expression:

$$-nm_i\left(\frac{\omega + kU_i}{k}\right)\tilde{U}_i = \tilde{n}\left\{(T_e+T_i) + \frac{T_i}{\frac{3}{2} - \frac{i\hat{\chi}_i}{\omega + kU_i}} + \frac{T_e}{\frac{3}{2} - \frac{i\hat{\chi}_e}{\omega + \omega_{||}}}\right\}, \tag{23}$$

where

$$\hat{\chi}_s = \chi_s\frac{k^2a_s^2}{\nu_s}.$$

In the limit $k^2a_e^2 \gg \nu_e(\omega+\omega_{||})$ (long electron mean-free paths), this equation takes the form

$$\frac{-nm(\omega+kU_i)\tilde{U}_i}{k} = \tilde{n}\left\{T_e\left(1 + \frac{i(\omega+\omega_{||})}{\hat{\chi}_e}\right) + T_i\left(1 + \frac{\frac{3}{2} + \frac{i\hat{\chi}_i}{\omega + kU_i}}{\frac{9}{4} + \frac{\hat{\chi}_i^2}{(\omega+kU_i)^2}}\right)\right\}. \tag{24}$$

Using Eq. 16, we arrive at the dispersion relation

$$\frac{(\omega+kU_i)^2}{\omega_s^2} - \left(1 + \frac{T_i}{T_e} + \frac{\frac{3}{2}\frac{T_i}{T_e}}{\frac{9}{4} + \frac{\hat{\chi}_i^2}{(\omega+kU_i)^2}}\right) = \frac{i}{\hat{\chi}_e}\left(\omega + \omega_{||} + \frac{\hat{\chi}_i\hat{\chi}_e}{(\omega+kU_i)}\frac{\frac{T_i}{T_e}}{\frac{9}{4} + \frac{\hat{\chi}_i^2}{(\omega+kU_i)^2}}\right), \tag{25}$$

where $\omega_s^2 = k^2T_e/m_i$.

Equation 25 may be put into the form of a fourth-order polynomial in ω, and solved by a number of methods. Muller's method[3] was used to solve this equation for various values of the wavevector k, electron temperature, ion temperature, and density. The reciprocals of the self-collision times from Spitzer[6] were used for the collision frequencies. The theoretical curves relating D_e/λ to the frequency, $f = \omega/2\pi$, are shown for helium in Fig. X-3 for typical ion and electron temperatures and densities. The numerical factors, χ_i and χ_e, were set equal to one for these calculations.

L. P. Mix, Jr., G. Bekefi

1. L. P. Mix, Jr., L. Litzenberger, and G. Bekefi, Quarterly Progress Report No. 93, Research Laboratory of Electronics, M.I.T., April 15, 1969, pp. 69-84.

2. B. D. Fried and S. D. Conte, The Plasma Dispersion Function (Academic Press, New York, 1961).

3. C. E. Froberg, Introduction to Numerical Analysis (Addison-Wesley Publishing Co., Reading, Mass., 1965).

4. L. P. Mix, Jr., E. W. Fitzgerald, and G. Bekefi, Quarterly Progress Report No. 92, Research Laboratory of Electronics, M.I.T., January 15, 1969, p. 227.

5. S. I. Braginskii, Reviews of Plasma Physics, M. A. Leontovich (ed.) (Consultants Bureau Enterprises, Inc., New York, 1965), Vol. 1, pp. 205-311.

6. L. Spitzer, Jr., Physics of Fully Ionized Gases (Interscience Publishers, New York, 1962).

2. THREE-WAVE COUPLING IN CLYNDRICAL PLASMAS

We consider a plasma cylindrical column in the presence of a uniform magnetic field, directed along the axis of the cylinder. Our description of the system is simple: (a) The electrons are assumed to behave like a charged conducting fluid. Their thermal motion is neglected. (b) The ions constitute a uniform neutralizing background. (c) The external magnetic field is of such strength that the motion of electrons perpendicular to it is neglected.

We are interested in plasma waves whose phase velocity is much smaller than the velocity of light, so that we may use the quasi-static approximation (neglect of AC magnetic field).

The equations that describe the system are

$$\frac{\partial v}{\partial t} - \frac{e}{m}\frac{\partial \phi}{\partial z} = -\frac{1}{2}\frac{\partial}{\partial z}(v^2) \tag{1}$$

$$\frac{\partial n}{\partial t} + N\frac{\partial v}{\partial z} = -\frac{\partial}{\partial z}(nv) \tag{2}$$

$$\nabla^2\phi = 4\pi en. \tag{3}$$

We have taken the external magnetic field in the z-direction (along the axis of the plasma column); v is the component of velocity perturbation in the z-direction; m and (-e) are the mass and charge of an electron; N is the number density of the ions, n + N the number density of electrons; ϕ is the perturbation potential.

Linear Solution

The linear solution is found by neglecting products of first-order quantities, and assuming solutions in the form of plane waves in the axial direction. The well-known result is[1]

$$\phi(\underline{r}t) = AJ_m(pr)\, e^{i(kz-\omega t+m\theta)} \tag{4}$$

$$v(\underline{r}t) = -\frac{e}{m}\frac{k}{\omega}\phi(\underline{r}t) \tag{5}$$

$$n(\underline{r}t) = -\frac{e}{m}N\frac{k^2}{\omega^2}\phi(\underline{r}t) \tag{6}$$

$$p^2 \equiv -k^2\epsilon. \tag{7}$$

Here, ϵ is the cold-plasma dielectric function, and A is a complex constant.

In the case of a perfectly conducting plasma-filled waveguide, the potential vanishes at the wall, r = R. This gives the dispersion relation

$$\frac{x_{mn}^2}{R^2} = -k^2\left(1 - \frac{\omega_p^2}{\omega^2}\right), \tag{8}$$

where x_{mn} is the n^{th} root of the m^{th}-order Bessel function. For low frequencies, the phase velocity is

$$v_{ph} = \omega_p \frac{R}{x_{mn}} \tag{9}$$

The group velocity is easily found from Eq. 8,

$$v_g = \frac{\partial\omega}{\partial k} = \frac{\epsilon(\omega)}{\epsilon(\omega) - 1}\left(\frac{\omega}{k}\right). \tag{10}$$

Equation 8 shows that the waves cut off at the plasma frequency.

Coupled-Mode Equations

We combine Eqs. 1-3 to obtain

$$\frac{\partial^2}{\partial t^2}\nabla_\perp^2\phi + \left(\omega_p^2 + \frac{\partial^2}{\partial t^2}\right)\frac{\partial^2\phi}{\partial z^2} = \frac{4\pi eN}{2}\frac{\partial^2}{\partial z^2}(v^2) - 4\pi e\frac{\partial^2}{\partial t\partial z}(uv). \tag{11}$$

Here, we have separated the Laplacian operator into its axial and transverse components.

The nonlinear terms are assumed sufficiently small, so that we may use the linear expressions for the number density and the velocity. We first expand n and v in the form

$$v(\underline{r}t) = \sum_{mn} v_{mn}(r)\, e^{i(kz-\omega_{mn}t+m\theta)}$$

$$n(\underline{r}t) = \sum_{mn} n_{mn}(r)\, e^{i(kz-\omega_{mn}t+m\theta)}. \tag{12}$$

We substitute these relations in the right-hand side of Eq. 11, denoted by R, and obtain in simplified notation,

$$R = -\frac{4\pi eN}{2}\sum (k'+k'')^2\, v'v''G - \frac{4\pi e}{2}\sum (k'+k'')(\omega'+\omega'')[n'v''+n''v']G, \tag{13}$$

where

$$G \equiv \exp[i(k'+k'')z - i(\omega'+\omega'')t + i(m'+m'')\theta].$$

We use (5) and (6) to relate the eigenfunctions for the density and velocity to the eigenfunction for the potential. We substitute these relations in (13) to get, after some reductions,

$$R = -\frac{e}{m}\omega_p^2 \sum (k'+k'')(\omega'+\omega'')\,\frac{k'}{\omega'}\,\frac{k''}{\omega''}\left\{\frac{(k'+k'')}{(\omega'+\omega'')} + \frac{k'}{\omega'} + \frac{k''}{\omega''}\right\}\phi'\phi''G. \tag{14}$$

These are the driving terms in (11). If they are set equal to zero, the last equation has the linear solutions already discussed. Since the radial and azimuthal modes form a complete set, at given z and t we can expand the potential in (11) as a sum of such modes. If we set

$$\phi(\underline{r}t) = \sum_{mn} \phi_{mn}(zt)\, J_m(p_{mn}r)\, \exp[i(kz - \omega_{mn}t + m\theta)], \tag{15}$$

then $\phi(zt)$ will be a slowly varying function of z and t if the nonlinearity is weak.

Substituting the expansion (15) in the left-hand side of (11), denoted by L, and neglecting second derivatives in z and t, we obtain

$$L = -\sum_{mn} \omega_{mn}^2 \exp[i(kz - \omega_{mn}t + m\theta)]$$

$$\times \left\{\nabla_\perp^2 + p_{mn}^2 + 2i\epsilon_{mn}k\frac{\partial}{\partial z} + \frac{2i}{\omega_{mn}}\left(\nabla_\perp^2 - k^2\right)\frac{\partial}{\partial t}\right\}\phi_{mn}(zt)$$

$$\times J_m(p_{mn}r). \tag{16}$$

Substituting (15) in (14) and setting the resulting expression equal to (16), we obtain the desired nonlinear equation. We can eliminate the dependence on the transverse coordinates by making use of the orthogonality relation

$$\int_0^{2\pi} d\theta\, e^{i(m+m')\theta} \int_0^R r\,dr\, J_m(p_{mn}r)\, J_{m'}(p_{m'n'}r) = \delta_{m+m',\,o}\,\delta_{n,n'}\frac{R^2}{2} J'^2_m(p_{mn}R)$$

and the fact that

$$\left(\nabla_\perp^2 + p_{mn}^2\right) J_m(p_{mn}r) = 0.$$

We finally obtain

$$\left(\frac{\partial}{\partial z}+\frac{1}{u_{mn}}\frac{\partial}{\partial t}\right)\phi_{mn}(zt) = -\left(\frac{i}{2}\right)\frac{1}{k\epsilon_{mn}}\sum_{n'n''} V(\omega|\omega'|\omega'')$$
$$\times \phi_{m'n'}\phi_{m''n''}\alpha(n'n'')$$
$$\times \exp[-i\Delta k z + i\Delta\omega_{mn}t], \qquad (17)$$

where

$$V(\omega|\omega'|\omega'') = -\frac{e}{2m}\omega_p^2\frac{1}{\omega^2}(k'+k'')(\omega'+\omega'')\frac{k'}{\omega'}\frac{k''}{\omega''}\left\{\frac{(k'+k'')}{(\omega'+\omega'')}+\frac{k'}{\omega'}+\frac{k''}{\omega''}\right\}$$

$$\alpha(n'n'') = \frac{1}{\frac{R^2}{2}J'^2_m(p_{mn}R)}\int_0^R r\,dr\,J_m(p_{mn}r)\,J_{m'}(p_{m'n'}r)\,J_{m''}(p_{m''n''}r)$$

$$u_{mn} = -\frac{\omega_{mn}\epsilon_{mn}k}{\left(p_{mn}^2+k^2\right)} = \frac{\epsilon_{mn}}{\epsilon_{mn}-1}\left(\frac{\omega_{mn}}{k}\right)$$

and

$$\Delta\omega_{mn} = \omega_{mn} - (\omega_{m'n'}+\omega_{m''n''})$$
$$\Delta k = k - (k'+k'') \qquad (18)$$
$$0 = m - (m'+m'')$$

Equation 17 is the final relation. It describes the coupling of the $(m, n)^{th}$ mode to all other modes that satisfy the relations (18). Note that there is no such relation for the radial (quantum) number, n. Also notice that the velocity u_{mn} is the group velocity of the $(m, n)^{th}$ mode. For appreciable energy exchange either $\Delta\omega = \Delta k = 0$ (resonance), or these quantities are small compared with any of the frequencies or wavevectors (quasi-resonance).

For three-wave coupling, we drop the summation in (17), and introduce the simplified notation

$(m, n) \rightarrow (1)$

$(m', n') \rightarrow (2)$

$(m'', n'') \rightarrow (3)$.

We also put in the expression for the coupling coefficients

$$k_1 = k_2 + k_3, \quad \omega_1 = \omega_2 + \omega_3,$$

which is exact in the case of resonance, and holds approximately in the case of quasi-resonance.

With this notation, we get

$$\left(\frac{\partial}{\partial z} + \frac{1}{u_1}\frac{\partial}{\partial t}\right)\phi_1(zt) = +\left(\frac{i}{2}\right) V_1\phi_2\phi_3 \exp[-i\Delta k_1 z + i\Delta\omega_1 t]$$

$$\left(\frac{\partial}{\partial z} + \frac{1}{u_2}\frac{\partial}{\partial t}\right)\phi_2(zt) = +\left(\frac{i}{2}\right) V_2\phi_1\phi_3^* \exp[+i\Delta k_2 z - i\Delta\omega_2 t]$$

$$\left(\frac{\partial}{\partial z} + \frac{1}{u_3}\frac{\partial}{\partial t}\right)\phi_3(zt) = +\left(\frac{i}{2}\right) V_3\phi_1\phi_2^* \exp[+i\Delta k_3 z - i\Delta\omega_3 t], \tag{19}$$

where

$$V_j = +\frac{a_j}{k_j(-\epsilon_j)} V \qquad (j = 1, 2, 3)$$

$$V = \frac{e}{2m}\omega_p^2 \frac{k_1k_2k_3}{\omega_1\omega_2\omega_3}\left\{\frac{k_1}{\omega_1} + \frac{k_2}{\omega_2} + \frac{k_3}{\omega_3}\right\}.$$

Equations 19 is a system of partial differential equations. Since they are very complicated in general, we deal only with two specific cases.

Spatial Variation in the Mode Amplitudes

If we put in Eqs. 19 $\frac{\partial}{\partial t} = 0$, we find that the resulting equations are in exactly the same form as in a previous report.[2] If we treat them in exactly the same way, we find the solutions

$$N_1(z) = N_{1a} + (N_{1b} - N_{1a})\, y^2[z]$$

$$y^2[z] = sn^2\left[(N_{1c} - N_{1a})^{1/2}\frac{H}{2}|z - z_o|\right], \tag{20}$$

where sn(u) denotes the elliptic integral of the first kind of modulus Λ,

$$0 < \Lambda^2 = \frac{N_{1b} - N_{1a}}{N_{1c} - N_{1a}} \leq 1,$$

$$H = [V_1 V_2 V_3]^{1/2}$$

$$N_j = \frac{A_j^2}{V_j} \qquad (j = 1, 2, 3),$$

and A_j is the amplitude of mode j. The period of the elliptic function is[3]

$$4K(\Lambda^2) = 4 \int_0^1 dt\, (1-t^2)^{-1/2}\, (1-\Lambda^2 y^2)^{-1/2},$$

so that the period in z is given by

$$L = \frac{4K(\Lambda^2)}{H/2} [N_{1c}-N_{1a}]^{-1/2}. \tag{21}$$

Temporal Variation in the Mode Amplitudes

We now put in Eqs. 19 $\frac{\partial}{\partial z} = 0$. Then again treating the resulting equations as before,[2] we find

$$\hat{N}_1(t) = \hat{N}_{1a} + (\hat{N}_{1b}-\hat{N}_{1a})\, y^2[t]$$

$$y^2[t] = sn^2\left[(\hat{N}_{1c}-\hat{N}_{1a})^{1/2} \frac{H}{2} |t-t_o| \right] \tag{22}$$

and the period in time is

$$T = \frac{4K(\Lambda^2)}{\hat{H}/2} [\hat{N}_{1c}-\hat{N}_{1a}]^{-1/2}. \tag{23}$$

We see from Eqs. 19 that

$$\hat{V}_j = u_j V_j$$

$$\hat{N}_j = \frac{1}{u_j} N_j \tag{24}$$

$$\hat{H} = (u_1 u_2 u_3)^{1/2} H.$$

Using (24) and comparing (21) and (23), we get

$$T = (u_2 u_3)^{-1/2} L$$

or, put another way,

$$\gamma = (u_2 u_3)^{1/2} \Gamma;$$

that is, the time growth rate, γ, is equal to the space growth rate, Γ, multiplied by the geometric mean of the two group velocities.

E. N. Spithas, W. M. Manheimer

References

1. A. W. Trivelpiece, Slow-Wave Propagation in Plasma Waveguides (San Francisco Press, 1967).
2. L. N. Litzenberger and G. Bekefi, "Nonlinear Coupling of Three Ion Acoustic Waves," Quarterly Progress Report No. 93, Research Laboratory of Electronics, M.I.T., April 15, 1969, pp. 72-84.
3. Handbook of Mathematical Functions (U.S. Department of Commerce, National Bureau of Standards, 1965, pp. 569-570.

3. LANGMUIR PROBE IN THE ORBITAL MOTION REGIME

The purpose of this report is to correct a formula used for determining plasma properties from Langmuir probe curves. The corrected formula is important practically, as well as conceptually, as it allows the plasma density to be computed independently of the electron temperature. Thus the density determination will not be subject to errors in the temperature measurement.

This formula is applicable in the regime in which Langmuir's orbital motion theory applies, namely $r_p \ll \lambda_D$, where r_p is the probe radius, and λ_D is the electron Debye length. Chen has written the expression for the ion current to a cylindrical probe as

$$I = \frac{2}{\sqrt{\pi}} eJ_r(1+\eta_p)^{1/2}, \tag{1}$$

where $J_r = 2\pi r_p(kT_i/2m_i)^{1/2}\, \ell n_o$ is the total random ion flux, and $\eta_p = -eV_p/kT_e$ is the normalized probe potential, with

r_p = probe radius
T_e = electron temperature
ℓ = probe length
m_i = ion mass
T_i = ion temperature
n_o = ion density
V_p = potential with respect to plasma potential.

The proper normalized probe potential, however, should be $\eta_p = -eV_p/kT_i$. With

this η_p, as T_i approaches zero, the ion current properly remains nonzero.

Consider the orbit of an ion in an attractive central force field. Let the initial velocity be v_o and the impact parameter be "b". At the point of closest approach to the potential center let the velocity be v_a and the radius be "a". Then

$$\frac{1}{2}mv_o^2 = \frac{1}{2}mv_a^2 + eV_a \qquad \text{(conservation of energy)}$$

$$bv_o = av_a \qquad \text{(conservation of angular momentum)}$$

$$b = a\left(1 - \frac{2eV_a}{mv_o^2}\right)^{1/2}, \tag{2}$$

where V_a must be referenced to zero (plasma potential) and $mv_o^2/2 = kT_i$. Then $b = a(1+\eta_p)^{1/2}$, where η_p is defined as $-eV_p/kT_i$.

If "a" is the probe radius r_p, then any ion with "b" smaller than $r_p(1+\eta_p)^{1/2}$ will be collected. Therefore the effective probe radius[2] is $r_p(1+\eta_p)^{1/2}$, and the correct formula is

$$n = \frac{2}{\sqrt{\pi}} J_r \left(1 - \frac{eV_p}{kT_i}\right)^{1/2} \tag{3}$$

$$n_o = \frac{m_c}{(2e)^{3/2}(r_p\ell)} \left(\frac{\Delta I^2}{\Delta V}\right)^{1/2}, \tag{4}$$

where all values are in MKS units, and n is independent of T. It is then easy to plot I^2 against V from the measured probe characteristic and use the slope of the resulting straight line in this formula to determine n_o.[3]

The densities derived from this formula are equal to those derived from the exact computer calculations of Laframboise[4] for cylindrical probes with $r_p/\lambda_D < 2.5$.

A. J. Cohen

References

1. F. F. Chen, C. Etievant, and D. Mosher, Phys. Fluids 11, 811 (1968); see Eqs. (1) and (2). This correction similarly holds for spherical probes in the orbital regime.
2. J. E. Allen, R. L. F. Boyd, and P. Reynolds, Proc. Phys. Society (London), Vol. LXX, No. 3-B, p. 297, 1957.
3. For electron current in the electron attracting regime this same formula will hold. See F. F. Chen in Plasma Diagnostic Techniques by R. H. Huddlestone and S. L. Leonard (Academic Press, 1965), Sec. 3.1.2.
4. James G. Laframboise, UTIAS Report No. 100, University of Toronto Institute for Aerospace Studies, June 1966; see Fig. 43 and Eq. (9.10).

4. NONLINEAR HARMONIC GENERATION AT PLASMA RESONANCES

The subject of this report is the generation of harmonics of an RF signal applied to an antenna immersed in the center of a low-density ($n \sim 10^9$ electrons/cm^3), low-pressure ($p \sim 0.4$ μ), DC discharge in Argon.

This harmonic generation was reported in two previous reports.[1,2] Various changes have been made in the system, which have resulted in more precise data of the kind reported previously and in new interesting data.

The experiment is basically the same as that reported earlier. The monopole spherical antenna has been replaced by the split-sphere dipole reported on by Waletzko and Cohen previously.[1,3,4] This was done to increase the Q of the resonance that naturally results in better definition of the observed effects. Since the dipole field is more localized than the monopole field, the dipole field is more intense for a given applied voltage to the antenna. Therefore the harmonic generation is more intense. The spectrum analyzer used earlier as a detector can now be replaced by an RF voltmeter so as to get a direct voltage reading for the harmonics. The coaxial cable used earlier to feed the dipole, RG174, was shown to be significantly lossy at the harmonic frequencies. It has been replaced by precision rigid and semirigid cables. The glass vacuum chamber was surrounded with a cylindrical screen closed top and bottom. This prevented RF leakage from the antenna from going directly into the detecting apparatus. It also prevented spurious pickup of radio and television stations that had been thought to be Tonks-Dattner resonances. Since the shield formed a cylindrical cavity resonant in the range of the harmonics, the RF absorber had to be placed strategically to damp out the cavity resonance. A 20-dB directional coupler was mounted to sample the power incident to the dipole. This power was kept constant during each run of data. The dipole could not be DC-biased because no double DC blocks were available at the frequencies of operation. The antenna is coated with a thin layer of dielectric, Insl-X, so it can remain DC floating throughout the experiment. A movable cylindrical Langmuir probe operating in the Langmuir orbital regime (see Sec. X-A. 3) was used to obtain radial density profiles. A diagram of the experiment is shown in Fig. X-4.

Most RF data were taken by sending 0.50 V of frequency f onto a dipole, 1 3/4 inches in diameter, and monitoring the reflected power both at f and at 2f, and by sending 2f onto the dipole and monitoring the reflected power at 2f. For a given frequency, the reflected signals were observed as a function of discharge current. Then the incident frequency was changed and the measurements were repeated. The RF admittance of the probe was monitored with a GR 1602B admittance meter. The value 0.50 V was chosen because it was large enough to give good results on the output detectors and small enough so as not to perturb the resonance significantly. The gas pressure could

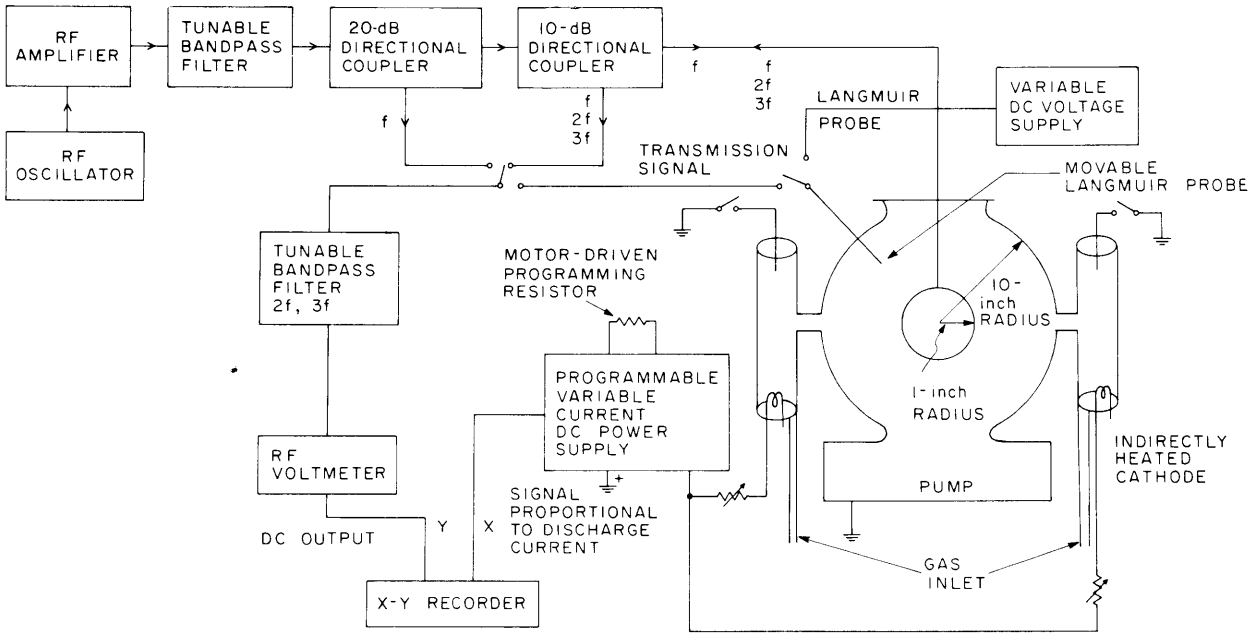

Fig. X-4. Diagram of the experiment.

also be varied from 0.25 μ to 2 μ by changing the flow rate. The measurements reported here are at 0.25 μ and 0.4 μ.

Geometrical Resonance

If a probe is inserted into a plasma, its RF admittance characteristic will show a resonance at a frequency somewhat below plasma frequency. This is attributed to a series resonance between the capacitive sheath surrounding the probe and the inductive plasma just beyond. (A plasma acts as an inductance below plasma frequency, since the conduction current exceeds the displacement current for ω less than ω_p ($\nabla \times H = J + \dot{D}$).)

The variation of the resonance with electron density n has been calculated theoretically from the formula

$$f_r = \sqrt{\frac{2}{3}} \sqrt{\frac{\left(1 + \frac{s}{R}\right)^3 - 1}{\left(1 + \frac{s}{R}\right)^3}}\, f_p, \qquad (1)$$

where R is the probe radius, f_p is electron plasma frequency, and s is the sheath thickness given by $4.4\,\lambda_D$.[5] For the conditions at 0.4 μ at which the admittance runs were taken, this formula can be written approximately as $f_r \sim n^{.30}$ for electron temperature, T_e a constant. Experimentally we observe a variation of $f_r \sim I^{.26}$ but since $n \sim I^{.78}$ from Langmuir probe data, we derive $f_r \sim n^{.33}$. This shows excellent agreement between

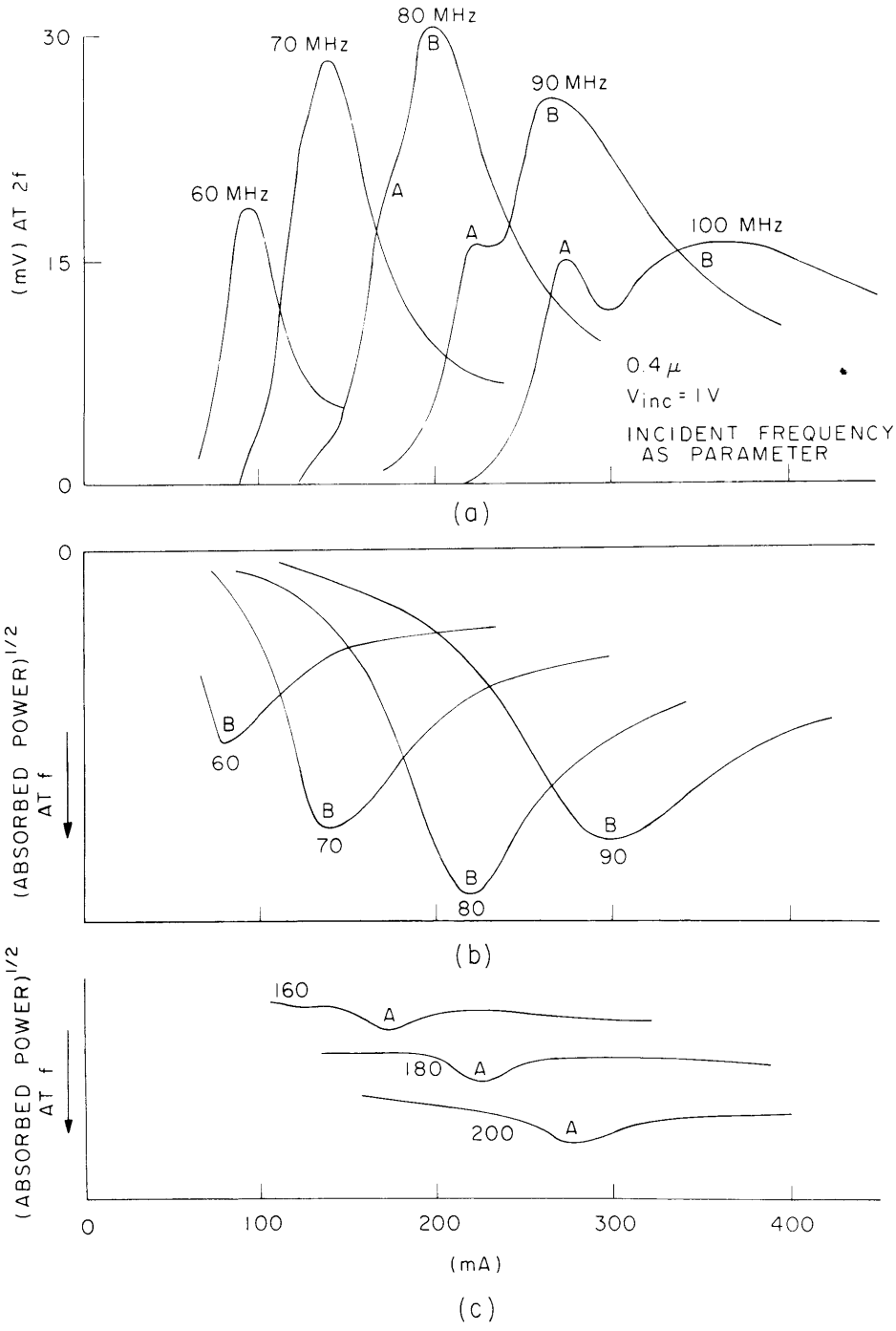

Fig. X-5. (a) Second harmonic as a function of density.
(b) Fundamental power reflected as a function of density.
(c) Harmonic power reflected as a function of density. (Zeros are displaced for clarity.)

theory and experiment. The precise positions of the resonant frequencies calculated from the same formula depend strongly on the value of density inserted for s and f_p.

Type B Peaks

If we put frequency f onto the antenna and look at the generation of frequency 2f by the plasma, or if we look at the reflected power from the plasma at f itself, both measurements being made as a function of plasma density, we observe effects that we previously called "type B" peaks[2] (see Fig. X-5). These results can then be correlated with the measurements at frequency f with the admittance meter.

a. Reflected Power from Plasma at Frequency f

In a simple series RLC circuit in which R, L, and C are independent of frequency ω, the minimum in the power reflected from the circuit occurs at the resonant frequency, where

$$G = \frac{R}{R^2 + \left(\omega L - \frac{1}{\omega C}\right)^2}$$

is a maximum and

$$B = \frac{\left(\omega L - \frac{1}{\omega C}\right)}{R^2 + \left(\omega L - \frac{1}{\omega C}\right)^2}$$

is zero. If, however, R, L, and C vary with frequency, then the minimum in reflected power does not have to occur at the resonance. This, in fact, is the case for the type B peaks observed in reflection at frequency f.

For experimental simplicity, the frequency is kept constant and the plasma density is varied instead. Since R, L, and C are functions of the density, the minimum in reflected power does not coincide with the conductance maximum (see Fig. X-6). The observed reflection curve at the fundamental f can be approximately generated from the observed admittance at the fundamental by using the formula

$$\left|\frac{V_{refl.}}{V_{inc.}}\right| = \sqrt{\rho\rho^*} = \left|\frac{Y_o - Y_L}{Y_o + Y_L}\right|, \qquad (2)$$

where ρ is the reflection coefficient, $\rho = (Y_o - Y_L)/(Y_o + Y_L)$, Y_o is the admittance of the 50-Ω cable, and Y_L is the measured admittance of the load that includes the inside capacitance of the dipole (see Fig. X-7).

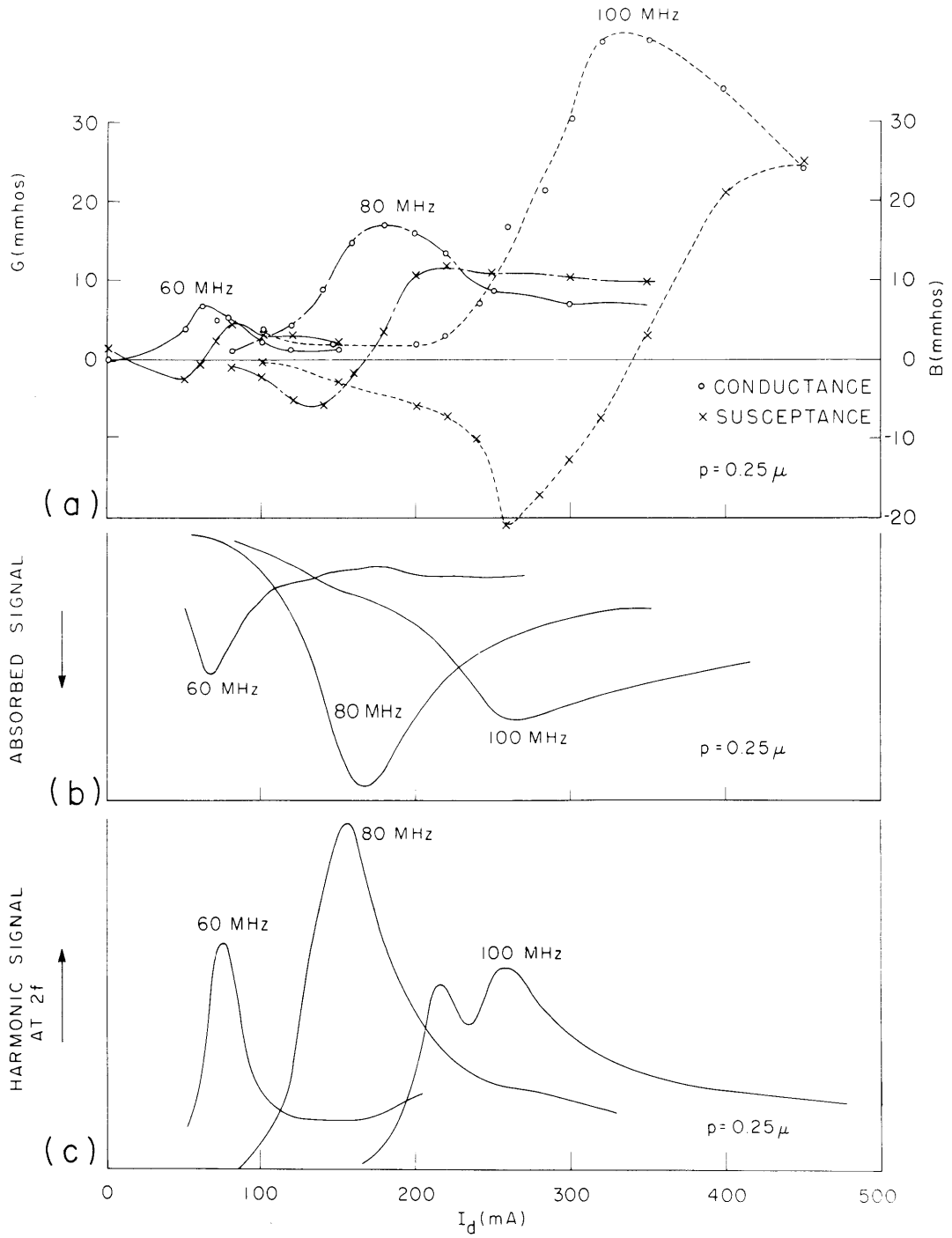

Fig. X-6. (a) Admittance as a function of discharge current for 60, 80, and 100 MHz.
(b) Absorbed power as a function of discharge current.
(c) Harmonic generation as a function of discharge current.

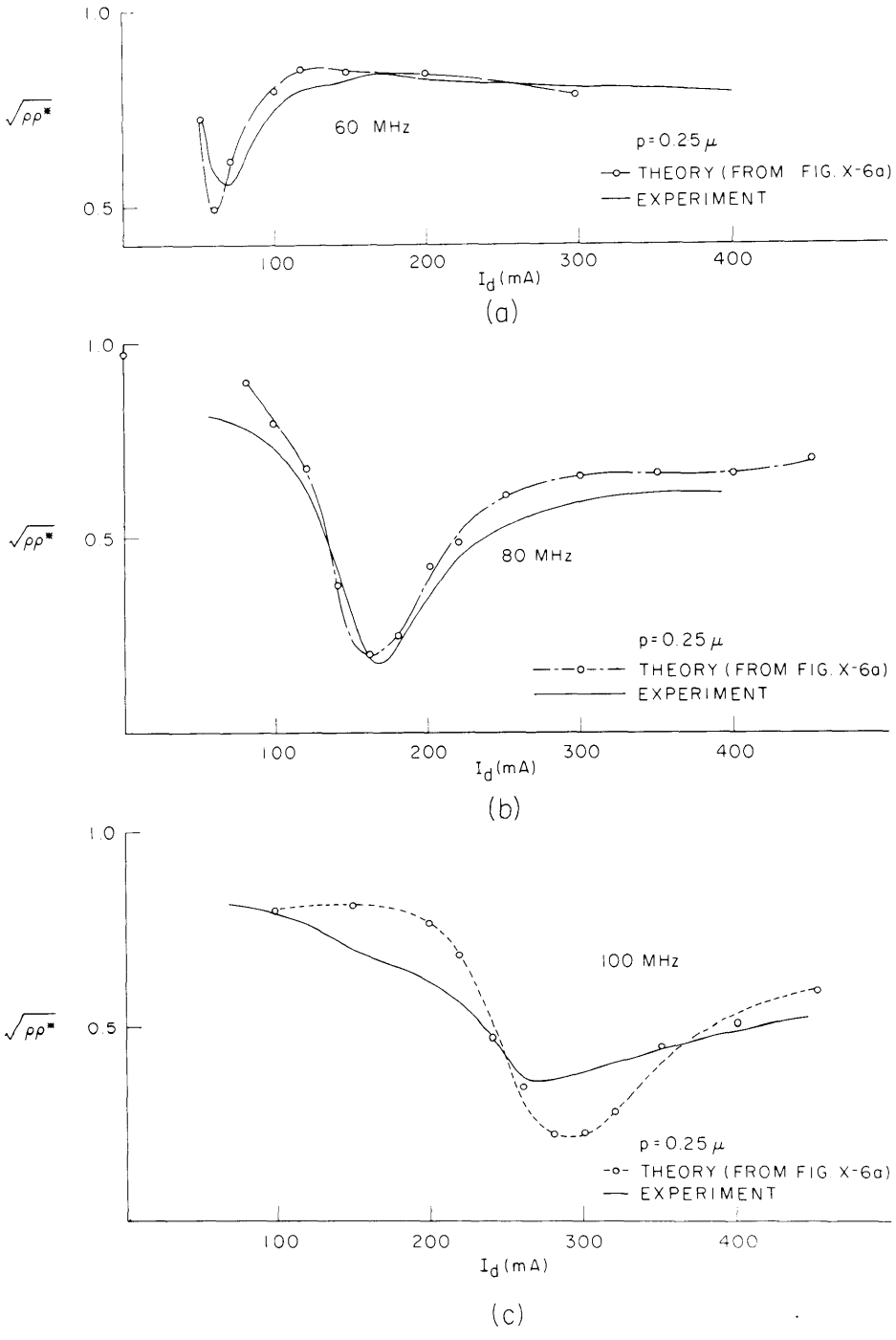

Fig. X-7. Reflected power as a function of discharge current: (a) at 60 MHz; (b) at 80 MHz; (c) at 100 MHz.

b. Generation of the Second Harmonic

If an RF signal is applied to a probe immersed in a plasma, then harmonics of that applied signal will be generated by the nonlinear exponential sheath. To explain the type B peak observed in the second harmonic, the admittance characteristics at the fundamental must be considered.

Since the harmonic is generated by rectification in the nonlinear exponential sheath, then the harmonic must peak when the voltage in the sheath is a maximum. The electron current to a probe is

$$I = ne\left(\frac{kT_e}{2\pi m_e}\right)^{1/2} e^{-eV/kT_e}. \tag{3}$$

Now, if $V = V_{DC} + V_{RF}$, where $V_{RF} = V_{sheath}$ at frequency f, then

$$I = I_{DC} \exp\left(\frac{-eV_{RF}}{kT}\right)$$

$$I = I_{DC}\left[1 + \frac{V_{RF}}{T_e} + \frac{1}{2}\frac{V_{RF}^2}{T^2} + \ldots\right]. \tag{4}$$

We are interested in the term in the expansion for I which varies at 2ω. For V_{RF}/T small, the series converges rapidly, and the only term that contributes significantly to $I(2\omega)$ is the $1/2\ (V_{RF}/T)^2$ term. The validity of this approximation for the experimental conditions is discussed in Appendix I. It is shown in Appendix II that $I(2\omega)$ is given by

$$I(2\omega) = \frac{I_{DC}}{4}\frac{|V_s(\omega)|^2}{T_e^2}. \tag{5}$$

If the voltage across the terminals of the dipole could be kept constant, then this sheath voltage would be largest at the admittance peak. Unfortunately, only the incident voltage can be kept constant. The terminal voltage equals the incident voltage plus the reflected voltage.

$$V_T = V_{inc.} + V_{refl.} = (1+\rho)V_{inc.} = \left(\frac{2Y_o}{Y_o + Y_L}\right)V_{inc.}. \tag{6}$$

Thus the terminal voltage drops as the resonance is approached. To determine the sheath voltage, a model more complex than the constant-voltage model used by others must be constructed.

The system may be modeled as shown in Fig. X-8. Then

$$V_s = I_p Z_s, \quad I_p = V_T Y_p, \quad V_T = \frac{2Y_o}{Y_o + Y_T} V_{inc.}$$

and so

$$V_s = \left(\frac{2Y_o}{Y_o + Y_T} \right) Y_p Z_s V_{inc.} \tag{7}$$

A value for V_s can then be obtained from the measured values of Y_T and Y_p and from a calculation for Z_s which is $\frac{1}{j\omega C_s}$ and C_s equals $4\pi\epsilon_o \frac{ab}{s}$, where a is the radius of the

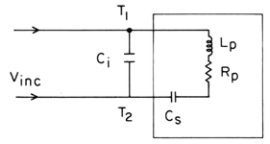

C_i = INSIDE CAPACITANCE OF DIPOLE

$Y_T = Y_p + j\omega C_i$

T_1, T_2 = TERMINALS ACROSS WHICH V_T IS DEVELOPED

Fig. X-8. Model for determining the terminal voltage.

antenna, s is the sheath size ($4.4\,\lambda_D$), and $b = a + s$. Since $C_s \sim 1/\lambda_D \sim n^{1/2}$, the ratio of sheath voltages for two different densities at a fixed frequency is

$$\frac{V_{s1}}{V_{s2}} = \left(\frac{Y_o + Y_{T2}}{Y_o + Y_{T1}} \right) \left(\frac{Y_{p1}}{Y_{p2}} \right) \left(\frac{n_2}{n_1} \right)^{1/2}, \tag{8}$$

where the various Y's are the values of admittances at frequency f. The ratio $|V_{s1}/V_{s2}|^2$ calculated from formula (8), by using the experimental values for Y_p, Y_T, and n, can be compared with the harmonic generation at 2f. The calculated and experimental peaks are close to each other. The calculated widths, however, are significantly larger than the observed widths.

This model was used to calculate the relative amplitudes of the second harmonic peaks for various frequencies, by using the experimentally determined values for the admittances. The theory and the experiment do not agree.

It should be noted that the comparisons above are valid only under the assumptions that the plasma admittance at the second harmonic is constant and that the only thing that determines the height and width of the B peaks is the variation of plasma admittance at the fundamental. These assumptions will be subject to further scrutiny.

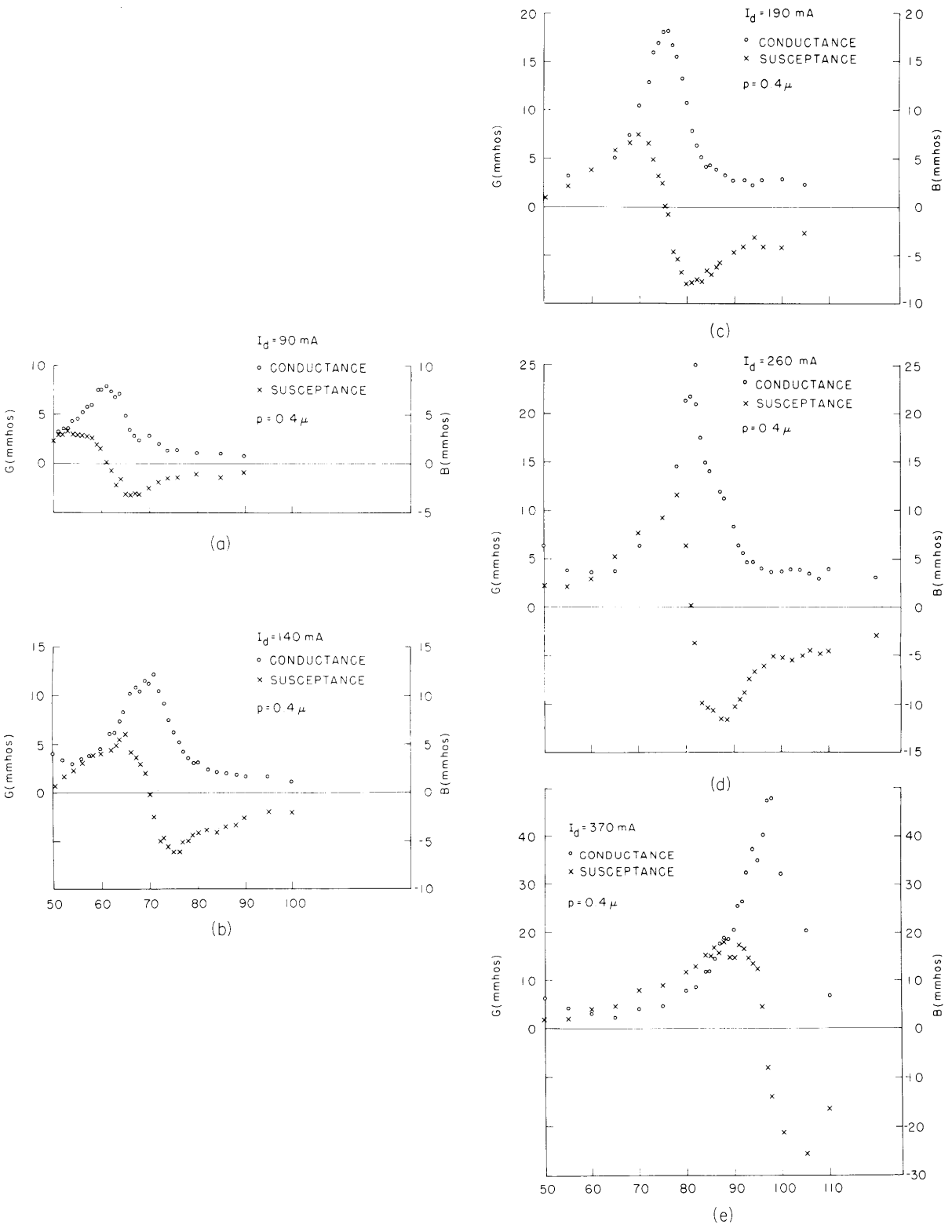

Fig. X-9. Admittance as a function of frequency.

Various Methods of Determining Series Resonance

Other investigators have measured resonance probe characteristics in three standard ways. They have used admittance meters,[5,6] observed transmitted or absorbed power,[7,8] and detected the extra rectified current to a biased probe when the radiofrequency is turned on.[8,9] This extra rectified current to the probe derives from the time average of Eq. 4, where V_{RF} is taken as $V_s \sin \omega t$. Then

$$\Delta I = \frac{I_{DC}}{4}\left(\frac{V_s}{T_e}\right)^2,$$

which is just the time average of Eq. 5. The heights of the resonance curves have been related to the damping by Buckley and others.[10,11] These methods have been compared and the positions of the resonances have been found to be equivalent in the regimes in which the experiments have been performed.[8,6]

The various methods may, in fact, be equivalent only over a limited range of currents, frequencies and pressures for which the Q of the resonance is not too high. At high Q's, the differences between these methods begin to show up.

As the resonant frequency is increased for a fixed pressure, the Q increases, as does the RF conductance as measured with the admittance meter (see Fig. X-9). It is seen, however, that the peak absorbed power at ω and the peak harmonic generation at 2ω (which should be equivalent to the extra rectified current) attain peak values, and then

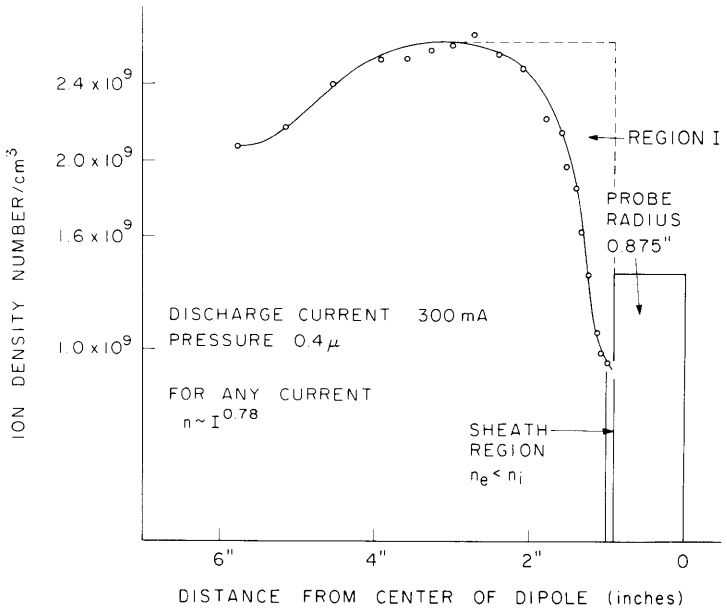

Fig. X-10. Density profile as determined by a Langmuir probe.

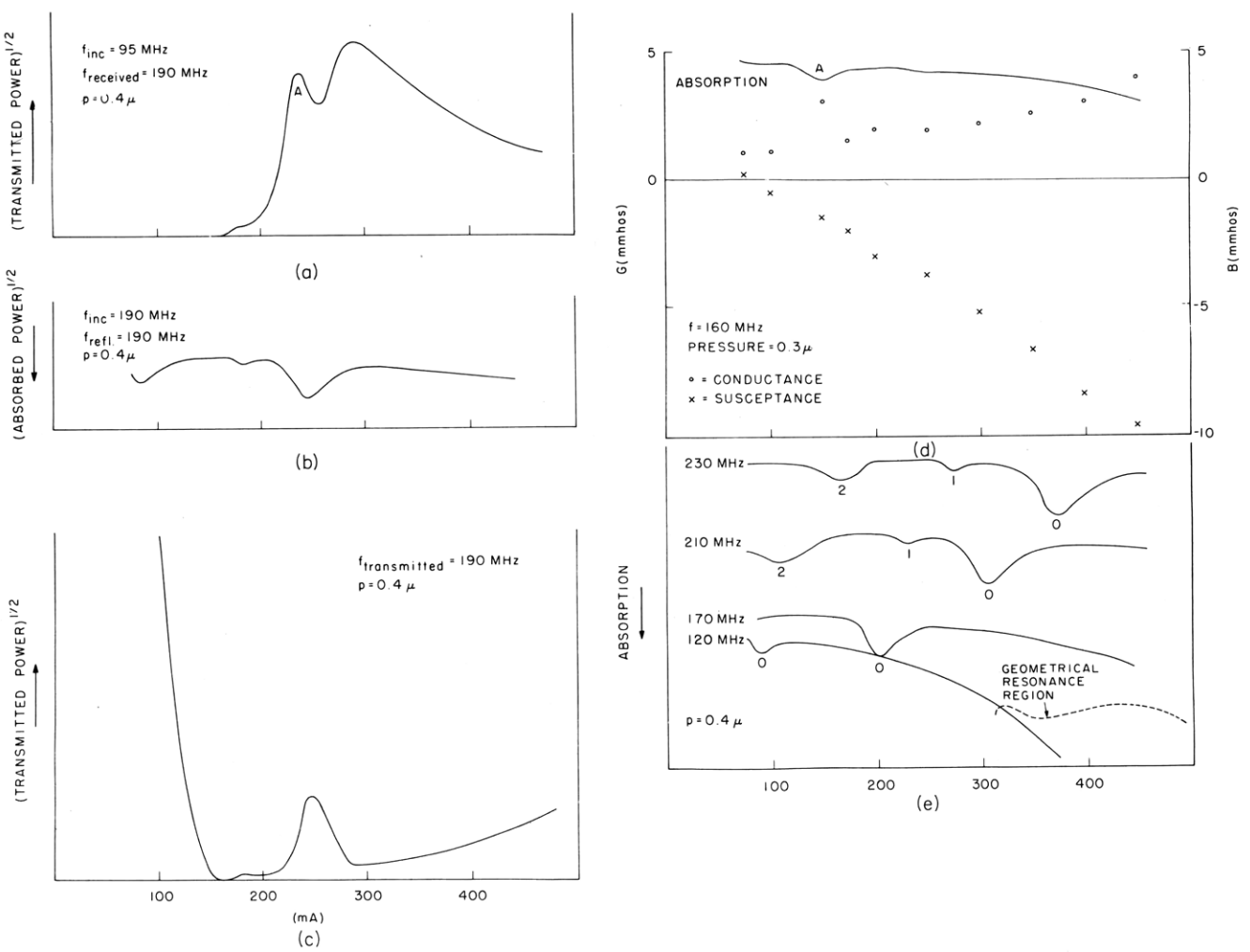

Fig. X-11. (a) Excitation of peak A by the harmonic.
(b) Absorption of peak A.
(c) Transmission at peak A.
(d) Absorption at 160 MHz compared with admittance at 160 MHz.
(e) Absorption of RF signal as a function of discharge current for various frequencies.

decrease as a function of ω (see Fig. X-5a and 5b and Fig. X-6b and 6c). Since the peak value of the RF conductance peak increases as expected for increasing resonance frequency and its position varies according to formula (1), then we expect that the RF admittance meter determination is the proper technique to use in a regime in which the various methods differ.

Type A Peaks

The solutions to the RF probe in a plasma are of two types: the long-wavelength solution in which the phase velocity is comparable to the vacuum electromagnetic velocity; and the short-wavelength solution in which the waves propagate at approximately the electron thermal velocity. The geometrical resonance and type B peaks were of the long-wavelength variety. We shall now consider the thermal waves.

The effects called "type A" previously[2] may result from a thermal standing wave that propagates between the dipole antenna and a point in the plasma for which $\omega = \omega_p(r)$. The wave equation[10] is $\omega^2 = \omega_p^2(r) + 3V_T^2k^2(r)$, where V_T is the electron thermal velocity, and k is the wave number of the oscillation. The wave becomes evanescent; that is, k becomes imaginary for $\omega < \omega_p(r)$. Standing waves of this type are known as Tonks-Dattner resonances, and have been discussed extensively by others.[12-14]

If we look at the radial density profile (Fig. X-10), measured with a thin cylindrical Langmuir probe operating in the orbital regime (see Sec. X-A. 3), we see that a region in which the Tonks-Dattner resonances could occur does exist for this probe-plasma system (region 1 of Fig. X-10).

A computer program is being prepared to predict the locations of the Tonks-Dattner resonances from the measured density profiles and electron temperatures. These solutions will be compared with the locations of the experimental type A peaks (see Fig. X-11).

Appendix I

In the expansion of Eq. 4, only the terms in even powers of V_s contribute to the second-harmonic current.

The term following $V^2/2T^2$ is $V^4/24T^4$. If V/T is small, then higher order terms, $n > 2$, may be neglected.

Let us see what V_s/T is for the case of maximum harmonic generation. If this is small, then the approximation should be valid everywhere. See Fig. X-6 for 80 MHz and 155 mA.

$$V_s = \frac{2Y_o}{Y_o + Y_L} \frac{Y_p}{Y_s} V_{inc.},$$

where Y_p = (13-3j) mmhos, and Y_L = (13+3j) mmhos.

$$Y_s = j\omega C_s \qquad C_s = \frac{4\pi\epsilon_o ab}{s},$$

where $s = 4.4\lambda_D$, a = radius of the probe, and b = a + s.

For T = 4.0 eV and $n_s = n_o/4 = 4 \times 10^8/cm^2$.

$j\omega C_s = 8.5j$ mmhos.

$|V_s| = 1.9\, V_{inc.}$ but $V_{inc.} = 0.5$ V.

$\frac{V_s}{T_e} \sim \frac{1}{4}$, and the fourth-order contribution will be negligible.

Appendix II

The applied signal is $V_{inc.} \sin \omega t$. Then V across the sheath is given by

$$V_s = \frac{2Y_o}{Y_o + Y_L} Y_p Z_s V_{inc.}$$

$$V_s = V_r \sin \omega t + V_i \cos \omega t$$

$$V_s^2 = V_r^2 \sin^2 \omega t + V_i^2 \cos^2 \omega t + 2V_r V_i \sin \omega t \cos \omega t,$$

but

$$\sin^2 \omega t = \frac{1 - \cos 2\omega t}{2}, \qquad \cos^2 \omega t = \frac{1 + \cos 2\omega t}{2}$$

$$2 \sin \omega t \cos \omega t = \sin 2\omega t$$

$$V_s^2 = \frac{1}{2}\left\{V_i^2 \cos 2\omega t - V_r^2 \cos 2\omega t + 2V_r V_i \sin 2\omega t.\right.$$

Then, from Eq. 4,

$$I(2\omega) = \frac{I_{DC}}{4T^2}\left\{\left(V_i^2 - V_r^2\right) \cos 2\omega t + 2V_r V_i \sin 2\omega t\right\},$$

but we measure $|I(2\omega)|$, so

$$|I(2\omega)| = \frac{I_{DC}}{4T^2}\left\{V_r^2 + V_i^2\right\} = \frac{I_{DC}}{4}\frac{|V_s|^2}{T^2}.$$

A. J. Cohen

References

1. A. J. Cohen, Quarterly Progress Report No. 85, Research Laboratory of Electronics, M.I.T., April 15, 1967, p. 103.
2. A. J. Cohen, Quarterly Progress Report No. 90, op. cit., July 15, 1968, pp. 76-82.
3. J. A. Waletzko, Quarterly Progress Report No. 79, op. cit., October 15, 1965, p. 95.
4. J. A. Waletzko, Quarterly Progress Report No. 80, op. cit., January 15, 1966, p. 103.
5. J. A. Waletzko and G. Bekefi, Radio Science (New Series), Vol. 2, No. 5, p. 489, May 1967.
6. R. S. Harp and F. W. Crawford, J. Appl. Phys. 35, 3436 (1964).
7. A. M. Messiaen and P. E. Vandenplas, J. Appl. Phys. 37, 1718 (1966).
8. D. Lepechinsky, A. Messiaen, and P. Rolland, CEA (Paris)-R2945 (1964).
9. H. Ikegami and K. Takayama, IPPJ-10 (Nagoya), 1963.
10. R. Buckley, J. Plasma Phys. 1 (Pt. 2), 171 (1967).
11. P. G. Davies, Proc. Phys. Soc. (London) 88, 1019 (1966).
12. A. Dattner, Ericsson Technics 2, 310 (1957).
13. F. C. Hoh, Phys. Rev. 133, A1016 (1964).
14. H. J. Schmitt, Appl. Phys. Letters 4, 111 (1964).

5. RADIATION TEMPERATURE OF EXTRAORDINARY WAVES

Observations have been made in this laboratory of the effective temperature, $T_r(\omega)$, of microwave radiation emitted from weakly ionized gas discharges.[1-4] In the presence of an external magnetic field, $\vec{B}$, resonant peaks in $T_r(\omega)$ were observed at the electron-cyclotron frequency $\omega = \omega_c = eB/m$ (in MKS units.) A theoretical model for this behavior was obtained by treating the steady-state intensity of radiation as a balance between the emission and absorption (by orbiting electrons) of right circularly polarized (resonant) electromagnetic waves propagating in the direction of $\vec{B}$. The resultant expression for the effective temperature of the radiation is

$$kT_r(\omega) = \frac{\int_0^\infty \frac{v^4 \nu_m}{(\omega-\omega_c)^2 + \nu_m^2} f(v)\, dv}{\int_0^\infty \frac{v^4 \nu_m}{(\omega-\omega_c)^2 + \nu_m^2} \left[-\frac{1}{mv}\frac{\partial f}{\partial v}\right] dv} \tag{1}$$

where k is Boltzmann's constant, $\nu_m(v)$ is the electron-atom collision frequency for momentum transfer, and f(v) is the (isotropic) electron velocity distribution function normalized so that $4\pi \int_0^\infty v^2 f\, dv = 1$. Both the numerator and denominator (representing coefficients of emission and absorption of right circular waves) exhibit resonant behavior at $\omega = \omega_c$ and, if $\nu_m(v)$ is not constant and f(v) is not Maxwellian, their ratio, $T_r(\omega)$ is resonant also. The model neglects warm plasma effects (for example, Doppler broadening) and assumes that electron collisions with neutral particles predominate. Because of its manifest simplicity, Eq. 1 has always been used – sometimes with remarkable success – in the analysis of resonant temperature data.[4,5] In the guided-wave systems normally employed in these experiments, however, the claim that right circularly polarized radiation is being monitored exclusively cannot be made. Furthermore, for waves propagating at an angle to the magnetic field, the wave resonant frequency (at which the wave phase velocity becomes quite large) is different from the electron-cyclotron frequency. Because of these potential influences, we have undertaken a study of the validity of (1) for other resonant polarizations.

A more general expression for $T_r(\omega)$, one which explicitly includes the wave polarization, may be based upon the theory of fluctuations. It is found that for weakly damped modes in a plasma confined by conducting walls (say, a waveguide) an effective radiation temperature may be defined by[4]

$$kT_r(\omega) = \pi \frac{\int \vec{E}^*(\vec{r}, \omega) \cdot \overleftrightarrow{\phi}(\vec{r}, \omega) \cdot \vec{E}(\vec{r}, \omega)\, d^3r}{\int \vec{E}^*(\vec{r}, \omega) \cdot \overleftrightarrow{\sigma}_H(\vec{r}, \omega) \cdot \vec{E}(\vec{r}, \omega)\, d^3r}, \tag{2}$$

where $\vec{E}(\vec{r}, \omega)$ is the wave electric field (assumed to vary as $e^{i\omega t}$), $\overleftrightarrow{\phi}(\vec{r}, \omega)$ is the microscopic current correlation dyadic, and $\overleftrightarrow{\sigma}_H(\vec{r}, \omega)$ is the Hermitian part of the conductivity tensor, $\overleftrightarrow{\sigma}$. The two integrals are taken over the plasma volume, and it has been assumed here that $\overleftrightarrow{\phi}$ and $\overleftrightarrow{\sigma}$ reflect only local behavior (cold-plasma limit). The expression (2) represents the average energies of fluctuating modes in the system as a balance between their rate of emission by random electron motion (the numerator) and their ohmic dissipation through the induced, in-phase current. In the case of a weakly ionized gas with a uniform magnetic field in the z-direction, all expressions are simplified by transformation to right and left circular coordinates:

$$\sqrt{2}\, E_r = E_x - iE_y, \qquad \sqrt{2}\, E_\ell = E_x + iE_y.$$

This transformation diagonalizes the tensors $\overleftrightarrow{\phi}$ and $\overleftrightarrow{\sigma}$, and for a uniform plasma we may write

$$kT_r(\omega) = \pi \frac{|E_r|^2 \phi_r + |E_\ell|^2 \phi_\ell + |E_z|^2 \phi_z}{|E_r|^2 \sigma_{Hr} + |E_\ell|^2 \sigma_{H\ell} + |E_z|^2 \sigma_{Hz}}. \tag{3}$$

The appropriate form of the components of $\overleftrightarrow{\phi}$ has been obtained by Bunkin[6]

$$\phi_{r,\ell} = \frac{4ne^2}{3} \int_0^\infty \frac{v^4 \nu_m}{(\omega \mp \omega_c)^2 + \nu_m^2} f(v)\, dv \tag{4}$$

ϕ_z = the same expression with $\omega_c = 0$.

Here n is the electron number density. Similarly, for the components of the diagonalized conductivity tensor

$$\sigma_{r,\ell} = \frac{4\pi ne^2}{3} \int_0^\infty \frac{v^4}{i(\omega \mp \omega_c) + \nu_m} \left[-\frac{1}{mv} \frac{\partial f}{\partial v} \right] dv \tag{5}$$

σ_z = the same expression with $\omega_c = 0$.

The components of the Hermitian tensor $\overleftrightarrow{\sigma}_H$ are simply the real parts of (5). Combining (4) and (5) with (3), we recover the original result (1) for $T_r(\omega)$ in the case of pure right circular polarization: $E_\ell = E_z = 0$.

In the interpretation of temperature measurements of guided electromagnetic waves, the form of $\vec{E}(\vec{r}, \omega)$ in the plasma column is not known. We can argue, however, that the component E_r is probably comparable to E_ℓ and E_z so that for $(\omega - \omega_c)^2 < \nu_m^2$ the right circular terms in (3) dominate the nonresonant terms by a factor of $4\omega_c^2/\nu_m^2$, which is

generally quite large. Whereas this argument is often valid and there may even be experimental evidence of significant resonant polarization,[7] its range of validity off resonance may be questioned, and we can hypothesize cases for which it might not apply at all. One such case is that of the so-called extraordinary wave encountered when the direction of propagation is perpendicular to the magnetic field. It has the property that, in the absence of collisions, its right circular component, E_r, vanishes at $\omega = \omega_c$. Furthermore, its refractive index (and correspondingly its emission and absorption coefficients) are greatest at the hybrid frequency, $\omega_H = \left(\omega_p^2 + \omega_c^2\right)^{1/2}$, where ω_p is the plasma frequency: $\omega_p^2 = ne^2/\epsilon_o m$. Thus for dense plasmas we might expect no resonant behavior in the intensity of extraordinary radiation at $\omega = \omega_c$ and might even anticipate an anomaly in $T_r(\omega)$ near ω_H.

A computer program was written to rigorously examine this question. We used the forms $f(v) = f_o \exp[-(v/v_o)^p]$ and $\nu_m(v) = Cv^q$, where v_o, C, p, and q are arbitrary constants, to calculate the conductivity from (5). For a given angle of propagation relative to the magnetic field, the components of $\vec{E}(\omega)$ were obtained from the wave equation

$$\vec{\kappa} \times (\vec{\kappa} \times \vec{E}) + \left(\frac{\omega}{c}\right)^2 \overleftrightarrow{K} \cdot \vec{E} = 0,$$

where $\overleftrightarrow{K}(\omega) = \overleftrightarrow{I} + \overleftrightarrow{\sigma}/i\omega\epsilon_o$ is the dielectric tensor, and $\vec{\kappa}$ is the propagation vector. The resultant values were then combined with the appropriate components of (4) and (5) to obtain $kT_r(\omega)$ from (3). The results of two such calculations (for right circular and extraordinary waves) are shown in Fig. X-12. Because the forms adopted for f(v) and $\nu_m(v)$ contain an arbitrary velocity scale that does not affect the form of $T_r(\omega)$, that quantity is plotted relative to the kinetic effective temperature: $kT_k = \frac{1}{3} m(v_T)^2$, where v_T is the rms electron velocity. Similarly, the scale of frequencies has been removed through use of dimensionless plasma parameters[8]: for the electron density, $\alpha = \omega_p/\omega$; for the magnetic field, $\beta = \omega_c/\omega$; and for the velocity-dependent collision frequency, $\gamma(v) = \nu_m(v)/\omega = \gamma_o(v/v_T)^q$. In keeping with experimental practice, we plot T_r as a function of magnetic field for fixed ω.

The parameters chosen for the case illustrated in Fig. X-12 are typical of experiments performed with argon discharges. Apart from a slight asymmetry, the effective radiation temperature for the extraordinary polarization is resonant at the electron cyclotron frequency (β=1) and exhibits no anomalies at the hybrid frequency (β=0.7). Indeed, the difference between the pure right circular and extraordinary polarizations, for the most part, is within experimental error.

To understand the physics underlying this result, the two nonzero components of $\vec{E}(\omega)$ in the extraordinary case are plotted in Fig. X-13a. The field amplitude has been normalized so that $|\vec{E}|^2 = |E_r|^2 + |E_\ell|^2 = 1$. For comparison we show the corresponding plot for a collisionless wave (γ=0). In spite of their similarity, these curves differ

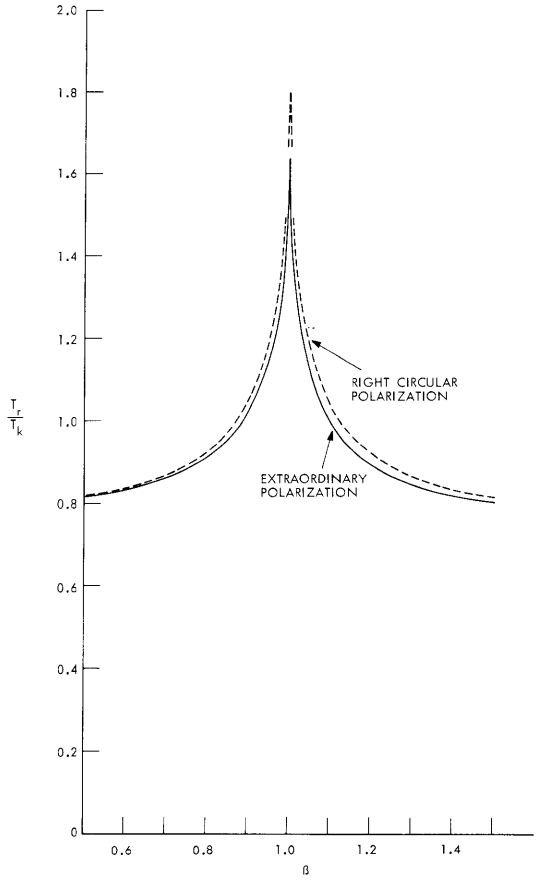

Fig. X-12. Computed radiation temperature as a function of $\beta = \omega_c/\omega$ for propagation parallel and perpendicular to the magnetic field. $f = f_o \exp[-(v/v_o)^4]$, $\gamma = 0.1\ (v/v_T)^3$, $\alpha^2 = (\omega_p/\omega)^2 = 0.5$.

importantly, in that $|E_r|^2$ is nonzero at $\omega = \omega_c$ when collisions are included. The right and left components of $\pi\overleftrightarrow{\phi}$ and $\overleftrightarrow{\sigma}_H$ are shown in Fig. 13b. Note that $\sigma_{H\ell}$ and $\pi\phi_\ell$ are quite small in comparison with σ_{Hr} and $\pi\phi_r$ and here are shown magnified by a factor of 100. The total emission and absorption terms (numerator and denominator of (3)) are presented in Fig. X-13c. The hybrid resonance appears as a broad maximum in both terms near $\beta = 0.7$ but the velocity-dependent collision frequency manifests itself in additional structure at $\beta = 1$. That the right circular terms clearly dominate the behavior of $T_r(\omega)$ in this case can be seen from the smallness of the left circular terms that are plotted for comparison. It is not surprising then that the resulting radiation temperature is only slightly different from that obtained from the right circular terms alone (see Fig. X-12).

Clearly, the appearance of the electron-cyclotron resonance in the extraordinary-wave

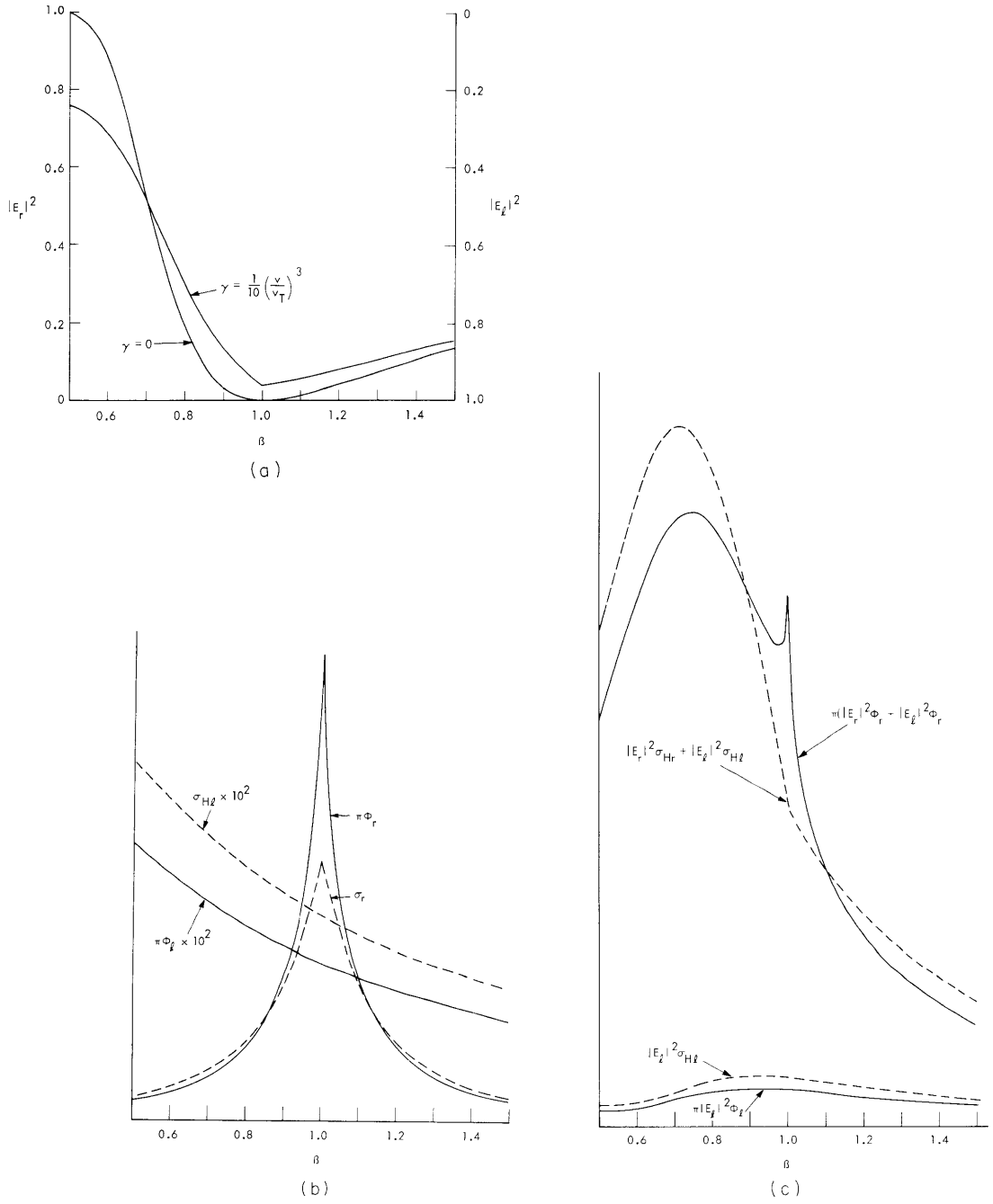

Fig. X-13. (a) Right and left circularly polarized components of the extraordinary wave electric field with $a^2 = 0.5$. (1) Without collisions. (2) Under the conditions of Fig. X-12.
(b) Dependence upon β of right and left circular components of $\vec{\phi}$ and $\overleftrightarrow{\sigma}_H$. Parameters as in Fig. X-12.
(c) Dependence upon β of the numerator and denominator of Eq. 3 illustrating hybrid and cyclotron resonances. The nonresonant contributions are also shown. Parameters as in Fig. X-12.

temperature is related to the influence of collisions on $|E_r|^2$ and to the general dominance of $|E_r|^2 \sigma_{Hr}$ and $|E_r|^2 \phi_r$ over $|E_\ell|^2 \sigma_{H\ell}$ and $|E_\ell|^2 \phi_\ell$ near $\beta = 1$. The relative magnitudes of these terms may be estimated by assuming that $\nu_m(v)$ is constant. In so doing we discard the resonant peak in $T_r(\omega)$, but preserve the magnitudes of the terms in question. For the extraordinary wave, the circular field components are simply related[8]

$$\frac{E_r}{E_\ell} = -\frac{K_\ell}{K_r},$$

where, for $\gamma(v)$ = constant,

$$K_{r,\ell} = \frac{1 \mp \beta - i\gamma - a^2}{1 \mp \beta - i\gamma}.$$

Furthermore, in this case, the components of $\overleftrightarrow{\phi}$ and $\overleftrightarrow{\sigma}_H$ are proportional, with

$$\frac{\sigma_{Hr}}{\sigma_{H\ell}} = \frac{\phi_r}{\phi_\ell} = \frac{(1+\beta)^2 + \gamma^2}{(1-\beta)^2 + \gamma^2}.$$

Working out the details, we therefore find that the ratio of the resonant terms in (3) to the nonresonant terms is given by

$$R = \frac{|E_r|^2 \phi_r}{|E_\ell|^2 \phi_\ell} = \frac{(1+\beta-a^2)^2 + \gamma^2}{(1-\beta-a^2)^2 + \gamma^2}. \tag{6}$$

If R is large (say, greater than 10) over the range of the resonant peak in $T_r(\omega)$, then the simple expression (1) could be used for the interpretation of experimentally observed extraordinary intensities. Taking its range as extending from $\beta = 1 - \gamma$ to $\beta = 1 + \gamma$, we plot in Fig. X-14 the minimum value of R in the resonance region as a function of the parameters a^2 and γ. It is seen that for $\gamma < 0.2$, R is suitably large for $a^2 < 0.5$. The example that we have cited with $\gamma_o = 0.1$ and $a^2 = 0.5$ corresponds at resonance to R = 9, and we should therefore expect a 10% difference between the extraordinary and right circular versions of $T_r(\omega)$. This is borne out by Fig. X-12 at the point $\beta = 1$, but off resonance the agreement improves as the r and ℓ components of $\overleftrightarrow{\sigma}_H$ and $\overleftrightarrow{\phi}$ become proportional in the limit $(\omega-\omega_c)^2 \gg \nu_m^2$.

In our calculations we have also examined the resonant waves that propagate at angles other than 0° and 90° relative to $\vec{B}$. In all respects, they are intermediate between the right circular and extraordinary cases cited here. We also considered the nonresonant polarizations which vary from the pure left circular wave at 0° to the "ordinary" wave

at 90°. For these cases the wave fields generally contain only a slight amount of E_r, and the radiation temperature does not vary dramatically.

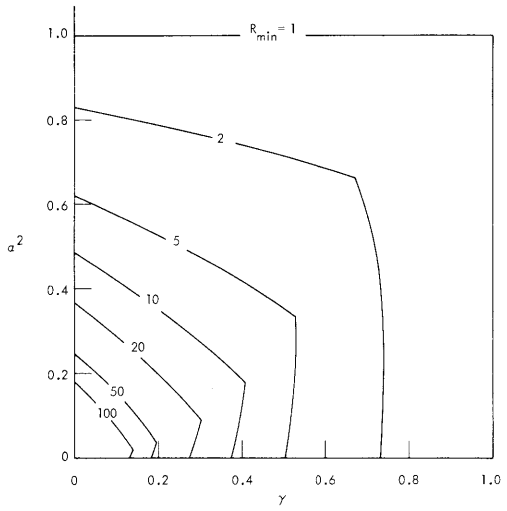

Fig. X-14.

Dependence on α^2 and γ of the minimum value of $R = |E_r|^2 \phi_r / |E_\ell|^2 \phi_\ell$ in the range from $\beta = 1 - \gamma$ to $\beta = 1 + \gamma$. Reduced collision frequency, γ, assumed independent of electron velocity.

Our initial concern has been with the radiation of guided waves in the neighborhood of the electron-cyclotron frequency. These waves are not pure plane waves and the suggestion that (1) may be correctly applied if $4\omega_c^2 \gg \nu_m^2$ is probably still valid. As a potential counterexample we have treated the extraordinary polarization and found that $T_r(\omega)$, if properly measured, would be resonant at $\omega = \omega_c$, even though the rates of emission and absorption are maximum elsewhere. Indeed (1) could be used with little error for moderate plasma densities. This is true in the collisionless limit $\gamma \to 0$ (see Eq. 6), even though this implies $E_r \to 0$ at $\omega = \omega_c$. A related question arises from studies of the anomalous emission of microwaves from noble-gas discharges. Even in dense plasmas, the observed radiation is well tuned to the electron-cyclotron frequency.[9] The phenomenon is thought to involve the negative absorption of extraordinary waves, and it seems apparent that as f(v) and $\nu_m(v)$ are varied the denominator of (3) will first become negative at the particle resonance, $\omega = \omega_c$, rather than at the wave resonance, $\omega = \omega_H$. Computer programs are being written to pursue this and related problems.

A. C. Reisz, B. L. Wright

References

1. H. Fields, G. Bekefi, and S. C. Brown, Phys. Rev. 129, 506 (1961).
2. G. Bekefi, Radiation Processes in Plasmas (John Wiley and Sons, Inc., New York, 1966).
3. B. L. Wright, Quarterly Progress Report No. 80, Research Laboratory of Electronics, M.I.T., January 15, 1966, p. 99.

4. B. L. Wright, "Measurement of the Time-Dependent Electron Velocity Distribution of a Plasma," Ph. D. Thesis, Department of Physics, M. I. T., June 1967.

5. B. L. Wright, Quarterly Progress Report No. 83, Research Laboratory of Electronics, M. I. T., October 15, 1966, p. 59.

6. F. V. Bunkin, Soviet Phys. – JETP 14, 206 (1961).

7. B. L. Wright, Quarterly Progress Report No. 76, Research Laboratory of Electronics, M. I. T., January 15, 1965, p. 81.

8. W. P. Allis, S. J. Buchsbaum, and A. Bers, Waves in Anisotropic Plasmas (The M. I. T. Press, Cambridge, Mass., 1963).

9. C. Oddou, Quarterly Progress Report No. 93, Research Laboratory of Electronics, M. I. T., April 15, 1969, p. 93.

6. DEVELOPMENT OF THE CASCADE IN LASER-PRODUCED PLASMAS

According to one physical picture of the process,[1] the breakdown of gases at the focus of a high-intensity laser occurs in three stages:

(a) A few initial free electrons appear, probably produced by low-order multiphoton ionization of impurities.

(b) A "cascade" of free electrons develops. In this stage, each free electron absorbs energy from the photon field during collisions with the massive neutrals. The number density of free electrons multiplies because those electrons that have gained enough energy to do so collide with and ionize the neutral atoms.

(c) When the electron and ion densities become great enough, nonlinear processes begin to dominate the cascade as follows:

(i) Collisions of free electrons with ions. Because the cross section for this process is greater than that for collisions with neutrals, the electrons gain energy more rapidly, and the growth rate is enhanced.

(ii) Electron-electron thermalization. This tends to fill out the high-energy tail of the electron distribution function, so that this process also increases the ionization rate.

(iii) Ambipolar diffusion. This decreases the effectiveness of one loss process.

All of these act to enhance the growth of the cascade, while the competing nonlinear process of recombination remains negligible. Thus, as soon as the breakdown reaches this third stage, it almost certainly goes to completion. (In support of the existence of this third stage, the data of Young and Hercher[1] show a discontinuity in the amount of charge collected near the threshold laser-beam power.)

A consequence of this physical picture is that it is stage (b) (linear growth of the cascade) that mainly determines the threshold for breakdown. Once stage (c) is reached, the cascade goes to completion; while the elimination of stage (a) does not seem to affect the threshold. (Young and Hercher's data show that using a low-grade discharge to provide, say, 100-1000 free electrons in the focal volume does not noticeably lower the threshold.)

Analogy with High-Frequency Microwave Breakdown

This report presents a calculation of gain and loss rates in stage (b) based on the Boltzmann equation as analyzed by Allis.[2] In his treatment, the distribution function, electric field intensity, and collision integrals are Fourier-analyzed in time and expanded in spherical harmonics in velocity space. For our purposes, the result may be written

$$\frac{\partial F}{\partial t} = \frac{1}{6v^2}\frac{\partial}{\partial v}\left[v^2 \frac{e^2 \mathscr{E}_p^2}{m^2} \frac{\nu_m}{\omega^2 + \nu_m^2} \frac{\partial F}{\partial v}\right]$$

$$+ \frac{m}{M+m}\frac{1}{v^2}\frac{\partial}{\partial v}\left[v^2 \nu_m(v)\left(F + \frac{kT_g}{mv}\frac{\partial F}{\partial v}\right)\right]$$

$$- [\nu_x(v)+\nu_i(v)]F + \xi(v)\,F + \frac{v^2\nabla^2 F}{3\nu_m}, \qquad (1)$$

where

$F(\underline{v}, \underline{r}, t)$ = the spherically symmetric DC component of the electron velocity-space-time distribution function;

v, e, m = the electron speed, charge, mass;

M, T_g = the mass, temperature of the unperturbed neutral gas;

$\nu_m(v)$ = the electron-atom collision frequency for momentum transfer;

$\nu_x(v), \nu_i(v)$ = the excitation and ionization collision frequencies for electrons incident on atoms;

$\xi(v)\,F$ = the rate at which slow electrons reappear, because of inelastic collisions of high-speed electrons;

$\mathscr{E}_p$ = the peak electric field strength — a function of space and time;

ω = the angular frequency of the incident radiation.

This equation treats the photon field classically; it makes no provision for the discreteness of photon energies, which are approximately 5-10 per cent of gas ionization energies.

In extending this theory to the case of laser-produced plasmas, we must note, among others, the following conditions:

1. The field is not uniform in space. This results in an uneven rate of growth for the electron density. Since the rate of growth is fastest at the center, this condition may enhance diffusion losses.

2. The field is not uniform in time. In microwave terms, the field is pulsed, rather than cw. We must therefore compute and integrate the net gain over the duration of the pulse in order to predict the threshold.

Also, we may expect this theory to be valid only provided that the mean-free path of the free electrons, and the amplitude of their oscillations, are both small compared with the characteristic dimensions of the discharges.[3]

For the present, these computations will be restricted to helium, for the following reasons: (a) The collision frequency in helium is very nearly constant as a function of electron speed.[3] This simplifies Eq. 1 considerably. (b) Fairly exact measurements

exist for the inelastic (excitation and ionization) cross sections of helium.[4] (c) Next to hydrogen, helium is the simplest atom known. This means that oscillator strengths have been calculated in a number of different approximations,[5] so that, if necessary, one may guess appropriate radiative rates a little more confidently. (d) Helium is monatomic, so that there are no low-lying rotational or vibrational molecular states. In principle, however, other gases could also be treated by the present theory.

As a first approximation to the solution, we may reduce Eq. 1 to an ordinary differential equation in two steps.

Step 1

Let

$$F(v, \underline{r}, t) = e^{\int^t \nu(t)\,dt}\, h(v, \underline{r}, t). \tag{2a}$$

Then

$$\frac{1}{F}\frac{\partial F}{\partial t} = \nu(t) + \frac{1}{h}\frac{\partial h}{\partial t}.$$

Our first approximation is to write

$$\frac{1}{F}\frac{\partial F}{\partial t} \approx \nu(t); \tag{2b}$$

that is, we assume $\partial \ln h/\partial t$ to be small.

Step 2

Extending the same analysis to nonuniformity in space, we write quite generally

$$h(v, \underline{r}, t) = f(\underline{r})\, g(v, \underline{r}, t) \tag{3a}$$

$$\frac{\nabla^2 h}{h} = \frac{\nabla^2 f}{f} + 2\,\frac{\vec{\nabla} f}{f}\cdot\frac{\vec{\nabla} g}{g} + \frac{\nabla^2 g}{g}.$$

Let

$$\frac{\nabla^2 f}{f} = -\frac{1}{\Lambda^2(\underline{r})}.$$

Then we make the second approximation:

$$\frac{\nabla^2 h}{h} \approx -\frac{1}{\Lambda^2(\underline{r})}, \tag{3b}$$

where the terms ignored are of order $\Lambda^{-1} \left| \underline{\nabla} \ln g \right|$. It is not obvious that these two approximations are valid; their validity must be checked against the solutions that they yield. But Eq. 1 now becomes (locally and instantaneously) an ordinary differential equation for g as a function of v. Furthermore, if we choose to normalize g(v) independently of the electron number density,

$$\int_0^\infty g(v)\, v^2\, dv = \frac{1}{4\pi},$$

then the parameters $\nu(t)$ and $\Lambda(\underline{r})$ reflect the growth and spatial distribution of the number density itself.

We may simplify the appearance of (1) by introducing the following grouped variables:

$$v_T^2 = \frac{1}{m}\left[\frac{M}{\nu_m^2 + \omega^2}\,\frac{e^2 \mathscr{E}_p^2}{6m^2} + kT_g\right]$$

$$v_D^2 = 3\mu\nu_m^2\Lambda^2$$

$$\mu = \frac{m}{M+m} \approx \frac{m}{M}$$

$$\theta = \frac{\nu}{\mu\nu_m}$$

$$kf_{nm}(v) = \frac{1}{\mu\nu_m}\,\xi(v)\, g(v)$$

$$h_\mu^{x,i}(v) = \frac{1}{\mu\nu_m}\,\nu_{x,i}(v).$$

At the same time, we take advantage of the function g(v) introduced by (2) to write the following ordinary differential equation for the reduced distribution function:

$$\frac{1}{v^2}\,\frac{d}{dv}\left[v^2 v_T^2\,\frac{dg}{dv} + v^3 g\right] - \frac{v^2}{v_D^2}\, g = \left[h_\mu^i(v) + h_\mu^x(v)\right] g + \theta g - kf_{nm}(v).$$

For convenience, we normalize

$$\int_0^\infty f_{nm}(v)\, v^2\, dv = \int_0^\infty g(v)\, v^2\, dv = \frac{1}{4\pi}.$$

For the sake of comparison with the theory of high-frequency microwave discharges, we

note that v_T corresponds roughly to the concept of an effective electric field, while v_D is proportional to the "dimensionless" variable $P\Lambda$.[3]

The parameters k and θ are still unknown. To solve for these self-consistently, we may impose further conditions on the parameters of (4) on physical grounds. Multiplying by v^2 and integrating, we obtain

$$4\pi \left[v^2 v_T^2 \frac{dg}{dv} + v^3 g \right]_0^\infty = \langle h_\mu^x \rangle + \langle h_\mu^i \rangle + \theta - k + \frac{\langle v^2 \rangle}{v_D^2}, \tag{5}$$

where for an arbitrary function s(v)

$$\langle s \rangle \equiv 4\pi \int_0^\infty s(v)\, g(v)\, v^2\, dv.$$

Now k is the (reduced) rate at which slow electrons appear following high-speed inelastic collisions:

$$k = \langle h_\mu^x \rangle + 2\langle h_\mu^i \rangle. \tag{6}$$

Furthermore, the growth rate θ should represent the difference between the ionization rate and the diffusion loss rate:

$$\theta = \langle h_\mu^i \rangle - \frac{\langle v^2 \rangle}{v_D^2}. \tag{7}$$

Finally, we expect g to vanish rapidly at ∞. All this is consistent with (5) if and only if

$$\left[v^2 v_T^2 \frac{dg}{dv} + v^3 g \right]_{v=0} = 0. \tag{8}$$

Now, unless $f_{nm}(v)$ is singular at v = 0, the solution to Eq. 4 is either analytic at the origin or has a simple pole there. But a simple pole at the origin violates condition (8), so we conclude that

$$g(v \to 0) = \text{const.} \tag{9}$$

It turns out that Eqs. 4, 6, and 7 yield a unique solution for any pair of values of (v_T, v_D); condition (9) is but an additional check on the correctness of the integration procedure.

Method of Numerical Integration

For a given set of values (v_T, v_D, k, θ), we may integrate (4) numerically, first rewriting it as follows:

$$\frac{d^2g}{dv^2} + \frac{1}{v_T^2}\left(\frac{2v_T^2}{v} + v\right)\frac{dg}{dv} + \frac{1}{v_T^2}\left(3 - \frac{v^2}{v_D^2} - h_\mu^{x+i} - \theta\right) g = -\frac{k}{v_T^2} f_{nm}(v)$$

or

$$g'' + A(v)\, g' + B(v)\, g = C(v).$$

We divide v-space into discrete intervals $\Delta v = h$, and label these intervals with an index n:

$$g_n'' + A_n g_n' + B_n g_n = C_n.$$

We combine this equation with two integrations by the trapezoidal rule

$$g_n' = g_{n-1}' + \frac{h}{2}(g_n'' + g_{n-1}'')$$

$$g_n = g_{n-1} + \frac{h}{2}(g_n' + g_{n-1}')$$

and solve these three, step by step, as simultaneous equations in g_n, g_n', and g_n''.

The values of k and θ are obtained by iteration. Values of these two parameters are guessed initially, but with each integration of g, new values of k and θ are computed from (6) and (7). Thus far, this iteration has in every case converged; moreover, the final form of g always satisfies condition (9).

Preliminary Results

The computer program turns out values for θ, k, $\langle h_\mu^x + h_\mu^i \rangle$, $\langle h_\mu^i \rangle$, and $\langle v^2 \rangle$, as well as values of the distribution function and its derivatives at selected intervals.

Variations of interval size, of the maximum velocity serving as cutoff for the integration (in lieu of infinity), and of the normalization function $f_{nm}(v)$, indicate that the parameters obtained are accurate within 1%.

The variation of $\theta = \langle h_\mu^i \rangle$ with v_T for infinite v_D is shown in Fig. X-15, as is $\langle h_\mu^x + h_\mu^i \rangle$. The corresponding variation of $\langle v^2 \rangle$ is shown in Fig. X-16.

Figure X-17 shows the variation of $\langle h_\mu^i \rangle$, k, and $\langle h_\mu^i \rangle - \theta = \langle v^2 \rangle / v_D^2$ with v_D for four values of v_T. The point at which $\langle h_\mu^i \rangle$ and $\langle v^2 \rangle / v_D^2$ are equal is the value of v_D for which

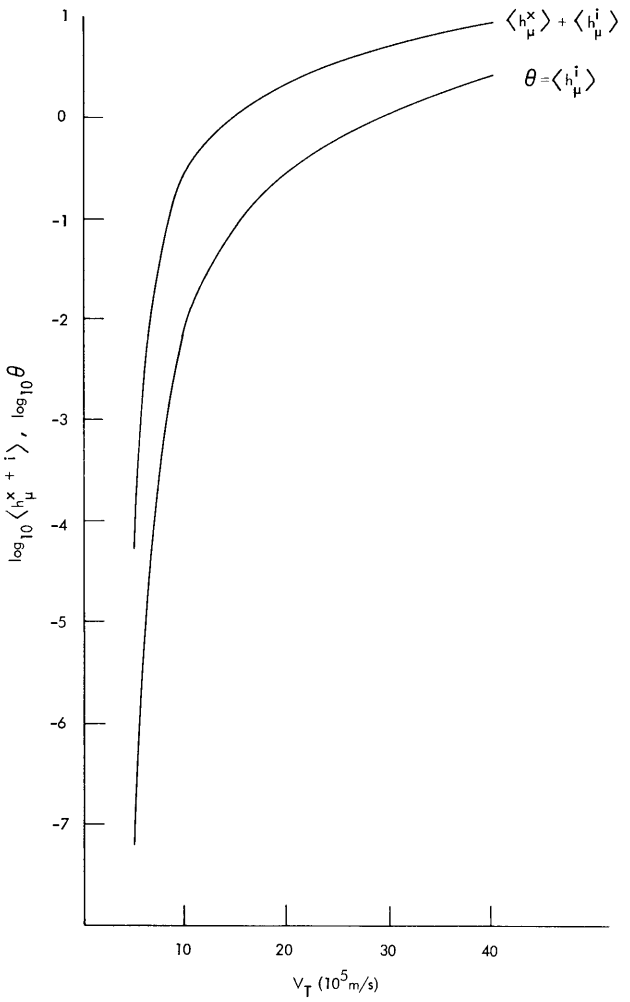

Fig. X-15.

Total rate of inelastic collisions and rate of ionization collisions, normalized by $\mu\nu_m$, as functions of v_T.

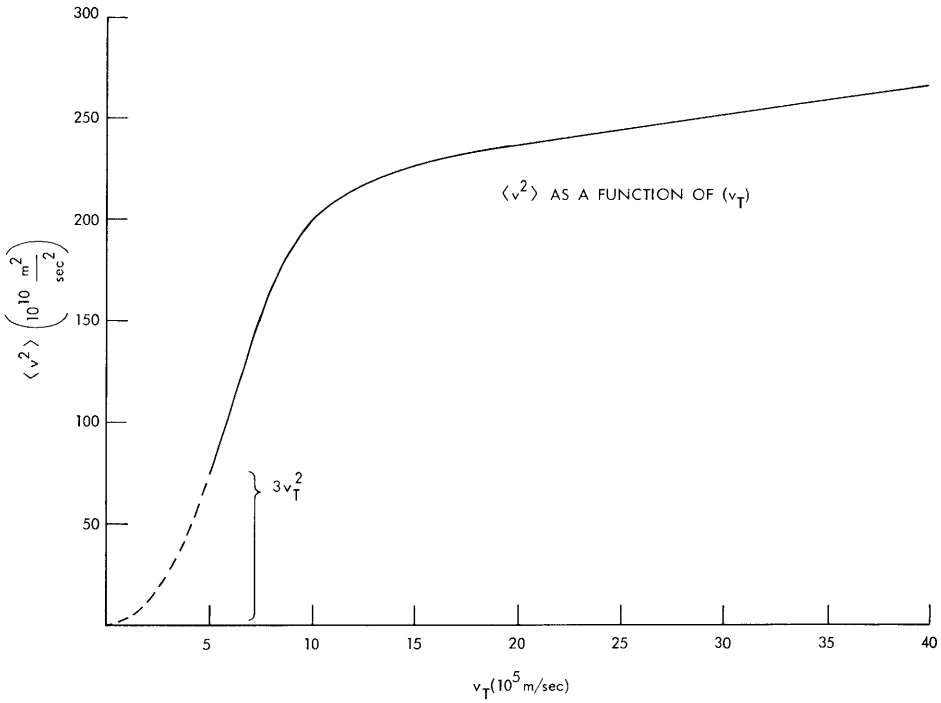

Fig. X-16.

Mean-square velocity as a function of v_T.

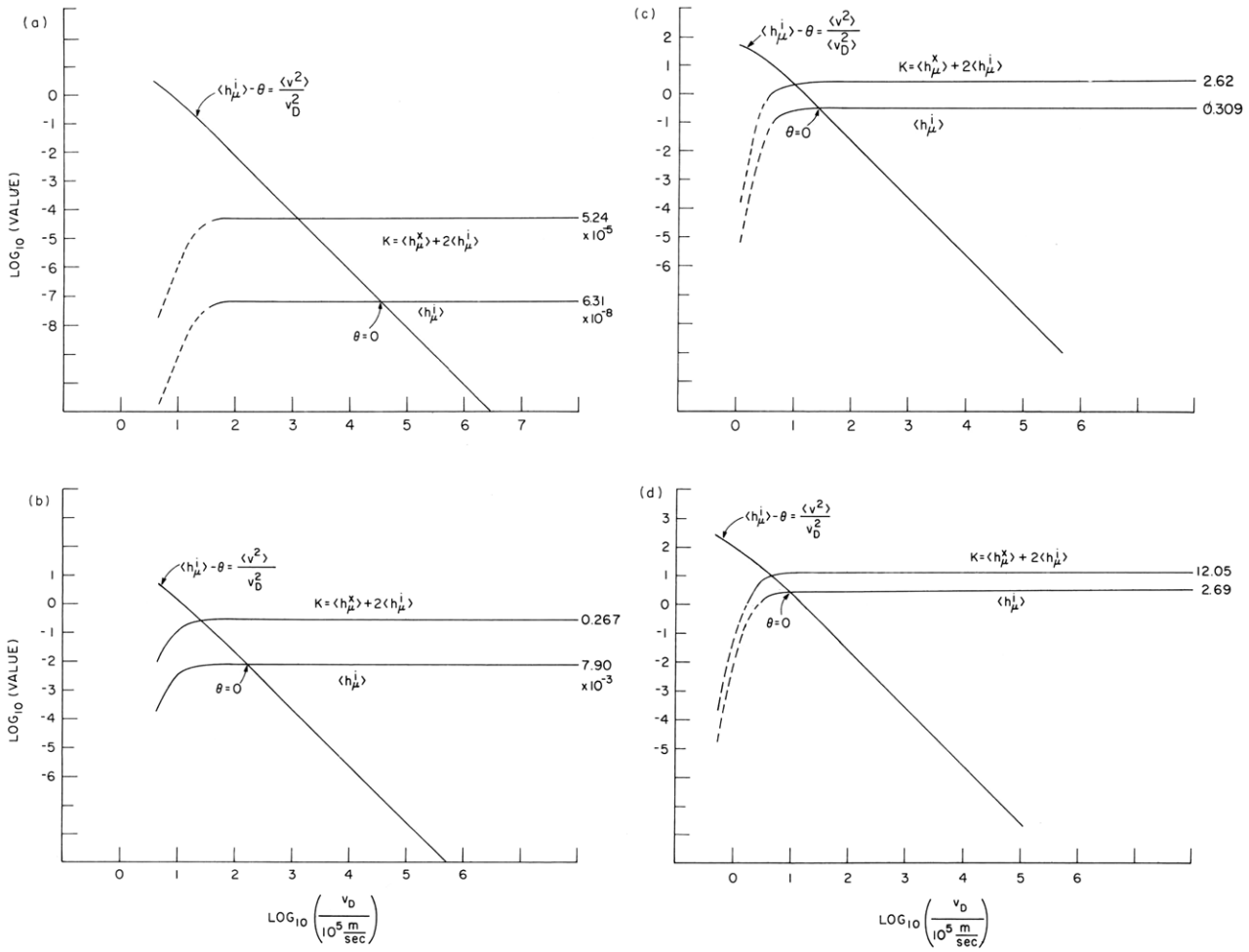

Fig. X-17. Variation of characteristic rates with v_D, for typical values of v_T.

(a) $v_T = 5 \times 10^5$ m/sec.

(b) $v_T = 10 \times 10^5$ m/sec.

(c) $v_T = 20 \times 10^5$ m/sec.

(d) $v_T = 40 \times 10^5$ m/sec.

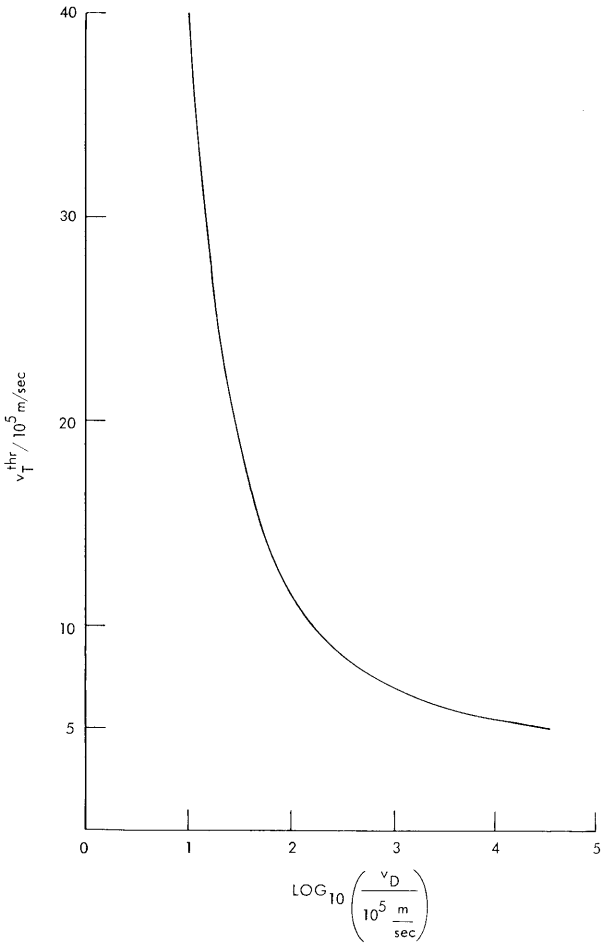

Fig. X-18. Basic threshold curve.

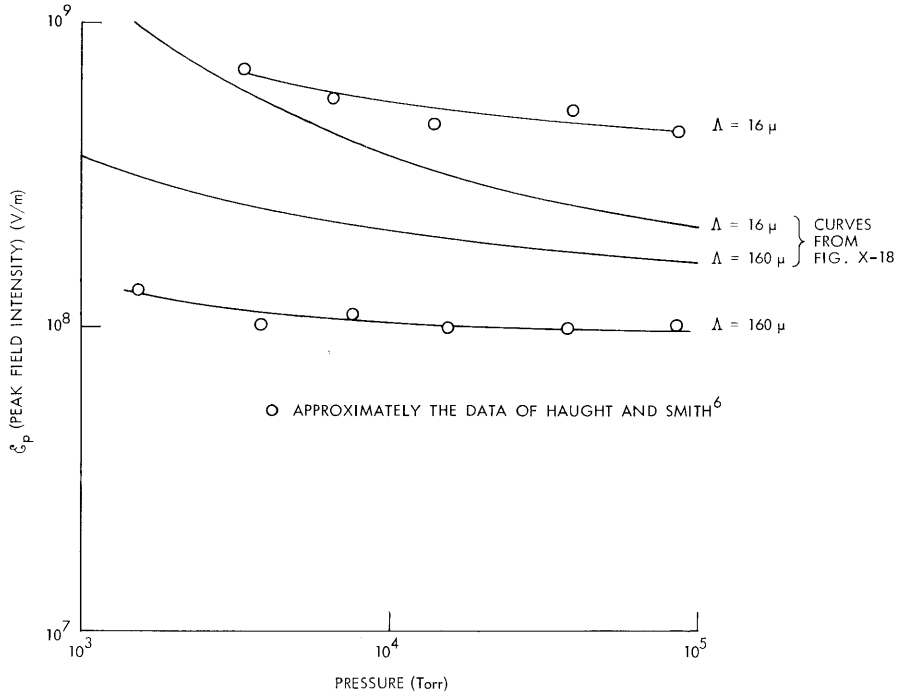

Fig. X-19. Comparison with experiment. The central curves are projected from Fig. X-18.

$\theta(v_T, v_D)$ changes sign, and is so marked. It will be noted in Fig. X-17 that the point $\theta = 0$ may be fairly closely determined by the intersection of straight lines extrapolated from $v_D \to \infty$; that is, the values given in Figs. X-15 and X-16 may be used to estimate

$$v_T^{thr}(v_D),$$

where v_T^{thr} is that value of v_T for which θ changes sign. Such a plot is shown in Fig. X-18.

Figure X-19 shows the curves of Fig. X-18 reduced to the $\mathscr{E}$-P plane, for two values of Λ, together with some experimental data of Haught and Smith.[6] Note that the order of magnitude of our calculation from first principles is correct, but displaying the curves of Fig. X-18 in the $\mathscr{E}$-P plane does not predict a strong enough dependence of the threshold on Λ. We do not know at this time whether this discrepancy is due to (a) our failure, thus far, to integrate over the pulse duration; (b) our use of the approximations (2), which have not yet been sufficiently justified; (c) our failure to include some other important effect such as trapping of the resonance line emission; or (d) the failure of the classical treatment of the incident electric field.

J. H. Vellenga

References

1. M. Young and M. Hercher, J. Appl. Phys. 38, 4393 (1967).
2. W. P. Allis, Handbuch der Physik, edited by S. Flügge (Springer-Verlag, Berlin, 1956), Vol. 21, pp. 383-444; also Technical Report 299, Research Laboratory of Electronics, M.I.T., June 13, 1956.
3. A. D. MacDonald, Microwave Breakdown in Gases (John Wiley and Sons, Inc., New York, 1966).
4. H. Maier-Leibnitz, Z. Physik 95, 499 (1935); R. M. St. John, F. L. Miller, and C.C. Lin, Phys. Rev. 134, A888 (1964); J. D. Jobe and R. M. St. John, Phys. Rev. 164, 117 (1967); D. Rapp and P. Englander-Gordon, J. Chem. Phys. 43, 1464 (1965); see also B. L. Moiseiwitch and S. J. Smith, Rev. Mod. Phys. 40, 238 (1968).
5. H. R. Griem, Plasma Spectroscopy (McGraw-Hill Publishing Co., New York, 1964).
6. A. F. Haught and D. C. Smith, Report UACRL E920272-8, United Aircraft Research Laboratories, August 1966 (unpublished).

7. DETERMINATION OF THE ENERGY DISTRIBUTION OF THE HOT-ELECTRON COMPONENT IN A PULSED ELECTRON-CYCLOTRON RESONANCE DISCHARGE

We have continued the study of the high-frequency instability that is present in the hot-electron plasma of our mirror-confined electron-cyclotron resonance discharge. Previous reports[1,2] have disclosed that several hundred microseconds pass following the end of the heating pulse before an intense burst of instability radiation is emitted by the plasma. Under the assumption that this time is that required for the velocity distribution of the hot-electron component to evolve into an unstable form, it follows that the energy distribution of these electrons may reflect these changes. We have thus undertaken a detailed study of the electron-energy distribution in the range 10-100 keV through measurement and interpretation of the plasma Bremsstrahlung spectra. This report presents the findings of the study.

It is well known that the relationship between the emission of x rays arising from the scattering of energetic electrons by neutral hydrogen and the energy distribution of these electrons is given by[3]

$$\eta(E) = \frac{16}{3} \frac{r_o^2 \alpha c^2}{E} N \int_E^\infty \frac{n(u)}{u} \ln\left(\frac{m a_o u}{h}\right) du, \tag{1}$$

where $\eta(E)$ is the number of x-ray photons per second per unit energy per unit volume emitted by the process at an energy E, N is the neutral gas density, n(E) is electron energy distribution (number per unit energy per unit volume), with u being the electron velocity, r_o the classical radius of an electron, α the fine-structure constant, c the velocity of light, a_o the first Bohr radius, m the electron mass, and h Planck's constant. It then follows from (1) that

$$n(E) = -\frac{2.2 \times 10^{14}}{N} E^{1/2} \frac{d}{dE}[E\,\eta(E)] \tag{2}$$

when the energy is in keV, the unit volume is taken as a cubic centimeter, and the slowly varying logarithm in (1) has been assumed constant with its argument evaluated at a velocity equal to the speed of light.

Measurement of $\eta(E)$ was accomplished by means of the system of Fig. X-20 in conjunction with a 400-channel RIDL pulse-height analyzer. The collimation system consists chiefly of two copper plates, 1/2 inch thick, separated by 75 cm with each having a viewing hole, 1/4 inch in diameter. A region, approximately 1 cm in diameter, is viewed by this system at the axis of the cavity. The vacuum extension between the collimators provides a path of minimum absorption for low-energy x-ray photons, and is

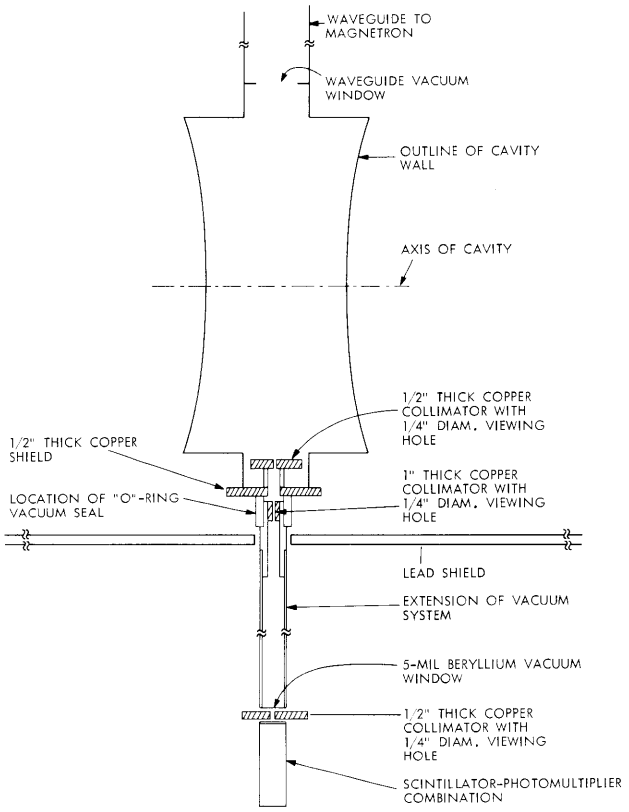

Fig. X-20. Detail of the collimation and detection system for the measurement of the plasma Bremsstrahlung spectrum.

sealed by a beryllium window, 5 mil thick. By viewing the plasma perpendicular to the cavity axis at the midplane, the collimation system is able to avoid detection of wall-generated x-rays, since it "looks" down the waveguide that is located on the opposite side of the cavity.

Detection of the x-ray photons was accomplished with an NaI(Tl) scintillation crystal, 2 mm thick, having a beryllium window, 5 mil thick, and a Model 10-8 RIDL scintillation probe to detect the scintillations. The 5-mil beryllium window on the crystal and the 5-mil beryllium vacuum window have very low attenuation for photon energies greater than 10 keV. (At 5 keV the correction for absorption in the windows is only ~1.4, thereby permitting qualitative observations below 10 keV.) The upper energy limit with this thin crystal is determined by the energy at which a photon can pass through the crystal. This energy was found experimentally to be ~140 keV. Analysis of the phototube output was accomplished with a 400-channel RIDL pulse-height analyzer. Calibration of the overall detection system was achieved in the range 0-100 keV by observing the x-ray peaks of C_o^{57}, C_s^{137} and A_m^{241} (14, 32, and 59.7 keV, respectively) and adjusting the analyzer amplifiers to place the peaks in the proper channels.

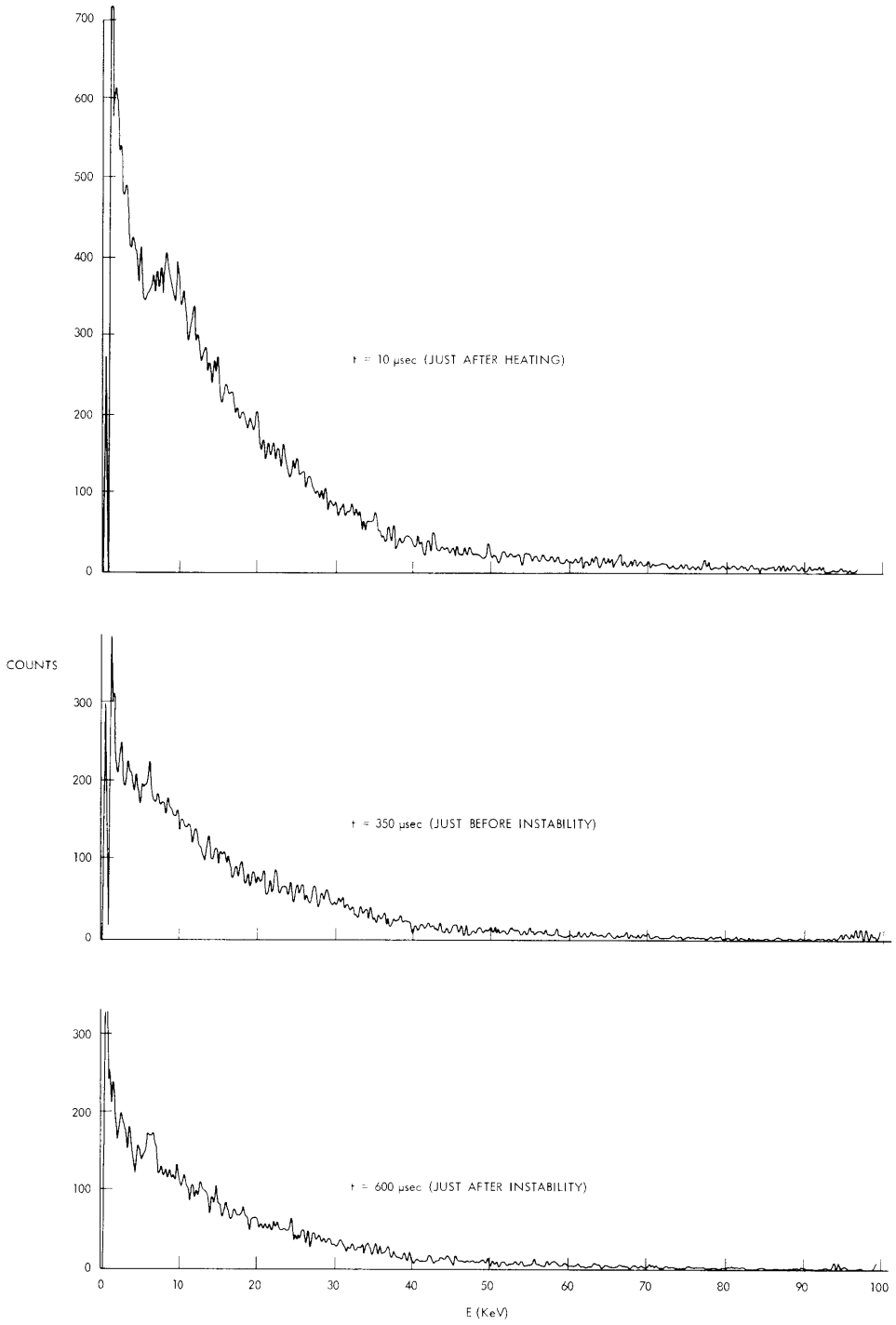

Fig. X-21. Measured photon number count vs energy at three critical times in the afterglow. Actual counting time, 24 sec. Discharge parameters: 3×10^{-5} Torr H_2; magnet current, 75 A; incident peak microwave power, 26 kW at 2852 MHz.

In operation the analyzer was gated on for a 20-μsec period at a given delay time following the end of each microwave heating pulse (1000/sec). In this way, the characteristics of the x-ray emission were determined as a function of time throughout the afterglow of the plasma. Figure X-21 shows this number count at three critical times in the afterglow for a total counting time of 20 min. The measured number count $\eta_c(E)$ is related to $\eta(E)$ by

$$\eta(E) = \frac{\eta_c(E)}{T_c \times V_g \times \Delta E \times P_o}, \tag{3}$$

where T_c is the actual time that the analyzer is gated on, V_g is the volume of plasma viewed by the detector, ΔE is the energy width of each channel of the analyzer, and P_o is the probability that an x-ray photon generated in the plasma will pass into the collimator. Under the assumption that the x rays are radiated isotropically, this latter quantity is simply the solid angle subtended by the collimator as viewed from the plasma divided by 4π. For our conditions this becomes $\eta(E) = 6.24 \times 10^3\ \eta_c(E)$ (photons keV^{-1} cc^{-1} sec^{-1}). Combining this result with (2) yields

$$n(E) \approx -1.3 \times 10^6\ E^{1/2} \frac{d}{dE} E[\eta_c(E)] \quad \frac{\text{electrons}}{\text{cm}^2\text{-keV}} \tag{4}$$

when n corresponds to that at a hydrogen pressure of 3×10^{-5} Torr.

Figure X-22 shows the relative unfolded energy distribution functions at the three

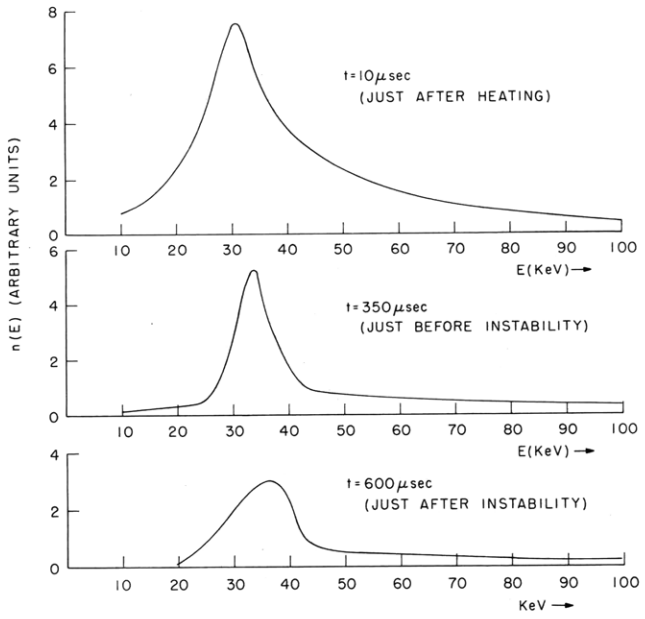

Fig. X-22. Relative electron energy distribution functions determined from the measurements of Fig. X-21.

times of Fig. X-21. The data were not unfolded for energies below 10 keV, because of the exponentially increasing correction resulting from absorption in the beryllium windows and an insufficient accuracy in the measurement of the energy. In obtaining these curves the data of Fig. X-21 were corrected for absorption at 10 keV (correction factor = 1.048) and also corrected for the slight nonlinear pulse height vs photon energy characteristic of the NaI(Tl) crystal. In performing the latter correction, the data of Aitken and co-workers, determined for a similar crystal, were employed.[4] Absolute measurements of the density as predicted by (4) are found to be approximately two orders of magnitude too high when compared with independent measurements of the total electron density. This is attributed to the relatively high percentage of large Z impurity atoms present in the background gas at a pressure of 3×10^{-5} Torr (base pressure = 2×10^{-7} Torr), since it is known that the x-ray intensity goes as Z^2 of the scattering atom.

It is clear from Fig. X-22 that the energy distribution of the electrons is peaked around 30 keV immediately following the heating pulse. Up to the time of the instability there is also a continuous decrease in the total density of electrons with energies between 10 keV and 100 keV. From curves similar to those of Fig. X-22 it is observed that this density decreases with a time constant of ~440 μsec. This is to be compared with the ~30-msec decay time expected from electron-neutral small-angle scattering calculations for a 30-keV electron. As well as this rapid loss of plasma, we observe that the distribution becomes more highly peaked, with a large fraction of the lower energy electrons being lost. The instability results in a loss of approximately one-half of the electron density in the 10-100 keV range, and also appears to result in a spreading of the distribution. Following the instability, the distribution changes only slowly with time. The hot-electron density-decay rate late in the afterglow is then ~32 msec, which is consistent with previously reported total density-decay rates.[5] It also is consistent with loss times attributable to small-angle scattering of the 30-40 keV electrons into the mirror loss cone.

Finally, the relative energy density vs time determined from these and similar electron energy distributions at other times in the afterglow is shown in Fig. X-23. Note that the energy density decays with a time constant of ~450 μsec up to the time of the instability. This decay rate is an order of magnitude slower than that observed from the plasma diamagnetism. This more rapid drop in the diamagnetism is believed to be associated with the rapid loss of electrons with energies in the range ~1-5 keV. That such a loss occurs can be inferred qualitatively from $\eta_c(E)$ at various times in the afterglow by realizing that Eq. 1 states that the only way the number count at low energies can decrease relative to that at higher energies is if the low-energy electron density has decreased. This loss has also been observed directly in thick target Bremsstrahlung from a beryllium target placed on the cavity wall at the mirror peak.

These observations indicate that before the occurrence of the high-frequency

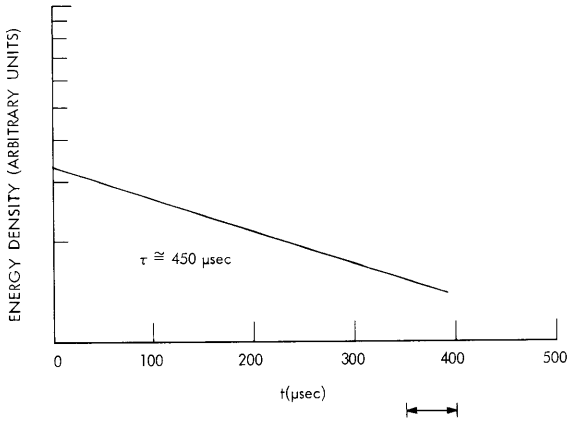

Fig. X-23. Decay of the energy density as determined from the plasma Bremsstrahlung measurements. The arrows indicate the range of the most probable time for the occurrence of the instability.

instability the hot-electron distribution is becoming highly peaked in energy in the range 30-35 keV. This indicates that a nonequilibrium condition may exist but is not conclusive, since an instability theory requires the more detailed information contained in a velocity distribution. We are continuing the interpretation of these results in light of previous measurements in order to see if a consistent velocity distribution may be inferred.

C. E. Speck

References

1. C. E. Speck, "Experimental Study of Enhanced Cyclotron Radiation from an Electron-Cyclotron Resonance Discharge," Quarterly Progress Report No. 89, Research Laboratory of Electronics, M. I. T., April 15, 1968, pp. 177-182.
2. C. E. Speck and A. Bers, "Experimental Study of Enhanced Cyclotron Radiation from an Electron-Cyclotron Resonance Discharge," Quarterly Progress Report No. 90, Research Laboratory of Electronics, M. I. T., July 15, 1968, pp. 135-144.
3. T. J. Fessenden, "Pulsed Electron-Cyclotron Resonance Discharge Experiment," Technical Report No. 442, Research Laboratory of Electronics, M. I. T., Cambridge, Mass., March 15, 1966, pp. 70-72.
4. D. W. Aitken, B. L. Beron, G. Yenicay, and H. R. Zulliger, "The Fluorescent Response of NaI(Tl), $C_sI(Tl)$, $C_sI(N_a)$ and $C_aF_2(E_u)$ to X-rays and Low Energy Gamma Rays," IEEE Trans., Vol. NS-14, No. 1, pp. 468-477, February 1967.
5. C. E. Speck and A. Bers, op. cit., p. 143.

8. INSTABILITIES DRIVEN BY HOT ELECTRONS IN A MAGNETIC MIRROR

We have continued our investigation of the possibility of negative dissipation effects in a mirror-confined electron distribution in the presence of a high-frequency electric field. Our previously reported calculations[1] were based on the approximation that the electrons did not penetrate too deeply into the magnetic mirror. In this report we present additional calculations that remove this approximation.

Subject to the experimental observations discussed in our previous report, we choose to calculate the power absorbed (or emitted) by a distribution of electrons confined by a mirror magnetic field with parabolic axial dependence, $B(z, r = 0) = B_o(1+z^2/L^2)$, when they are acted upon by an RF electric field. We take the RF field to have an $e^{j\omega t}$ dependence ($\omega = \omega + j\omega_i$, $\omega_i \ll \omega_r$) and to be circularly polarized transverse to the magnetic field. No variation of the electric field along z is assumed, and it is taken to be of infinite wavelength.[2] (In our previous report we took the field to be linearly polarized, but have found that in the decomposition of this field into two oppositely rotating circularly polarized fields only the component rotating with the electrons entered into the interaction.) Taking the midplane ($Z = 0$) electron distribution in the absence of the electric field to be of the form

$$f_o = n_o F_\perp\left(v_{\perp o}^2\right) F_{11}\left(v_{11o}^2\right), \tag{1}$$

where n_o is the electron density, we integrate the linearized Vlasov equation along the zero-order electron orbits predicted by adiabatic theory

$$z(t') = z_o \cos\left[\omega_m(t'-t)+\phi\right] \tag{2}$$

$$\begin{aligned} v_\perp(t') &= v_{\perp o}\, e^{j\Psi}\sqrt{1 + z^2/L^2}\; e^{j\int_t^{t'} \omega_c(t'')\, dt'} \\ &= v_x(t) + jv_y(t), \end{aligned} \tag{3}$$

where $z_o = Lv_{110}/v_{\perp o}$ is the maximum penetration depth into the mirror of an electron whose midplane parallel and perpendicular velocity magnitudes are v_{110} and $v_{\perp o}$, respectively, $\omega_m = v_{\perp o}/L$ is the mirror frequency of the electron, $\omega_c(t) = \omega_{co}(1+z^2(t)/L^2)$ is the instantaneous cyclotron frequency of the electron, ϕ is the phase of the electron in its longitudinal motion at $t' = t$ and Ψ is the phase of the transverse velocity at $t' = t$. This integration yields the first-order distribution function for the electrons, $f_1(z, v_{110}, v_{\perp o}, t)$, which is then used to calculate the first-order current density in the plasma. The time average power absorbed per unit transverse area by the electrons can then be determined from the expression

$$P_d = \mathrm{Re} \int \left(E_l^* J_\perp\right) dz, \tag{4}$$

where both E_l and $J_\perp$ are written in circular polarized variables. The results of the calculation are

$$P_d = \mathrm{Re}\left(-|E_l|^2 \epsilon_o \omega_{po}^2 \pi^2\right) \int d(v_{\perp o})^2 \int d\left(z_o^2\right) \int \frac{d\phi}{2\pi}\, \omega_m b^{3/2}(\tilde{z})\, v_{\perp o}^2$$

$$\int_{-\infty}^{0} d\tau\, e^{j\omega\tau} \left[\left(F_\perp' F_{ll} - F_\perp F_{ll}'\right) \frac{1}{b(z')} + F_\perp F_{ll}'\right] b^{1/2}(z')$$

$$\exp\left\{-j\left[\bar{\omega}_c \tau + A \sin 2(\omega_m \tau + \phi) - A \sin 2\phi\right]\right\}, \tag{5}$$

where

$$b(z) = 1 + z^2/L^2$$

$$\tilde{z} = z_o \cos\phi$$

$$\tau = t' - t$$

$$z' = z(\tau)$$

$$\bar{\omega}_c = \omega_{co}\left(1 + z_o^2/2L^2\right)$$

$$A = \omega_{co} z_o^2/\left(4\omega_m L^2\right)$$

$$\omega_{po}^2 = e^2 n_o/(\epsilon_o m)$$

and the primes on the distribution functions indicate derivatives with respect to their arguments. In order to perform the integrations on τ and ϕ, we introduce the real functions $M_n^k\left(A, z_o^2/L^2\right)$ defined by

$$\left[1 + \frac{z_o^2}{L^2} \cos^2\left(\frac{\theta}{2}\right)\right]^k e^{-jA\sin\theta} = \sum_{n=-\infty}^{\infty} M_n^k\, e^{-jn\theta}, \tag{6}$$

which satisfy the relation

$$M_n^k = \frac{1}{2\pi} \int_0^{2\pi} d\theta\, e^{jn\theta - jA\sin\theta} \left[1 + \frac{z_o^2}{L^2} \cos^2\left(\frac{\theta}{2}\right)\right]^k. \tag{7}$$

These integrations may then be performed to yield

$$P_d = -\left(|E_1|^2 \epsilon_o \omega_{po}^2 \pi^2\right) \mathrm{Re} \int d\left(v_{\perp o}^2\right) \int d\left(z_o^2\right) \frac{v_{\perp o}^3}{L}$$

$$\sum_{n=-\infty}^{\infty} M_n^{3/2} \left[(F_\perp' F_{11} - F_\perp F_{11}') M_n^{-1/2} + F_\perp F_{11}' M_n^{1/2} \right] \frac{1}{j(\omega - \bar{\omega}_c - 2n\omega_m)}. \tag{8}$$

Thus it is clear that the "resonant" electrons are those whose average cyclotron frequency plus or minus even multiples of its mirror frequency equals the frequency of the RF field. In the limit of vanishing small negative imaginary part of ω the integration on z_o^2 is then performed to yield

$$P_d = 2\pi^3 \frac{\omega_{po}^2}{\omega_{co}^2} \epsilon_o L |E_1|^2 \int_0^\infty d\eta \, F_\perp(\eta) \sum_{n=-\infty}^{\infty} Q_n(\eta), \tag{9}$$

where

$$Q_n(\eta) \equiv -\eta^{3/2} M_n^{3/2} \left\{ M_n^{1/2} - M_n^{-1/2} \left[y_n + \eta \frac{dy_n}{d\eta} + 1 \right] \right\} F_{11}'(\eta y_n) \mu_{-1}(y_n)$$

$$+ \eta^{3/2} \left\{ \frac{3}{2} \frac{1}{\eta} M_n^{3/2} M_n^{-1/2} + \frac{d}{d\eta} \left(M_n^{3/2} M_n^{-1/2} \right) \right\} F_{11}(\eta y_n) \mu_{-1}(y_n), \tag{10}$$

with

$$y_n = \frac{2}{\omega_{co}} \left(\omega - \omega_{co} - \frac{2n\eta^{1/2}}{L} \right)$$

$$M_n^k = M_n^k \left(A = \frac{\omega_{co} L}{4\eta^{1/2}} y_n, \frac{z_o^2}{L^2} = y_n \right)$$

$$\eta = v_{\perp o}^2.$$

Of particular interest in the application of this theory to the explanation of the high-frequency instability present in our pulsed electron-cyclotron resonance discharge[2] is the nature of the power absorption at a frequency equal to the minimum cyclotron frequency along a field line. From Eq. 9, the sign of P_d for a sufficiently narrow perpendicular distribution about a particular η is determined by the sign of the sum of the Q_n

evaluated at η. Noting that for $\omega = \omega_{co}$ none of the positive n values contribute and because the parallel distribution should decrease at large arguments, we expect that only the n = 0 and first few negative terms in the sum are necessary for the determination of P_d. Note also that to first order in y_n the $M_n^k(A, y_n)$ functions defined by (7) are approximated by $J_n(A_n)$. We then find for $\omega = \omega_{co}$ that the n = 0 term is given by

$$Q_o = \frac{3}{2}\,\eta^{1/2} F_{11}(0), \tag{11}$$

and for the n = -1 term

$$Q_{-1} = \frac{6\eta^2}{L\omega_{co}} J_1^2(1)\, F_{11}'\left(\frac{4\eta^{3/2}}{L\omega_{co}}\right) + \frac{3}{2}\,\eta^{1/2} J_1^2(1)\, F_{11}\left(\frac{4\eta^{3/2}}{L\omega_{co}}\right). \tag{12}$$

From (11), which in fact is exact, we see that the n = 0 term always predicts positive dissipation at $\omega = \omega_{co}$. It vanishes only if $F_{11}(0)$ vanishes. By combining (11) and (12), an approximate criterion for negative dissipation at $\omega = \omega_{co}$ may be derived to yield

$$\frac{-4\eta^{3/2}}{L\omega_{co}} \frac{F_{11}'\left(\frac{4\eta^{3/2}}{L\omega_{co}}\right)}{F_{11}\left(\frac{4\eta^{3/2}}{L\omega_{co}}\right)} > 1 + \frac{F_{11}(0)}{J_1^2(1)\, F_{11}\left(\frac{4\eta^{3/2}}{L\omega_{co}}\right)}. \tag{13}$$

It can be shown that a Maxwellian parallel distribution cannot satisfy this criterion and, therefore, must result in positive dissipation at ω_{co}. In fact, numerical calculations of the entire sum in (10) showed strong positive dissipation for ω at and above ω_{co}, and very small negative dissipation in frequency bands below ω_{co}, when a Maxwellian F_{11} was used.

The class of distribution functions that most easily satisfy (13) are those with $F_{11}(0) = 0$. Thus we are led to consider peaked distributions of the form

$$F_{11}\left(v_{110}^2\right) = \frac{n}{v_{11T}\Gamma(1+1/2n)} \left(\frac{v_{110}^2}{v_{11T}^2}\right)^n \exp -\left(\frac{v_{110}^2}{v_{11T}^2}\right)^n \tag{14}$$

which are observed to approach a delta function at $v_{11}^2 = v_{11T}^2$ as $n \to \infty$. A detailed numerical study of Eq. 9 was undertaken, using the n = 4 member of the class of distribution functions described by Eq. 14. The M_n^k functions were evaluated by expanding them in terms of an infinite sum of Bessel functions. Figure X-24 shows a characteristic

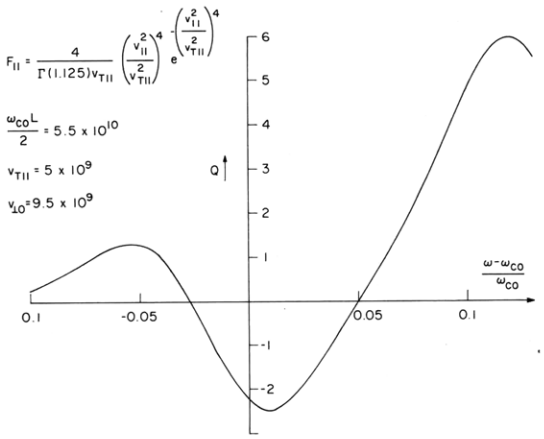

Fig. X-24.

Plot of the gain parameter $Q \equiv \Sigma Q_n$ of Eqs. 9 and 10 for the stated parameters.

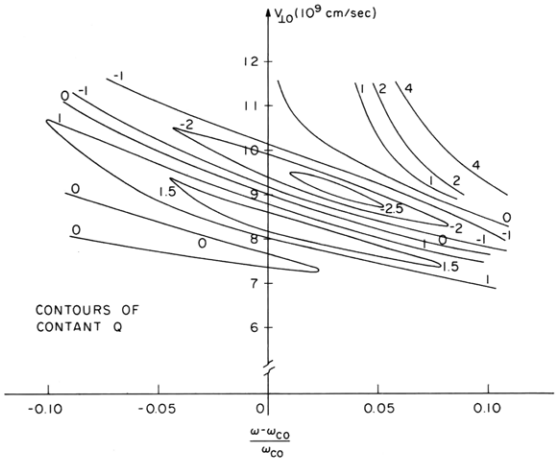

Fig. X-25.

Contours of constant Q for the parallel distribution of Fig. X-24.

plot of $Q \equiv \sum_{n=-\infty}^{\infty} Q_n$ against $(\omega-\omega_{co})/\omega_{co}$ for $v_{T11} = 5 \times 10^9$ cm/sec, $v_{\perp o} = 9.5 \times 10^9$ cm/sec, $\omega_{co} = 2\pi \times 2.5 \times 10^9$ sec^{-1}, and $L \cong 7$ cm which are characteristic of the parameters in our experiment. Note that a wide region of negative absorption occurs in the vicinity of $\omega = \omega_{co}$. Several such curves for different $v_{\perp o}$ have been used to construct the plot of constant Q contours in $v_{\perp o} - (\omega-\omega_{co})/\omega_{co}$ space shown in Fig. X-25. A region of negative absorption is observed for large values of $v_{\perp o}$ and $\omega \sim \omega_{co}$. We thus arrive numerically at the conclusion that for the relatively peaked parallel distribution under consideration, the perpendicular velocity must also be peaked in order to achieve net negative dissipation (that is, Eq. 9 states that $Q\left(v_{\perp o}^2\right)$ is weighted by $F_{\perp}\left(v_{\perp o}^2\right)$ in determining the net dissipation).

These calculations illustrate that net dissipation is possible for suitable distribution functions. We are continuing the study of this theory with particular interest in its application to the experiment.

C. E. Speck, R. J. Briggs

References

1. C. E. Speck and R. J. Briggs, "Instabilities Driven by Hot Electrons in a Magnetic Mirror," Quarterly Progress Report No. 93, Research Laboratory of Electronics, M.I.T., April 15, 1969, pp. 101-110.
2. The results presented here can easily be generalized to include an arbitrary standing-wave field, $E_1 f(z)\, e^{i\omega t}$. The only change is that in the expression for M^k the left-hand side of Eq. 6 will now be multiplied by $f(z_o \cos\theta^n/2)$.
3. C. E. Speck, "Experimental Study of Enhanced Cyclotron Radiation from an Electron-Cyclotron Resonance Discharge," Quarterly Progress Report No. 89, Research Laboratory of Electronics, M.I.T., April 15, 1968, pp. 177-180.

X. PLASMAS AND CONTROLLED NUCLEAR FUSION*

B. Diffusion and Turbulence

Academic and Research Staff

Prof. T. H. Dupree
Prof. L. M. Lidsky
Prof. W. M. Manheimer

Graduate Students

K. R. S. Chen
H. Ching
S. I. Friedman
H. R. Greenberg
P. M. Margosian
G. K. McCormick
R. L. McCrory, Jr.
M. Murakami
L. C. Pittinger
J. E. Robinson

1. EXPERIMENTS ON WAVE-PARTICLE INTERACTION

The construction of the linear nonadiabatic experimental device, which was intended to provide a sensitive test of nonlinear theories of wave-particle interactions in plasma,[1-4] has been completed. This report describes a performance test in the device and preliminary results of an experiment on the interaction between electrons and waves produced by the electron beam itself.

The experimental configuration, described in detail in a previous report,[1] is shown schematically in Fig. X-26. An electron trap in a uniform magnetic field is produced by two negatively biased trapping electrodes. The pulse system enables us to inject the electrons into the trap and to extract them for energy analysis after some trapping time which is variable from 10^{-7} sec to 5×10^{-4} sec. The interaction of the trapped electrons with the perturbation field located in the trap causes the electron velocity distribution to change from a delta function to some other broader one. The shape of the broadened distribution as a function of the trapping time is the experimental information that we seek. The distribution of $E_{\parallel}$ (energy parallel to the uniform magnetic field) is determined by a retarding potential technique, by using the Faraday cage current modulated by small AC voltage superposed on the DC retarding potential to monitor the energy distribution.

To test the over-all performance of the device, the first experiment was done with no external perturbation field. The experimental data shown in Fig. X-27 indicate time evolution of the distribution function for the 1000-eV electrons injected parallel to the uniform magnetic field of 100 G. The transit time of these electrons between the electrodes is 170 nsec. The data show that the electrons can be trapped without substantial changes of their distribution function for more than 100 μsec (600 transits). The

*This work was supported by the U.S. Atomic Energy Commission (Contract AT(30-1)-3980).

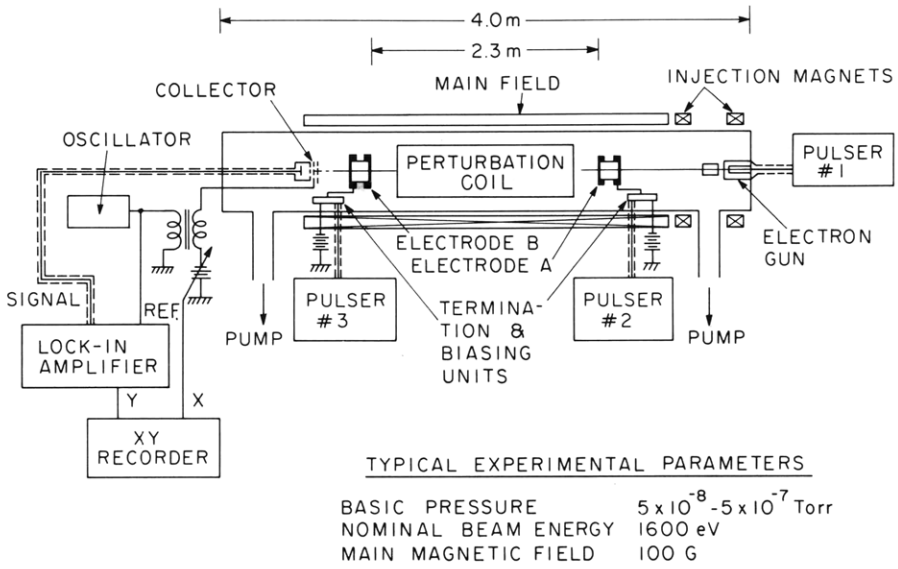

Fig. X-26. Experimental configuration used in the linear nonadiabatic experiment.

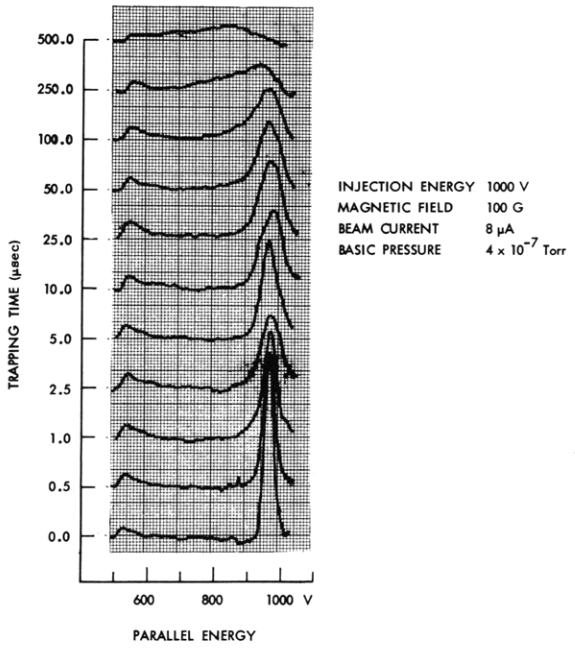

Fig. X-27. Time evolution of the energy distribution function in the weak-beam case.

appreciable broadening at 200 μsec or later results from collisions with background neutrals (the estimated total collision time is 200 μsec at 5×10^{-7} Torr). A bump on each distribution function at 520 V corresponds to the electron population influenced by the transient electric field when they are extracted, hence only the electrons whose parallel energy is above this bump energy can be allowed to impinge on the energy analyzer.

Besides the collisions, the following effects may result in distortion of the distribution function. The first is nonadiabaticity caused by the trapping electrode potentials. The change in magnetic moment[5] is of the order of $(r_L/L)^2$, where r_L is the Larmor radius, and L is the characteristic length of the field – in this case, of the axial electric field of the trapping electrodes. Since this nonadiabaticity limits the confinement time, bigger electrodes have been constructed. The second is instability caused by collective effects, which will be discussed hereafter. In the actual experiments (corkscrew or constant-pitch perturbation), the injected beam has a certain gyration radius; thus the electron density is smaller than that in the present case, and hence the instability is less important.

Figure X-28 shows time evolution of the distribution function for an intense-beam current, which is fifteen times as large as that in Fig. X-27. We can see that two peaks appear in the 2.5-μsec curve, while they merge at 10 μsec. The resultant distribution functions are much broader than those in Fig. X-27. Again the collision effect becomes evident at 250 μsec. Figure X-29 demonstrates evolution of the distribution function on

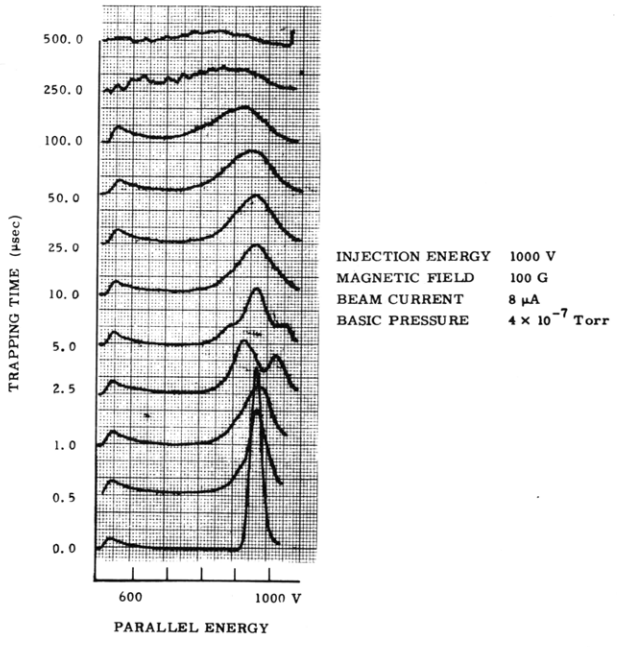

Fig. X-28. Time evolution of the energy distribution function in the intense-beam case.

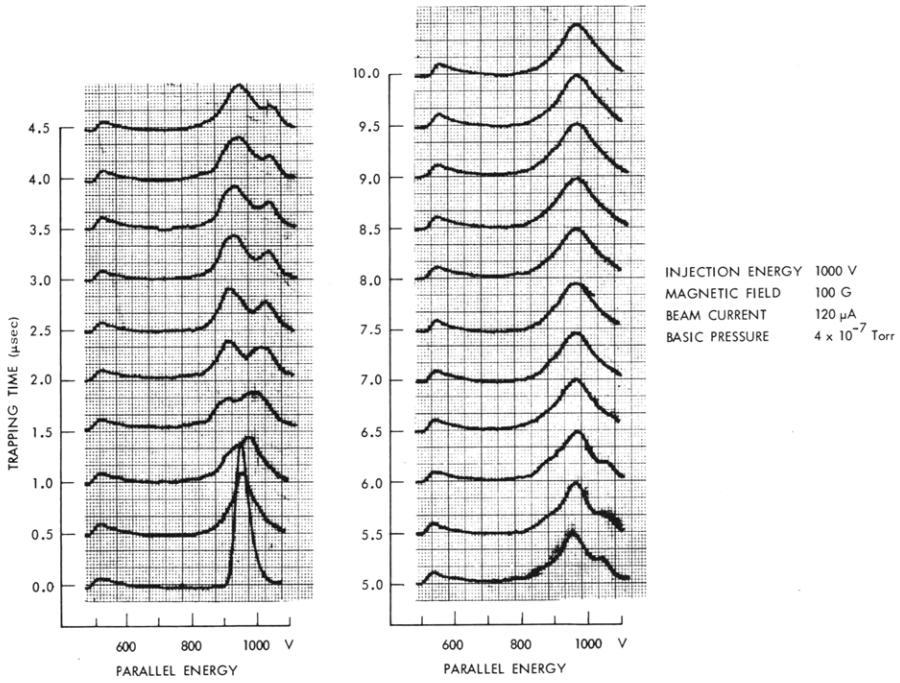

Fig. X-29. Time evolution of the energy distribution function during the first 10 μsec in the same case as in Fig. X-28.

a faster time scale during the first 10 μsec. The distribution function has been broadened at 0.5 μsec, and in the 2.0-μsec curve it splits into two peaks. Thereafter the lower energy peak becomes heavier and heavier, while the higher energy peak is decaying, and finally they merge at ~6.0 μsec. In fact, the total particle energies calculated from the distribution functions are smaller by approximately 1% than the initial particle energy. This fraction of the energy may be counted as the wave energy.

An obvious candidate for the instability is two-stream instability because the reflected portion of the electron beam faces the incoming portion. According to the threshold condition of the two-stream instability, the present beam with an estimated beam radius of 1.5 mm has a minimum unstable wavelength of 60 cm, which corresponds to one-quarter of the trapping length. Therefore this instability presumably exists. Since the phase velocity of this instability is nearly equal to zero, we cannot expect such strong resonant wave-particle interactions as those appearing in Fig. X-29.

The other possibility is an instability caused by coupling between (longitudinal) plasma waves and (transverse) backward cyclotron waves.[6] The frequency is approximately one-half the cyclotron frequency for the case of equal and opposite streaming velocity beams. A relevant feature is that the phase velocity is very close to the streaming velocity; thus resonant wave-particle interaction, if the unstable wave exists, can be expected.

We observed the collector current signals. The oscillation on the signals has characteristically a frequency of ~50 MHz, which is almost independent of the magnetic field. The oscillation lasts a long time, and finally it ceases rather suddenly (for example, at 30 μsec in the 100-G field). The cessation time is approximately proportional to the magnetic field. Therefore the signal may be an indication of bunching of the charges, because of the two-stream instability, and the dependence of the cessation may be explained by the focusing effect of the magnetic field to keep it dense enough to satisfy the instability condition.

The oscillation of the wave electric field was observed by fixed electrostatic probes. We can distinguish two modes: one is the high-frequency mode, the other is the low-frequency mode. The low-frequency mode corresponds to the oscillation seen in the collector signal. The high-frequency mode is observed to have a frequency of approximately one-half the cyclotron frequency, as predicted for coupling between the plasma and cyclotron waves. The detailed characteristics, such as spectrum and wavelength, are under investigation.

The next pertinent question is whether the phase velocity of the unstable oscillation is larger or smaller than the stream velocity, with respect to the Landau damping. The frequency and wave-number formulas in the uncoupled-mode approximation by Maxum and Trivelpiece[6] indicate that difference between the phase velocity and the stream velocity is approximately one-thirtieth the stream velocity, or in terms of energy, the unstable wave lies at 1000 ± 60 V for the 1000-V stream (the plus sign is for the fast plasma wave, and the minus sign is for the slow plasma wave, coupled with the backward cyclotron wave). These positions are approximately the positions where the peaks appear on the distribution function. Because of the large-amplitude oscillation, the trapping of the particles in the wave potential trough may be important in the wave-particle interaction process. Further investigation of these points is under way.

M. Murakami, L. M. Lidsky

References

1. M. Murakami and L. M. Lidsky, Quarterly Progress Report No. 88, Research Laboratory of Electronics, M. I. T., January 15, 1968, p. 220.
2. M. Murakami and L. M. Lidsky, Quarterly Progress Report No. 89, Research Laboratory of Electronics, M. I. T., April 15, 1968, p. 183.
3. M. Murakami and L. M. Lidsky, Quarterly Progress Report No. 90, Research Laboratory of Electronics, M. I. T., July 15, 1968, p. 145.
4. T. H. Dupree, Phys. Fluids 9, 1773 (1966).
5. T. G. Northrop, The Adiabatic Motion of Charged Particles (John Wiley and Sons, Inc., New York, 1963).
6. B. J. Maxum and A. W. Trivelpiece, J. Appl. Phys. 36, 481 (1965).

X. PLASMAS AND CONTROLLED NUCLEAR FUSION*

D. Fusion-Related Studies

Academic and Research Staff

Prof. D. J. Rose
Prof. R. J. Briggs

Graduate Students

G. L. Flint, Jr.
Y. Y. Lau
A. E. Wright

1. FEASIBILITY OF PULSED FUSION DEVICES

Ribe has proposed[1] a pulsed fusion device with a 10-cm vacuum wall radius R_c and a maximum B field of 200 kG. The vacuum wall is the magnetic-field-producing coil and withstands the stress thereby produced. The plasma has a temperature of 15 keV and a radius of half the wall radius. The burning time τ_T is three-eighths the field period τ, and a cooling mechanism operates between pulses.

In the present study we investigate the tritium-breeding, hoop-stress, wall-heating, thermal-stress, and cooling requirements in devices of this sort, using coils of copper-zirconium, niobium-zirconium, or TZM. The coils vary in size from 10 cm to 60 cm.

Tritium Breeding

With an infinite blanket of 98% lithium and 2% niobium, the tritium blanket breeding is acceptable for TZM coils 7 cm or less in thickness. The TZM coils breed better than comparable niobium-zirconium coils or copper-zirconium strengthened with TZM backing. Copper-zirconium is inferior to TZM because copper nuclei slow down neutrons that are then absorbed by the molybdenum nuclei before reacting with the lithium. For the 7.00-cm TZM coil there is no significant change in the T/n = 1.35 breeding ratio for variations in the amount of lithium coolant in the coil for cooling channels occupying less than 7.2% of the coil volume. Of the breeding, 90% comes from the $L^6(n, T)\,\alpha$ reaction.

Hoop Stress

The hoop-stress considerations eliminate from consideration any coil made of copper-zirconium alone, since it cannot withstand the envisioned fields with a safety factor of two. Niobium-zirconium is also unsuitable. It has a low-yield stress at the

*This work was supported by the U.S. Atomic Energy Commission (Contract AT(30-1)-3980).

envisioned peak temperatures ≈1400°K. There is no serious problem with TZM coils. A copper-zirconium coil clad with TZM has been designed, but it would not permit tritium breeding.

Wall Heating

The wall heating is the most critical consideration. The heating in the coil comes from 5 sources: Bremsstrahlung, electrical resistance, neutron collisions, gamma-ray absorption, and synchrotron radiation. The synchrotron radiation is only 0.1% that of Bremsstrahlung; so it is neglected. Electrical and gamma heating are peaked toward the inner wall, and the Bremsstrahlung radiation is deposited in a surface layer, 2 mm thick. Good engineering practice is not to permit operating temperatures to exceed half the melting temperature (on an absolute scale). This eliminates copper-zirconium coils (melting point 1353°K) from consideration. The wall heating for 200 kG, and fractional burnup of 0.09 for copper-zirconium is approximately 1400°K; for niobium-zirconium, 2000°K; for TZM, 1700°K. The gamma heating is 26.2 times the direct neutron heating at the wall for the 7-cm TZM coil. Because of this, the field must be reduced to approximately 180 kG. This does not permit reconsideration of copper-zirconium, since the initial coil temperature still prevents its use; nor of niobium-zirconium, since the gamma heating for it is approximately the same as for the TZM coil and the heating is more severe in the niobium-zirconium coil than in the TZM coil.

For the TZM coil, the maximum wall temperature is

$$T = 1.11 \times 10^{-19} B^4 R_c \tau_T^{1/2} + 7.73 \times 10^{-19} B^4 R_c \tau_T + 4.08 \times 10^{-9} B^2 + T_{initial}\ (°K). \quad (1)$$

Here B is the field in gauss, R_c the coil radius in cm, and τ_T the burning time in sec. Since $\tau_T \propto B^2$, it is seen that for large machines (where B^2R = constant from stress consideration) the second term of Eq. 1 (the gamma and neutron contribution) dominates the first term (Bremsstrahlung heating) and the third term (electrical heating). This is observed for the devices of interest (see Fig. X-30), where the wall heating is 1400°K. Of the temperature rise above the ambient value, 79% is due to gamma heating, 8% to electrical heating, 10% to Bremsstrahlung heating, and 3% to direct neutron scattering. The fields and burning times necessary to achieve this wall heating are also given, as are the number of Bohm times τ_T/τ_B needed to achieve enough confinement. The net power out, P_{out}, is given by

$$P_{out} = \frac{1}{4}\left\{\frac{3}{8}\epsilon P_t + 3(\epsilon - 1) P_E\right\}. \quad (2)$$

Here P_T is the thermonuclear power, P_E the electrical power, and ϵ the efficiency of converting to usable power. The factor 1/4 appears as the pulses are spaced

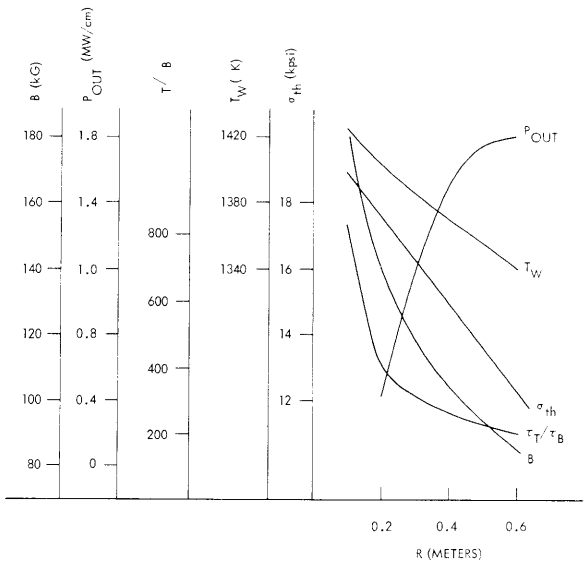

Fig. X-30. The 7-cm TZM coil.

3 pulse times apart to allow cooling. The factor 3/8 appears because the plasma burns only during a portion of the pulse. The factor 3 accounts for the electrical loss in the feed slot, as well as in the coil. For radii less than 30 cm the net power out is negative. Thus it seems that a feasible device requires lower fields and larger radii than those envisioned by Ribe.

Thermal Stress

The thermal stress attributable to the temperature gradient caused by the Bremsstrahlung at the low fields required by wall heating are well below the yield stress of 75K psi for TZM near 1400°K. The thermal stress is also included in Fig. X-30.

Cooling Requirements

The cooling for the 7-cm TZM coil is easily handled by turbulent flow of liquid lithium in channels that are 1 mm in diameter and approximately 13 cm in length. The interfacial temperature difference is 139°C, and the temperature rise along the channel is 250°C. The channels are spaced so that the heat transfer coefficient is approximately 7×10^4 Btu/hr ft^2 °F in order to guarantee turbulent flow and reasonably long channels. This spacing is less than the thermal diffusion length in the coil, yet the channel volume never exceeds 5% of the coil volume. The pressure drops needed for this cooling are approximately 20-30 psi, and the pumping power needed to pump the coolant through

the channels does not exceed 8 kW/cm, which is negligible compared with the output power which is of the order of 10^5 W/cm.

The present study indicates that the most feasible pulsed fusion devices will have TZM coils, fields of 100 kG or less, and radii of 30 cm or more.

G. L. Flint, Jr., D. J. Rose

References

1. F. L. Ribe, T. A. Oliphant, Jr., and W. E. Quinn, "Feasibility Study of a Pulsed Thermonuclear Reactor," Report LA-3294-MS, Los Alamos Scientific Laboratory, 1965.

2. END LOSS FROM A MAGNETIC MIRROR CAUSED BY FIELD FLUCTUATIONS

Consider the magnetic mirror shown in Fig. X-31, which shows a finite-β plasma in the main part where the field inside the plasma is B_1 (uniform). At the mirrors, the field is $B_o > B_1$. Suppose that B_1 increases for some reason while B_o stays constant; for example, a flute causes radial plasma loss which decreases β, but this has little effect in the region of the mirrors. Each trapped particle has its perpendicular velocity $v_\perp$ increased, hence has improved confinement with respect to the unperturbed loss cone. On the other hand, the loss cone is enlarged. Here is a question: Are particles swept into the loss cone, hence ejected from the region, or not? The question relates to observed fluctuations in high-β mirrors, for example, the device ELMO at Oak Ridge National Laboratory.

Assume that a particle spends all but a negligible fraction of its time in the uniform field region B_1. For the particle, with velocities $v_\parallel$ parallel to the axis and $v_\perp$ in the perpendicular direction, we define the particle velocity direction θ_p as

$$\tan \theta_p = v_\perp / v_\parallel . \tag{1}$$

But the loss-cone angle θ_m is

$$\sin^2 \theta_m = B_1 / B_o , \tag{2}$$

and $\theta_p \geq \theta_m$ for trapped particles. Furthermore,

$$\frac{m v_\perp^2}{2} = \mu B_1 , \tag{3}$$

where μ is the (invariant) magnetic moment. From these relations, find

$$d\theta_p / dB_1 = \sin \theta_p \cos \theta_p / 2B_1 \tag{4}$$

$$d\theta_m / dB_1 = \tan \theta_m / 2B_1 , \tag{5}$$

whence

$$d\theta_m / d\theta_p = \tan \theta_m \sec^2 \theta_p / \tan \theta_p . \tag{6}$$

Now for the most vulnerable particle at the edge of the loss cone, $\theta_m = \theta_p$. Thus if B_1 increases, $d\theta_m / d\theta_p > 1$, and some particles are <u>always</u> thrown out of the system axially.

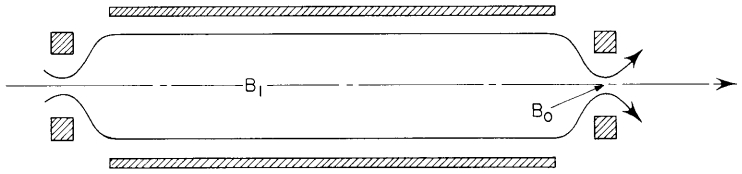

Fig. X-31. Magnetic mirror system.

Conversely, decreasing B_1 does not lead to particle loss by this mechanism.

More questions can be asked as a consequence. A first one is: Are enough particles ejected so that the total perpendicular plasma energy actually decreases (recall that the remaining particles are heated)? For a uniform filling of velocity angles out to the loss cone, the answer is easy. From Eqs. 4 and 5, the loss cone encroaches into the distribution at a rate

$$\frac{d\theta_m}{dB_1} - \frac{d\theta_p}{dB_1} = (\tan\theta_m \sin^2\theta_m)/2B_1, \tag{7}$$

and the rate of change of pressure from all causes is

$$\frac{dP_\perp}{dB_1} = \frac{P_\perp}{B_1}\left[1 - \frac{\sin^6\theta_m}{2\cos^2\theta_m\left(1 - \frac{\cos^2\theta_m}{3}\right)}\right]. \tag{8}$$

The first term in the bracket represents adiabatic heating, and the second represents the energy particles lost by the net $d\theta/dB$ mechanism of Eq. 7. From Eq. 8, the total energy decreases if

$$\frac{\sin^6\theta_m}{2\cos^2\theta_m} > 1 - \frac{\cos^2\theta_m}{3}, \tag{9}$$

which is true for $\theta_m > 60.8°$ (mirror ratio 1:31).

Finally, can $P_\perp$ decrease enough that a mirror instability will develop? Here we must have

$$\left(\frac{B_1^2}{2\mu_o} + P_\perp\right)_{after} < \left(\frac{B_1^2}{2\mu_o} + P_\perp\right)_{before}; \tag{10}$$

if so, the (presumed) equilibrium is upset by a lemon-pip (in Tennessee, watermelon-seed)

effect. Since necessarily also

$$P_{\perp} + \frac{B_1^2}{2\mu_o} < \frac{B_o^2}{2\mu_o} \tag{11}$$

or else no mirror would exist when the trap was empty, we see at once that there is no energy source to drive the instability at low β. At finite β, Eqs. 10 and 11 can be cast in the form

$$\frac{1-\beta}{\beta} + \frac{1}{2} < \frac{3x^3}{4(1-x)(2+x)} \quad \text{(unstable)} \tag{12}$$

$$x < 1 - \beta, \tag{13}$$

where

$$x = \sin^2 \theta_m. \tag{14}$$

Equations 12 and 13 can be combined in the inequality

$$(x+1)(x+2) < 3x^3/2 \quad \text{(unstable)}, \tag{15}$$

which cannot be satisfied for $x < 1$. Thus a mirror instability cannot develop from this effect.

D. J. Rose

3. EFFECT OF HIGH FUEL BURN-UP IN PROPOSED DEUTERIUM-TRITIUM FUSION REACTORS

A computer study of conditions expected inside a deuterium-tritium (D-T) fusion reactor for conditions of low fractional fuel burn-up[1] (f_b) is being extended to regions of high burn-up. Results have been obtained for comparison with a fusion feasibility study in which a different assumption about helium nuclei (α-particle) energy deposition[2] was used.

In summary, the model uses the following proposed energy balance. D + T ions are

Table X-1. Plasma parameters for large f_b exponential lifetime distribution assumption.

	V_i (keV)	T_i (keV)	f_b	Ψ	Q
$C_1 = 1.$	100	64.7	.0416	.202	3.66
$C_2 = 0.2$	100	74.0	.0656	.155	5.78
$D = 1.$	100	84.5	.0952	.125	8.37
$V_e = 0$	100	93.0	.1256	.103	11.05
$J = 1.$	100	99.1	.1544	.0855	13.60
	80	60.4	.0564	.132	6.20
	80	66.1	.0702	.121	7.72
	80	77.6	.1005	.105	11.05
	80	93.1	.1546	.0812	17.00
	60	52.7	.0609	.0961	8.95
	60	58.8	.0751	.0930	11.03
	60	70.8	.1055	.0861	15.50
	60	87.3	.1579	.0737	23.2
	40	45.6	.0661	.0673	14.55
	40	52.0	.0805	.0695	17.70
	40	64.2	.1100	.0701	24.2
	40	81.2	.1605	.0655	35.3
	20	39.5	.0721	.0462	31.7
	20	45.9	.0863	.0509	38.0
	20	58.4	.1163	.0567	51.2
	20	75.5	.1651	.0565	72.6
	0	34.3	.0786	.0317	–
	0	40.7	.0933	.0368	–
	0	53.0	.1227	.0449	–
	0	70.0	.1699	.0488	–

injected with energy V_i, for which input power is required. Inside the plasma, the ions have energies in a presumed Maxwellian distribution at temperature T_i. They are confined with a mean lifetime τ_i and carry off power as they leave. Similar things can happen to electrons, for which the symbols V_e, T_e, and τ_e apply. Also, electrons can lose energy via Bremsstrahlung, multiplied by an adjustable dimensionless constant C_1, and modified synchrotron radiation, multiplied by a similar constant C_2 to account for reflectivity of the surrounding vacuum walls. Electrons and ions interchange energy by Coulomb interactions. Inside the plasma, D + T ions fuse and two-tenths of the fusion power appears with the energetic α particles formed in the nuclear reaction. The α density is small, but the α energy is high and hence the α pressure is substantial. The α cool in the plasma by dynamical friction on both electrons and ions; their energy distribution is not Maxwellian. By assumption, for this study, the lifetimes of the alpha particles are exponentially distributed, with a time constant set equal to the ion lifetime.

Table X-1 shows some plasma conditions calculated for typical open-ended systems. In every case, electrons are injected with zero energy ($V_e=0$), the ion and electron confinement times are the same, ($J=\tau_i/\tau_e=1$), and an intermediate assumption is made about the escape of synchrotron radiation from the optically thick plasma ($C_2=0.2$, $D=1$, according to a previous report[2]). From the computer calculations, we find two quantities of interest for reactor feasibility, ψ and Q. ψ is the probability of ion loss per 90° effective Coulomb scatter, and Q is the ratio of fusion power to injection power.

The results shown in Table X-1 are plotted in Fig. X-32, as contours of constant

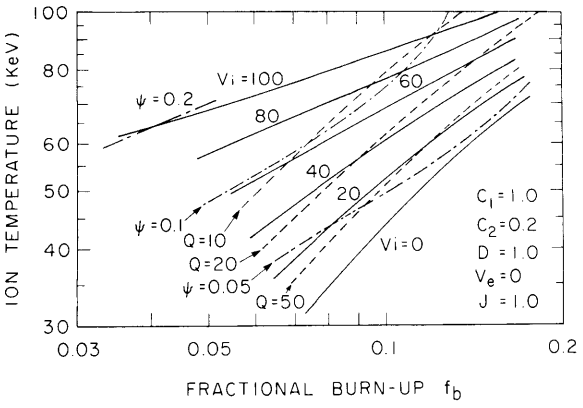

Fig. X-32. Contours of constant V_i, ψ, Q on an f_b-T_i scale.

V_i, ψ, and Q on an f_b-T_i scale. This graph shows that it will be more difficult to operate in a region of high Q. For very optimistic confinement, $\psi = 0.1$, the best Q would be a bit more than 10, for an f_b around 0.10. These results are more pessimistic than those in the feasibility study,[2] as can be seen by comparing contours of Q in

Fig. X-33. The contours of Q are those from Fig. X-32, containing the assumption of exponential distribution of α lifetimes. The contours of Q^* are for the same input values, except for the assumption that the α completely thermalize, which were calculated in the previous feasibility study. For a given f_b, Q is lower than Q^*. Even though confinement time is long at high burn-up, and the α deposit much of their energy, not all is deposited, some α escape early, and Q is deleteriously affected.

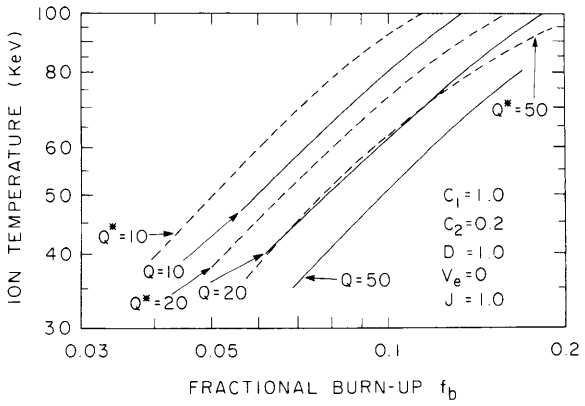

Fig. X-33.
Values of Q for exponential lifetime distribution assumption compared with Q^* for complete α-particle thermalization.

These two assumptions, fixed lifetime τ_α for each α particle, or an exponential distribution with mean life τ_α, in our view enclose what would be the true situation in a fusion plasma. This begs the question of whether other effects not included in this plasma model (such as non-Maxwellian electron velocity distribution) will alter the energy balance still further.

F. B. Marcus, D. J. Rose

References

1. F. B. Marcus and D. J. Rose, "Effect of Low Fuel Burn-up in Proposed Deuterium-Tritium Fusion Reactors," Quarterly Progress Report No. 93, Research Laboratory of Electronics, M.I.T., April 15, 1969, pp. 122-130.

2. D. J. Rose, "On the Feasibility of Power by Nuclear Fusion," ORNL-TM-2204, Oak Ridge National Laboratory, May 1968.

4. SYNCHROTRON RADIATION FROM A FUSION PLASMA ENCLOSED BY REFLECTING WALLS

We want to determine the synchrotron radiation intensity from a plasma enclosed by reflecting metal walls for proposed operating ranges of fusion reactors. First, the reflectivity of the surrounding walls is found. The electrical resistivity of possible metals for the wall is obtained from formulas and tables. The reflectivity at a given frequency is calculated for resistivities at different temperatures. With these we can find an effective reflectivity Γ for an open-ended system. Γ is lowered primarily because of physical holes through which radiation can escape; variations in metal reflectivity caused by temperature and radiation wavelength will have little effect on the results.

In order to calculate the radiation from a plasma with a previously developed model, it is necessary to derive a synchrotron radiation coefficient C_2, in the symbolism used previously,[1] which is the ratio of actual power radiated to the amount of energy that would be radiated if there were no reflectors present in the system. Since the area under a curve of spectral intensity vs frequency represents total radiated power, the ratio of the areas of power curves with reflectors to power curves without reflectors gives C_2. It is a very complex computational task to calculate the power radiated as a function of frequency at a given electron temperature T_e. Partial results have been obtained for T_e = 25 keV and T_e = 50 keV. The value of C_2 will be calculated for these two cases, and we shall show that it is approximately the same for both. We can therefore assume that C_2 is roughly a constant and use it for intermediate values of T_e. A calculation is performed on the plasma model to find actual radiation level.

Expressions[2,3] for electrical resistivity (η) for Mo and Nb at different wall temperatures are used to calculate Table X-2. The surface reflectivity Γ^*, which is the fraction

Table X-2. Resistivity and reflectivity coefficients.

Material	Temperature (°K)	Electrical Resistivity η (Ω-cm)	Reflectivity Γ
Mo	800	18.6×10^{-6}	.9848
Mo	1100	26.7×10^{-6}	.9818
Mo	1400	35.1×10^{-6}	.9791
Nb	800	36.7×10^{-6}	.9786
Nb	1100	47.0×10^{-6}	.9759
Nb	1400	54.6×10^{-6}	.9740

of incident power reflected from a metal wall, is given in MKS units by[4]

$$\Gamma^* = 1 - 4\sqrt{\frac{\omega\epsilon_o\eta}{2}}, \quad \omega\epsilon_o\eta \ll 1. \tag{1}$$

For Table X-2, let ω be the twentieth harmonic of electron synchrotron frequency ω_b for a magnetic field B_o of 5 T (experience shows that the power spectrum peaks at $\omega \approx 20\ \omega_b$). Note that a representative value is $\Gamma = 0.98$, and that variations will be small over different temperatures and frequencies. Next, an effective Γ may be found for an open-ended system. Assume a configuration of a closed cylindrical surface with a hole cut out at each end. Typically, the end holes with zero reflectivity take up 8% of the surface area; the rest would have $\Gamma^* = 0.98$. We thereby obtain an effective $\Gamma = 0.9$ to be used in radiation calculations.

The basic synchrotron radiation equation is[5]

$$S \propto S_B[1 - \exp(-aL)], \tag{2}$$

where S is the intensity of radiation at frequency ω, S_B is the spectral intensity of black-body radiation at temperature T_e and frequency ω. The quantity a is the energy absorption coefficient for a ray propagating in the plasma, and L is a characteristic length of the plasma. At the frequencies of interest, the Rayleigh-Jeans approximation for S_B is valid. Thus for fixed T_e, for dimensionless frequency ω/ω_b, we obtain

$$S \propto \left(\frac{\omega}{\omega_b}\right)^2 [1 - \exp(-aL)], \tag{3}$$

where ω_b is the nonrelativistic synchrotron frequency at B_o. If the plasma is enclosed by reflectors with an effective reflectivity Γ, then the intensity of radiation S_Γ is given by

$$S_\Gamma \propto \frac{S_B[1 - \exp(-aL)][1-\Gamma]}{1 - \Gamma \exp(-aL)}. \tag{4}$$

Let S_{50}, $(aL)_{50}$, and $S_{\Gamma 50}$ denote S, (aL), and S_Γ at $T_e = 50$ keV, $\Gamma = 0.9$, and similarly for S_{25}, $(aL)_{25}$, and $S_{\Gamma 25}$ at $T_e = 25$ keV, $\Gamma = 0.9$. Values for S_{50} and $S_{\Gamma 50}$ are in relative units, and values for $(aL)_{50}$ vs ω/ω_b are available[6] and are shown in Table X-3 and in Figs. X-34 and X-35. These values are for $\mathscr{L} = 10^4$, where

$$\mathscr{L} = \frac{\omega_p^2 L}{\omega_b C}, \tag{5}$$

with plasma frequency ω_p. This value of $\mathscr{L}$ will be justified here. Trapezoidal

Table X-3. Plasma synchrotron radiation with and without reflectors.

$\frac{\omega}{\omega_b}$	$(\alpha L)_{50}$	S_{50}	$S_{\Gamma 50}$	X	$(\alpha L)_{25}$	S_{25}	$S_{\Gamma 25}$
1	Large	1.5	0.	1.0	Large	1.5	0.2
2	Large	4.0	0.5	1.0	Large	4.0	0.4
3	Large	7.0	0.8	1.0	Large	7.0	0.7
4	Large	13.0	1.0	1.0	Large	13.0	1.3
5	Large	19.0	1.5	0.725	1.3	13.8	1.8
6	14.7	30.0	2.5	0.710	1.2	21.3	2.9
7	5.6	39.0	3.5	0.513	0.71	20.0	3.6
8	2.88	49.0	5.0	0.297	0.33	14.4	4.1
9	1.37	50.0	6.5	0.157	0.12	7.8	3.9
10	0.750	41.5	8.0	0.118	0.064	4.9	3.3
11	0.463	34.0	8.7	0.080	0.052	2.7	1.9
12	0.288	28.5	9.0	0.067	0.017	1.9	1.7
13	0.177	22.0	9.0	0.067	0.001	1.5	1.4
14	Small	18.0	9.0	0.059	Small	1.1	1.1
15	Small	15.0	8.5	0.058	Small	0.9	0.9
16	Small	11.5	8.0	0.	Small	0.	0.
17	Small	8.0	6.0	0.	Small	0.	0.
18	Small	5.0	5.0	0.	Small	0.	0.
19	Small	3.0	3.0	0.	Small	0.	0.
20	Small	2.0	2.0	0.	Small	0.	0.

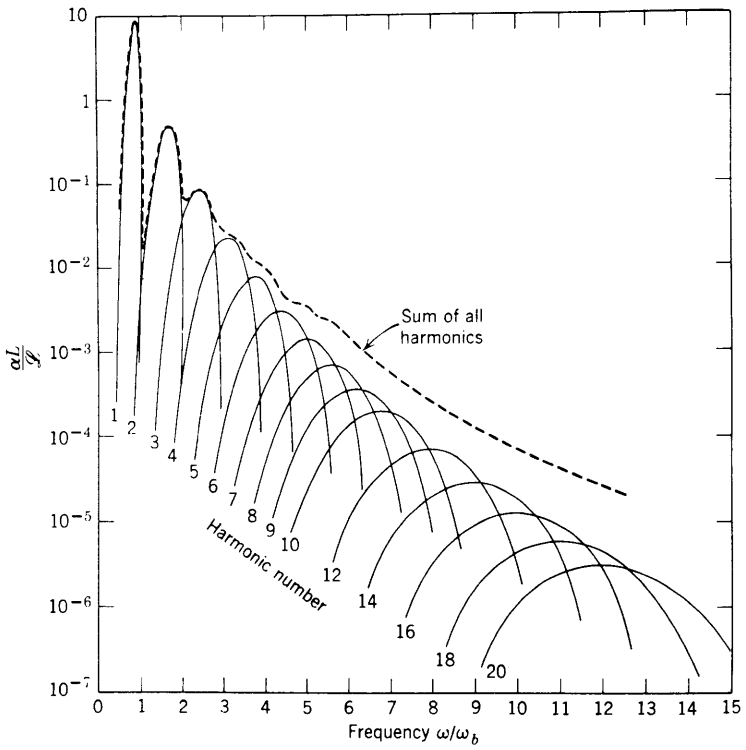

Fig. X-34. Dimensionless absorption coefficient $aL/\mathscr{L}$ for cyclotron radiation as a function of dimensionless frequency ω/ω_b, for a plasma with electron temperature $T_e = 50$ keV. (After J. L. Hirshfield, D. E. Baldwin, and S. C. Brown.)

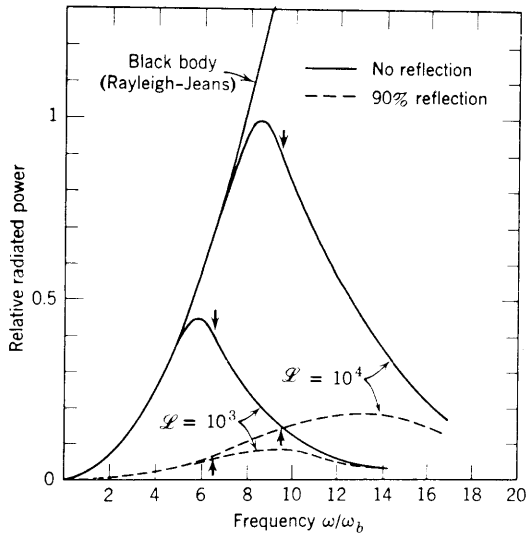

Fig. X-35.

Relative cyclotron radiation loss from a plasma at $T_e = 50$ keV for $\mathscr{L} = \omega_p^2 L/\omega_b C = 10^3$ and 10^4 with and without 90% reflecting walls. Short arrows indicate the frequency ω^* at which $aL = 1$.

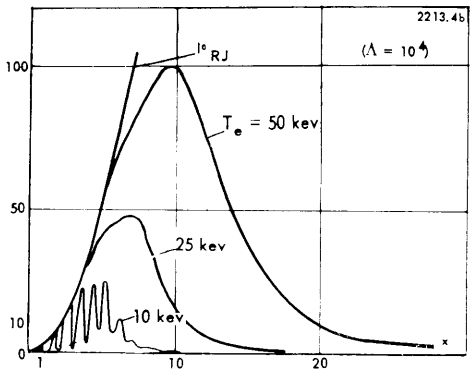

Fig. X-36.

Relative cyclotron radiation loss from a plasma slab at $T_e = 50$ keV, 25 keV, 10 keV for $\Lambda = \omega_p^2 L/\omega_b C = 10^4$. In this case Λ is $\mathscr{L}$. (After B. A. Trubnikov and V. S. Kudryavtsev.[7])

integrations of S_{50} and $S_{\Gamma 50}$ yield

$$C_2(T_e = 50 \text{ keV}) = \frac{96.5}{399.3} = 0.24. \tag{6}$$

Now let us find $C_2(T_e = 25 \text{ keV})$. Define the ratio $X = S_{25}/S_{50}$. Values for S_{25} and X are available[7] and are shown in Table X-3 and in Fig. X-36. From Eq. 3,

$$(aL)_{25} = \ln\left[\frac{1}{1 - X\{1 - \exp[-(aL)_{50}]\}}\right]. \tag{7}$$

Values for $(aL)_{25}$ in Table X-3 are found from Eq. 7. From Eqs. 2 and 4,

$$S_{\Gamma 25} = \frac{S_{25}[1-\Gamma]}{1 - \Gamma \exp[-(aL)_{25}]}. \tag{8}$$

Values for $S_{\Gamma 25}$ in Table X-3 are found from Eq. 8. Trapezoidal integrations of S_{25} and $S_{\Gamma 25}$ yield

$$C_2(T_e = 25 \text{ keV}) = \frac{29.1}{115.1} = 0.25. \tag{9}$$

For $\mathscr{L} = 10^4$ and $\Gamma = 0.9$, C_2 has nearly the same value at $T_e = 25$ keV and $T_e = 50$ keV. Therefore, it seems reasonable to adopt $C_2 = 0.25$ for intermediate values of T_e. Table X-3 may be used for calculations for other Γ.

With a previously developed model of a fusion plasma,[1] we find a completely self-consistent solution, with $C_2 = 0.25$. Relevant quantities are the magnetic field at the vacuum wall (B_m), the magnetic field at the plasma surface (B_o), the radius of wall facing the plasma in a cylindrical geometry (r_w), the neutron power deposition per unit wall area (S_o), a dimensional parameter characteristic of the system (D), the ion temperature (T_i), ion and electron injection voltages (V_i and V_e), fractional fuel burn-up (f_b), total synchrotron radiation per fusion event (U_c), with each fusion event giving 3500 keV to the plasma. Results have been calculated[8] for $T_e = 40$ keV and are shown in Table X-4 for comparison with results from the previous feasibility study.[1] Other symbols are described there.

The thing to note here is the ratio C_2/D, which is a multiplicative factor in the synchrotron radiation term of the model. This ratio is considerably larger in the self-consistent case. The radiation is much greater than was hitherto estimated, as is shown by the term U_c; f_b is much higher, which will also justify a model assumption of complete alpha-particle fusion energy deposition in the plasma. This raises T_i and makes energy available for the increased radiation. Note that the answer is

Table X-4. Comparison of previous results with self-consistent results for an open-ended system.

		Feasibility Study	Self-consistent
T_e = 40 keV	Input C_2	.08	.25
C_1 = 1.	Input D	1.	.74
J = 1.	Assumed $\mathscr{L}$	10^4	10^4
V_i = 40 keV	Computer calculated T_i	62.8 keV	79.3 keV
V_e = 0 keV	β	.284	.33
B_o = 5 T	r	$1.23\times10^{20}/m^3$	$1.31\times10^{20}/m^3$
B_m = 10 T	$\mathscr{L}$	1.24×10^4	1.24×10^4
Γ_w = 3 m	D	.59	.74
$S_o = 10^7$ W/m^2	$U_{\alpha i}$	1954 keV	1954 keV
	$U_{\alpha e}$	1542 keV	1542 keV
	f_b	.072	.134
	U_x	80.3 keV	79.0 keV
	U_c	259 keV	1345 keV

self-consistent, with calculated D = 0.74, and $\mathscr{L}$ is close to 10^4. Thus we have shown that C_2 may be considered a constant over a range of T_e, and that the synchrotron radiation is considerably larger than had been assumed in previous calculations.

Solutions to the plasma energy-balance equations that are internally self-consistent to this extent are hard to come by, and we have calculated just one. There are many others, and our judgment is that more attractive solutions lie at lower fractional burn-up (0.08?) than was found here (0.134). Such solutions would naturally have lower T_e, hence lower synchrotron radiation loss. Thus the discontentful situation here will be somewhat ameliorated; but it seems that the synchrotron radiation losses in mirrors is likely to exceed those casually implied heretofore.[1]

F. B. Marcus, D. J. Rose

References

1. D. J. Rose, "On the Feasibility of Power by Nuclear Fusion," ORNL-TM-2204, Oak Ridge National Laboratory Report, May 1968.
2. For Mo, see International Critical Tables.

3. For Nb, unpublished information from David J. Rose.

4. R. B. Adler, L. J. Chu, and R. M. Fano, Electromagnetic Energy Transmission and Radiation (John Wiley and Sons, Inc., New York, 1960), p. 431.

5. D. J. Rose and M. Clark, Jr., Plasmas and Controlled Fusion (The M.I.T. Press, Cambridge, Mass., 1961), Chap. 11.

6. Ibid., pp. 248, 249.

7. B. A. Trubnikov and V. S. Kudryavtsev, "Plasma Radiation in a Magnetic Field," in Proc. Second International Conference on Peaceful Uses of Atomic Energy, Geneva, 1958, Vol. 31, p. 93.

8. F. B. Marcus, "Effects of Fuel Burnup and Synchrotron Radiation in Fusion Reactors," S.B. Thesis, M.I.T., 1969.

5. STABILITY OF A RELATIVISTIC ELECTRON LAYER

We have continued our study of the stability of a relativistic gyrating electron beam as previously formulated.[1, 2] In the last report,[2] we presented a dispersion relation for the beam in vacuum. Now, we shall examine this dispersion relation in some detail, and in the last part of this report we shall consider the case in which background plasma is included. Nyquist stability methods have been used to study these dispersion relations.

Stability of the Beam in Vacuum

The dispersion relation for a neutralized relativistic electron beam in vacuum, located at radius R with thickness τ, can be written[2]

$$D_1(\bar{\eta}, \ell) + \frac{1}{\ell}(b_+ + b_-) = 0, \tag{1}$$

where

$$D_1(\bar{\eta}, \ell) = K\left(\frac{1}{\bar{\eta} - \delta\eta} - \frac{1}{\bar{\eta} + \delta\eta}\right) + K^2 \log \frac{\bar{\eta} + \delta\eta}{\bar{\eta} - \delta\eta} + K^2\left(\frac{\bar{\eta} - \delta\eta}{\bar{\eta} + \delta\eta} - \frac{\bar{\eta} + \delta\eta}{\bar{\eta} - \delta\eta}\right). \tag{2}$$

In these equations,

$$\bar{\eta} = \frac{\omega - \ell\omega_o(R)}{\omega_o(R)}, \qquad \delta\eta = \frac{1}{2}\frac{\ell\tau}{R} \tag{3}$$

$$K = \omega_p^2/\omega\omega_o \approx \omega_p^2/\ell\omega_o^2 \tag{4}$$

$$b_+ = \frac{\ell}{j\omega\epsilon_o}\left(\frac{H_z}{E_\theta}\right)_{r=r_2^+} \tag{5}$$

$$b_- = -\frac{\ell}{j\omega\epsilon_o}\left(\frac{H_z}{E_\theta}\right)_{r=r_1^-} \tag{6}$$

and the remaining symbols are the same as those used previously.[1, 2]

The map of the lower half of the cut $\bar{\eta}$ plane on the D_1 plane is illustrated in Fig. X-37. The Nyquist criteria indicate that the beam is stable if the contour Γ_1, in the D_1-plane (Fig. X-37) does not enclose the point $-\frac{1}{\ell}(b_+ + b_-)$. Therefore, for all lossless, "inductive" structures,[3] $b_+ + b_- < 0$, the beam is stable; while for lossy and some capacitive structures, $b_+ + b_- > 0$, instability is predicted.

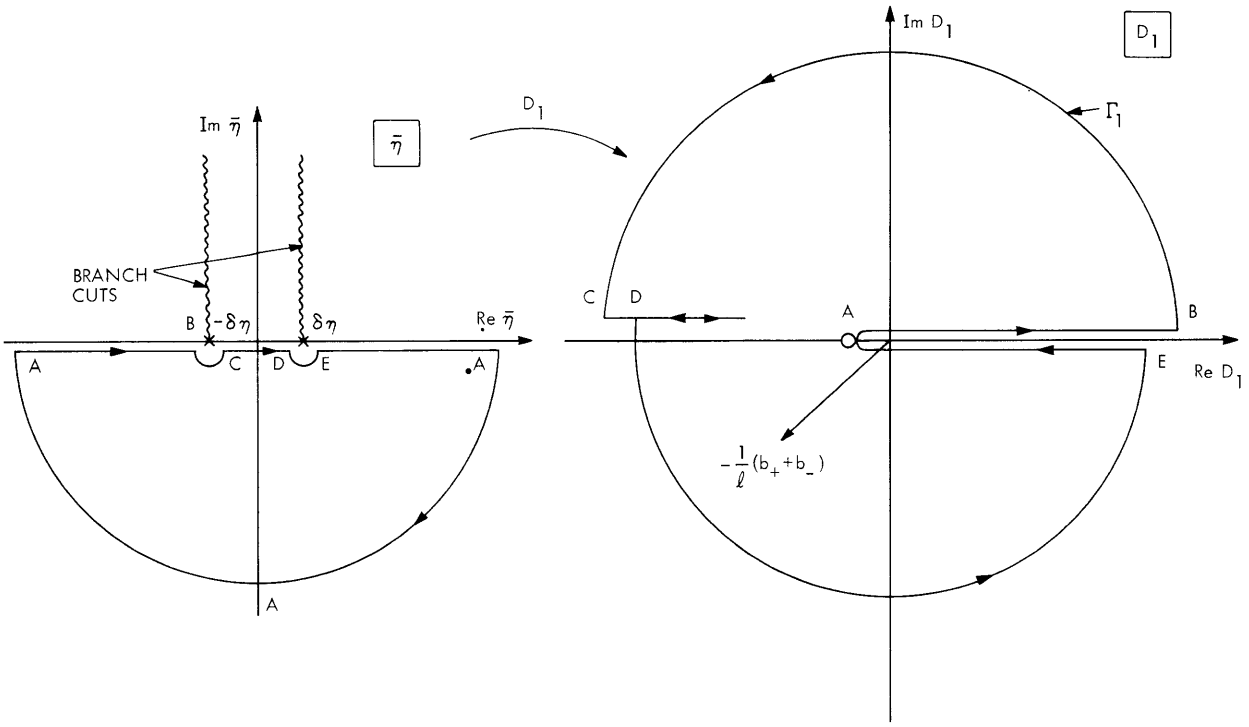

Fig. X-37. Map of the lower half of $\bar{\eta}$ plane on D_1 plane.

It is of some interest to compute the growth rates for capacitive structures, under the assumption that the beam is "tenuous." For such cases, K is small, and thus as a first approximation, Eq. 1 becomes

$$\frac{1}{\ell}(b_+ + b_-) + K\left(\frac{1}{\bar{\eta} - \delta\eta} - \frac{1}{\bar{\eta} + \delta\eta}\right) = 0. \tag{7}$$

The omitted terms involve factors of K^2 and are of higher order in $\bar{\eta}$, the expansion parameter. Equation 7, when solved for η, yields

$$\bar{\eta} = -\left[\frac{K}{b_+ + b_-} \pm \sqrt{\frac{K^2}{(b_+ + b_-)^2} + 1 - \frac{K\,4R}{\tau(b_+ + b_-)}}\right]. \tag{8}$$

Note that the first term under the radical is assumed small. Thus, stability results if

$$1 > \frac{K\,4R}{\tau(b_+ + b_-)}$$

or

$$\ell > 4\zeta\left(\frac{R}{\tau}\right)^2 \frac{1}{(b_+ + b_-)}, \tag{9}$$

where $\zeta = \dfrac{\omega_p^2 \tau}{\omega_o^2 R}$ is known as the "loading factor" and is essentially equal to the ratio of the self-magnetic field to the applied magnetic field. Equation 9 indicates that, even if the structure is capacitive, the beam is stable when the wave number ℓ is large enough. As ℓ increases, the assumption that K is small becomes better ($K \sim 1/\ell$), and the growth rate, because of the omitted terms, becomes diminishingly small. As an example, consider an electron beam parametrized by $\omega_p^2/\omega_o^2 = 0.2$ and $R/\tau = 20$, located in vacuum inside a (capacitive) structure with dimensions $a/R = 2/3$ and $b/R = 1.4$.[3] For this configuration, Eq. 9 predicts stability for $\ell \geq 7$. We have also shown that when $\ell \geq 7$ the growth rate attributable to the omitted terms ($\sim K^2$) in Eq. 2 is very small.

As a closing remark, we note that the present analysis is consistent with that of Briggs and Neil[3] as we let $\tau \to 0$. In so doing, only the last term under the radical in Eq. 8 is important. Furthermore, the series expansion should not be pushed any farther because we have omitted terms of higher order in η when we formulated the constitutive relation for J_θ.

Stability of the Beam in a Cold Plasma

We shall now consider the effects of a cold plasma on a relativistic E-layer of intermediate thickness. The inclusion of background plasma will modify the previous formulation in the following way: An additional contribution to the total current arising from a background plasma is now introduced into the constitutive relation. Needless to say, the values of the wave admittances $b_\pm$ at the beam edges are also modified because of the presence of plasmas; otherwise, the analysis is identical with the one we have described in some detail previously.

The model consists of a metallic cylinder of inner radius a and outer radius b, between which the E-layer, located between r_1 and r_2, is immersed in a blanket of cold (collisionless) plasma. We are still concerned with the negative-mass mode whose only nonvanishing field quantities are H_z, E_r, and E_θ, and whose frequencies are near $\ell\omega_o$. The total perturbation current now is

$$\vec{J} = \vec{J}(\text{beam}) + \vec{J}(\text{plasma})$$

$$= \hat{r}\left[\frac{\epsilon_o \omega_{p2}^2 E_\theta}{\omega_o} + \frac{\omega_{p1}^2 \epsilon_o}{\omega^2 - \omega_c^2}(\omega_c E_\theta - j\omega E_r)\right]$$

$$+ \hat{\theta}\left[\frac{j\omega_o}{(\omega - \ell\omega_o)} \frac{d}{dr}\left(\frac{\epsilon_o \omega_{p2}^2 r E_\theta}{\omega_o}\right) + \frac{\omega_{p1}^2 \epsilon_o}{\omega^2 - \omega_c^2}(-\omega_c E_r - j\omega E_\theta)\right].$$

Here,

ω_{p2}^2 = plasma frequency of the E-layer

ω_{p1}^2 = plasma frequency of the background plasma

$\omega_c = -\frac{eB_o}{m_o}$ $(=\gamma_o\omega_o)$.

With this expression substituted in Maxwell's equations, and after eliminating E_r and H_z, we arrive at the following differential equation:

$$\frac{d}{dr}\left[\frac{\ell(K_1+K_2)\, rE_\theta}{\ell^2 - \frac{\omega^2}{c^2}K_\perp r^2}\right] - K_\perp \frac{d}{dr}\left[\frac{r\frac{d}{dr}(rE_\theta)}{\ell^2 - \frac{\omega^2}{c^2}K_\perp r^2}\right]$$

$$- K_1\left[\frac{\ell\frac{d}{dr}(rE_\theta) - \frac{\omega^2}{c^2}r(K_1+K_2)\, rE_\theta}{\ell^2 - \frac{\omega^2}{c^2}K_\perp r^2}\right]$$

$$+ \frac{\omega_o K_2}{\omega - \ell\omega_o}\frac{d}{dr}(rE_\theta) + K_\perp E_\theta = 0, \qquad (10)$$

where

$$K_\perp = 1 - \frac{\omega_{p1}^2}{\omega^2 - \omega_c^2}$$

$$K_1 = \frac{\omega_{p1}^2\omega_c}{\omega\left(\omega^2-\omega_c^2\right)}$$

and $K_2 = \omega_{p2}^2/\omega\omega_o$.

The remaining task is to solve Eq. 10 subject to appropriate boundary conditions at r_1 and r_2. Note that Eq. 10 has a simple mathematical structure (though the algebra is complicated when we series-expand its solution), in the sense that it has only one singularity, namely at a point where $\omega - \ell\omega_o = 0$, in the region of interest since the

point $r' = \ell c/\omega\sqrt{K_\perp}$ does not lie between r_1 and r_2 for the parameters of interest here $\left(K_\perp \gtrsim 1.4 \text{ for } \omega_{pl}^2/\omega_o^2 \gtrsim 30\right)$. Therefore, the series solution expanded about the singularity converges rapidly enough at the beam edge, in contrast to the vacuum case.

We have obtained a series solution for $\phi = rE_\theta$ about the singularity $\Omega = \omega - \ell\omega_o = 0$. For convenience, we set $\omega_o = c/r$ and ω_{pl}^2 a constant across the beam. With the series solution substituted in the boundary conditions at r_1 and r_2, we obtain the following dispersion relation.

$$D(\Omega) \equiv (\Omega-\delta\Omega)^{|\rho|}\left[a_1 + \frac{b_1(\Omega+\delta\Omega)}{(\Omega-\delta\Omega)} + \frac{c_1}{(\Omega-\delta\Omega)}\right]$$

$$- (\Omega+\delta\Omega)^{|\rho|}\left[a_2 + \frac{b_2(\Omega-\delta\Omega)}{(\Omega+\delta\Omega)} + \frac{c_2}{(\Omega+\delta\Omega)}\right]$$

$$= 0, \tag{11}$$

where

$$a_{1,2} = -\frac{K_2}{\rho\ell}\left[\frac{\gamma_o}{\ell} \pm b_\mp + \frac{\ell K_2^2}{K_\perp \rho}\right]$$

$$b_{1,2} = \frac{r_{2,1}K_2}{r_{1,2}\ell}\left[\frac{\gamma_o}{\ell} \mp b_\pm + K_2\left(\frac{1}{2+\rho} + \frac{\ell K_2}{\rho}\right)\right]$$

$$\rho = \frac{\ell K_2}{K_\perp}(1-K_\perp), \qquad c_{1,2} = \frac{c}{r_{1,2}}\left(-\frac{K_2^2}{\rho}\right)$$

$$\delta\Omega = \frac{1}{2}\frac{\ell c\tau}{r_1 r_2}$$

$$\Omega = \omega - \ell\omega_o(R).$$

In the analysis up to this point we have imposed no restriction on the plasma density distribution outside the beam. We have considered a simplified case in which the plasma blanket extends uniformly from the inner to outer walls. Furthermore, if the plasma density is high enough ($\gtrsim 10^{10}/\text{cm}^3$ for modes $\ell < \gamma_o \approx 9$), the fields outside the beam decay rapidly, and the edge impedance is approximately that of an infinite plasma. This assumption simplifies the calculation of $b_\pm$ considerably. Under this assumption, we obtained the Nyquist plot of D for various particular values of τ/R, ζ, ℓ and ω_{pl}^2. The result is as follows. For a given value of τ/R, ζ and ℓ, there is a critical plasma density (which increases with ℓ at fixed ζ and τ/R) above which the Nyquist contour of D

does not encircle the origin (see Fig. X-38). In other words, the negative mass instability can be suppressed by a high-density plasma background. A numerical example with $\tau/R = 1/20$, $\zeta = 4\%$ is illustrated in Fig. X-38.

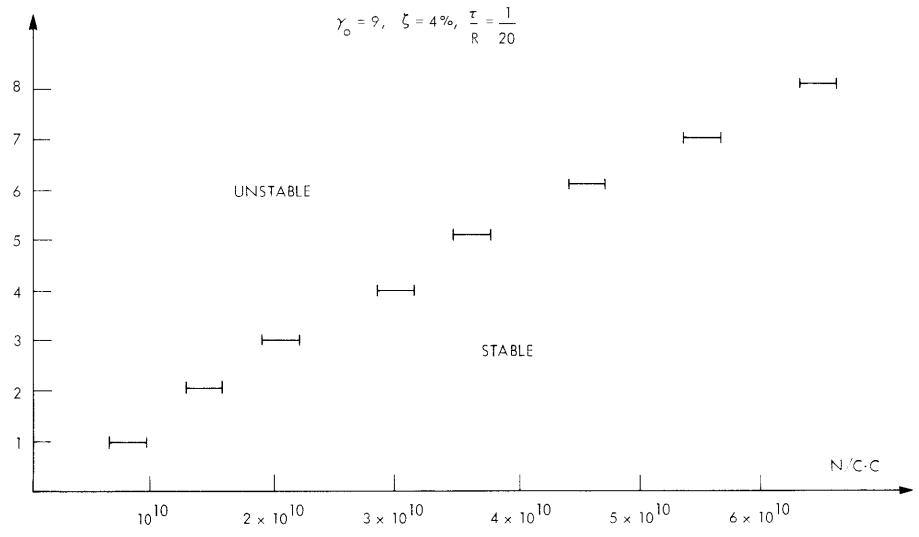

Fig. X-38. Critical plasma density as a function of ℓ.

Analytically, we can show that the following set of inequalities yields sufficient conditions for stability according to the general dispersion relation,[11]

$$\left.\begin{aligned} a_1 + b_1 - a_2 - b_2 &< 0 \\ c_2 - 2b_2\delta\Omega &> 0 \\ c_1 + 2b_1\delta\Omega &> 0 \\ a_1 - \frac{c_1}{2\delta\Omega} &< 0 \end{aligned}\right\} \qquad (12)$$

and the numerical data agreed with this result. It is of some interest to note, according to our data, that in the stable regime, $b_+ + b_- < 0$, and in the unstable regime, $b_+ + b_- > 0$, so that the stabilization at higher plasma densities is basically an inductive medium effect. Also, the curve in Fig. X-38 has a remarkable resemblance to the result of Briggs,[4] which was obtained from a model with zero thickness.

Y. Y. Lau, R. J. Briggs

References

1. Y. Y. Lau and R. J. Briggs, Quarterly Progress Report No. 92, Research Laboratory of Electronics, M. I. T., January 15, 1969, pp. 266-271.

2. Y. Y. Lau and R. J. Briggs, Quarterly Progress Report No. 93, Research Laboratory of Electronics, M. I. T., April 15, 1969, pp. 126-130.

3. R. J. Briggs and V. K. Neil, "Negative-Mass Instability in a Cylindrical Layer of Relativistic Electrons," J. Nucl. Energy, Part C, Vol. 9, pp. 207-227, 1967.

4. R. J. Briggs, "Effects of Cold Plasma on the Negative-Mass Instability," UCID-15001, University of California, Lawrence Radiation Laboratory, Livermore, California, July 15, 1966.